Investigation of grain size and shape effects on crystal plasticity by dislocation dynamics simulations

Maoyuan Jiang

université PARIS-SACLAY

NNT : 2019SACLC035

Thèse de doctorat

Exploration des effets de la taille et de la forme des grains sur la plasticité cristalline par simulations de dynamique des dislocations

Investigation of grain size and shape effects on crystal plasticity by dislocation dynamics simulations

Thèse de doctorat de l'Université Paris-Saclay
préparée à CentraleSupélec

École doctorale n°579 : Sciences Mécaniques et Energétiques, Matériaux et Géosciences (SMEMaG)
Spécialité de doctorat : Mécanique des solides

Thèse présentée et soutenue à Gif-sur-Yvette, le 04 Juin 2019, par

MAOYUAN JIANG

Composition du Jury :

M. Renald BRENNER DR CNRS, Sorbonne Université (Institut Jean le Rond d'Alembert)	Président
M. Xavier FEAUGAS Professeur, Université de La Rochelle (LaSIE)	Rapporteur
M. Marc VERDIER DR CNRS, Grenoble INP (SIMaP)	Rapporteur
Mme. Véronique AUBIN Professeur, CentraleSupélec (MSSMat)	Examinatrice
M. Claude FRESSENGEAS Professeur émérite, Université de Lorraine (LEM3)	Invité
M. Ghiath MONNET Chercheur-Ingénieur, EDF R&D (MMC)	Co-directeur de thèse
M. Benoit DEVINCRE DR CNRS, CNRS-ONERA (LEM)	Directeur de thèse

Acknowledgements

Ten years ago, when I finished high school and came to France to pursue my studies, I never thought I would complete a PhD. Today, when I look back, I still feel determined and thrilled to choose this path. I am grateful to all the people who have accompanied and supported me throughout this extraordinary intellectual adventure in the world of science.

First of all, I would like to express my gratitude to the reviewers of my thesis, Xavier Feaugas and Marc Verdier, and to the examinaters, Véronique Aubin, Renald Brenner and Claude Fressengeas. Thank you for agreeing to be members of the thesis committee and the exchanges during the thesis defense are extremely enlightening.

I am sincerely grateful to my tutors, Benoit Devincre and Ghiath Monnet. I think you two make the best tutoring team to guide my research work by contributing independently but complementarily. Thanks to Benoit for taking me into the field of Dislocation Dynamics. I remembered it well the first time he showed me the videos of DD simulations at the internship speed dating in Cachan, how fascinated I was. Since then, the seed of curiosity has been planted in my mind and keeps motivating me. With great patience and generosity, Benoit can always pass on his knowledge in the simplest and most inspiring way. I also admire his rigor and open-mindedness in conducting research. Ghiath is by appearance a very strict person, but in fact a warm person by heart. I appreciate every discussion with him because he can always make concise and insightful remarks. In particular, the trust and encouragement from Ghiath gave me a lot of strength during these three years.

Many thanks to Alphonse Finel and Yann Le Bouar for allowing me to finish my thesis in LEM laboratory. The welcoming and pleasant atmosphere of the laboratory is unforgettable. LEM is small but great, because all my colleagues are wonderful. Riccardo Gatti, he helped me a lot when I started using the code. In addition, I am grateful for the time he took to attend my thesis meetings and he made many suggestions to refine my work. I would like to thank Ladislas Kubin and Georges Saada for their helpful comments on my work, and I also enjoyed the stories they have told me about their extraordinary life experiences. I insist on expressing my gratitude to Jean-Sébastien Merot, I think he is the best computer support engineer we can have in the laboratory and I feel lucky. With his help, my routine computer-related work became much easier. I also want to thank Viviane Cothias, Fadoua Hammami, Catherine Deutsch, their help is essential to solve all the administrative problems that appeared at the end of my thesis.

In the laboratory, not only do we have the most serious discussions on scientific topics, but we also have a lot of fun. Benoît Appolaire and Mathieu Fèvre form such a great team to make jokes. The football prognosis match organized by Frédéric Fossard becomes a special festive season for all of us. Armelle Girard brought the plants and trees to decorate the laboratory with more greenery and freshness. The other colleagues Laurent Korzeczek, Vanessa Verbeke, Gader Altinkurt, Hocine Lebbad, Carolina Baruffi, Alice Castan, Matthieu Degeiter, Francesca Boioli, Hakim Amara, Juba Hamma, Cora Moreira Da Silva, Alexandre Plaud, Henri Prévost, Lorenzo Sponza, Daniel Förster, Benoît Dabas, Etienne Carré, and Luis Eon, with whom I had a very good time these three years. I wish them all the best in the future.

Special thanks to all the colleagues in the MMC department at EDF R&D Les Renardières, they have also shown me the greatest kindness and warmth. Amina Benaceur, a very passionate person who has some deep thoughts on social issues. I really appreciate all the discussions we had on so many topics, from which I learned a lot and which helped me to enrich my cultural knowledge. The lunch break with Qiwei Shi, Georges-Arthur Debeire, Ziling Peng, Aboubakr Amzil and the others was a relaxing moment and we had many interesting conversations.

Finally, I would like to thank my family, my boyfriend and my friends. Your support is the most precious thing that has allowed me to pursue my studies and PhD in France. The distance cannot keep us apart because your care for me never fades and I always feel close to you. Thousands of words cannot express my feelings, because love for all of you is what I carry in my heart.

Contents

List of Abbreviations

BCC	Body-Centered Cubic
CS	Cross Slip
CPL	Crystal Plasticity Law
CPFEM	Crystal Plasticity Finite Element Method
DCM	Discrete-Continuous Model
DD	Dislocation Dynamics
EBSD	Electron BackScatter Diffraction
FCC	Face-Centered Cubic
FDM	Field Dislocation Mechanics
FEM	Finite Element Method
FR	Frank-Read
GB	Grain Boundary
GND	Geometrically Necessary Dislocation
HCP	Hexagonal Close Packed
HP	Hall-Petch
IB	Impenetrable Boundary
IQ	Image Quality
PBC	Periodic Boundary Conditions
RPV	Reactor Pressure Vessel
SEM	Scanning Electron Microscopy
SSD	Statistically Stored Dislocation
TB	Transparent Boundary
TEM	Transmission Electron Microscopy

Introduction

The assessment and management of materials ageing and degradation under irradiation are essential to ensure the safe long-term operation of nuclear power plants. The project SOTERIA brings together some of the most important international players in the field to build a reliable prediction platform for the light water reactors in service in Europe. This project aims at achieving multi-scale modeling of mechanical behavior for the steel components in the reactor pressure vessel.

For these steels, previous studies mainly focused on the issue of isotropic strain hardening associated with local strengthening mechanisms such as forest and irradiation defect interactions. The corresponding dislocation density based crystal plasticity laws (CPL) were developed and their use in FEM simulations allowed an accurate prediction of the macroscopic mechanical behavior under monotonic loading. However, some important features of plastic deformation involved in industrial materials are not taken into account, such as the deformation heterogeneities induced by grain boundaries (GBs) or the anisotropic properties of plastic deformation under cyclic loading. The main objective of this thesis is to improve these classical CPLs by accounting for some local features of plastic deformation.

To improve CPLs, the key is to understand the physical mechanisms at the origin of plastic heterogeneity. In this work, we propose to use Dislocation Dynamics (DD) simulations, now identified as a powerful technique allowing for quantitative description of mechanical properties at the mesoscopic scale. This method links the discrete properties of dislocation to the mechanical behavior of continuum crystal, which is an essential intermediate step in multi-scale modeling.

During the plastic deformation of polycrystals, an accumulation of polarized dislocations (GNDs) develops in the close vicinity of GBs. This particular organization of dislocations inside the grains induces an additional strengthening mechanism by introducing long-range stress field, i.e. back stress. This effect is grain size dependent and is known as the Hall-Petch (HP) effect. Though some phenomenological models were proposed in the literature, this effect is still poorly known. With the help of DD simulations, we investigate the physical origin of the HP effect in model polycrystals of

different grain size and shape. Based on the results of DD simulations, we propose a constitutive description for the prediction of back stress at low strain. The latter can be integrated into the existing CPL to improve the prediction of the mechanical properties. As the GB strengthening behavior is a general phenomenon for all polycrystalline materials, pure copper is chosen as our test case material since its properties have been well depicted in literature.

The dissertation is organized as follows:

In Chapter 1, the industrial context and scientific background are briefly presented. In particular, we summarize the previous work of PhD students made on RPV and internal steels. Then, the literature study is mainly focused on the GB strengthening behavior in polycrystalline materials. Next, we present some experimental results of the HP effect as well as the most well-known HP models. At last, we give a general presentation of the DD code used in this work.

In Chapter 2, the effect of grain size and grain shape on the flow stress in model aggregate grains is investigated. We consider grains of 1.25–10 μm size, three orientations ([135],[100] and [111]) and three shapes (cube, plate and needles). The influence of grain size is explored by considering simple periodic polycrystalline aggregates made of grains with cube, plate or needle shapes. We show that the HP effect is globally well reproduced with DD simulations. The HP constant is found a function of the grain orientations and shapes. A model is proposed to quantify the influence of the grain morphology.

In Chapter 3, the back stress generated by GNDs stored at GBs are characterized using DD simulations and it is shown that they constitute a strong strengthening mechanism for polycrystals. The significant accumulation of GND density is localized in a thin layer at GB and can be assimilated to a surface distribution of dislocations in GB facets. Internal stress field is found relatively homogeneous, particularly in the central area of the grain. The stress field associated to finite dislocation facets calculated with DD simulation is found quite different from the analytical solution existing in the literature for infinite dislocation walls. An efficient model is then proposed to predict the back stress induced by surface GNDs, in which the geometry of the GBs, the character of the dislocations and the GND density are all taken into account.

In Chapter 4, we show with the help of DD simulations that, at low strain, the evolution with plastic strain of the back stress is not sensitive to grain size. We show that the increase of back stress is directly related to the surface density of GNDs, which

can be calculated with a function proportional to the plastic strain. From this analysis, the independence of the HP constant K with plastic strain is derived. The observed size effect is simply related to the critical resolved shear stress (CRSS) that is derived at the beginning of the plastic deformation. The amplitude of CRSS is controlled by the initial dislocation microstructure we consider in the simulated grains. When theoretically the size effect reproduced by the simulations should be inversely proportional to the grain size, some relaxation processes in the smaller grains explain the existence of a power law relationship in agreement with the empirical HP law. Finally, an additional analysis of the pile-up model allows to provide some insights into the size effect in coarse-grained industrial material.

Chapter 1

State of the art

1.1 Industrial context

In recent years, the safety of nuclear energy has been again a public debate topic after some important events, such as the disaster in the Fukushima Daiichi nuclear plant in 2011, as well as the shutdown of the Doel nuclear reactor in Belgium in 2015. Facing the challenge of nuclear safety issue under economic impact, it becomes a major priority for regulators and nuclear power providers to extend the service time of existing plants beyond the anticipated time frame. In order to ensure a safe long-term operation of nuclear power plants, an European project SOTERIA was launched in 2015 bringing together some of the most important collaborators in the nuclear field. The aim of the project is to improve the understanding of aging problems in reactor structural components and to provide a predictive modeling platform for the evaluation and surveillance of safe nuclear exploitation.

The project SOTERIA is successor of two previous projects LONGLIFE and PERFORM60. The former was experimentally-oriented on the characterization of the microstructural and mechanical evolution of irradiated material under long-term exposure. The latter was focused on the development of a multiscale modeling framework to predict the mechanical properties of structural components in nuclear power plants. A significant progress was already made on the research of irradiation-induced aging phenomena, but they were mainly used as a support for observation and not for prediction. As to move forward to the management of nuclear power plants, we must be enabled with a robust prediction framework of ageing phenomena. To this end, several issues remaining unsolved so far need to be addressed. For instance, some observed phenomena requires a physically-justified model to achieve quantitative interpretation; on the other hand, then the proposed models need to be validated with smart experiences. Therefore, two complementary research fields involving both numerical and experimental approaches across relevant scales (from nano to macro scale) are coupled in project SOTERIA. The main features of this project is illustrated in Figure 1.1.

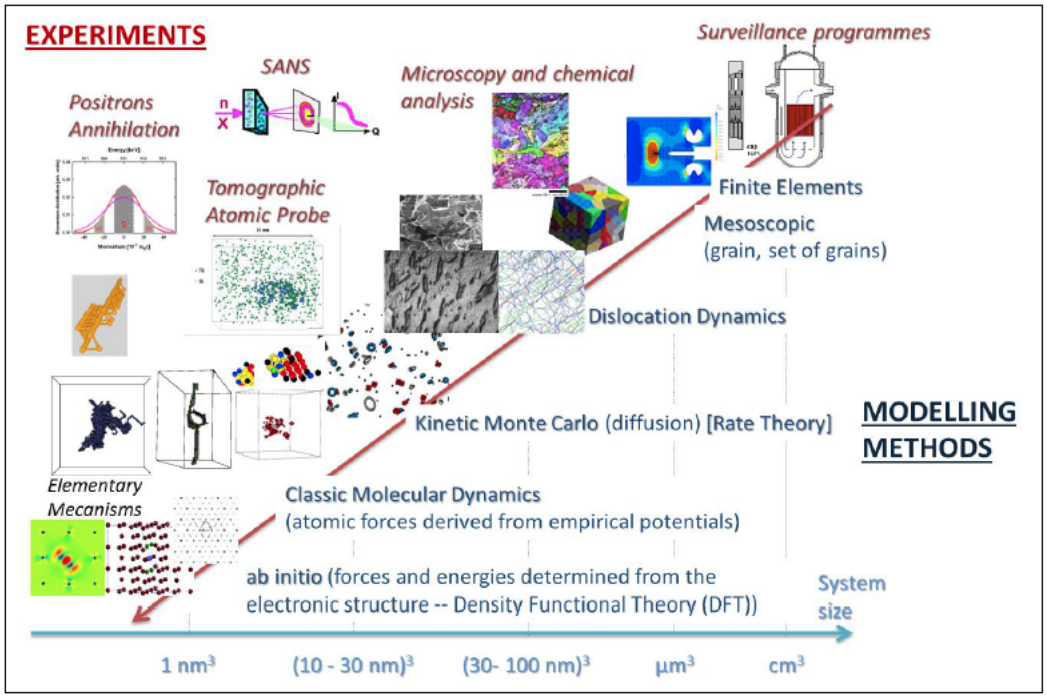

FIGURE 1.1: The project SOTERIA brings together multiscale modelings and experimental characterizations (http://www.soteria-project.eu).

1.2 Structural components in reactor pressure vessel

A nuclear power plant is a thermal power installation where heat source extracted from the fission of nuclear fuel is converted to electrical source. The production of electricity is not direct, several independent systems are coordinated to make the energy conversion take place in a cyclic way, see Figure 1.2.

The first system is the primary circuit composed of the reactor pressure vessel and the pressurizer. The main operation is transferring the thermal source from the reaction core to the steam generator through the circuit of coolant. The coolant may be water or gas or even liquid metal depending on the type of reactor. This primary circuit is in contact with radiation diffused from the fission of nuclear fuels, thus several measures are adopted to prevent the release of radioactivity into the environment:

- Zirconium alloys is used as the cover of the combustion fuel of uranium pellets because of its high resistance to corrosion and low absorption of thermal neutron

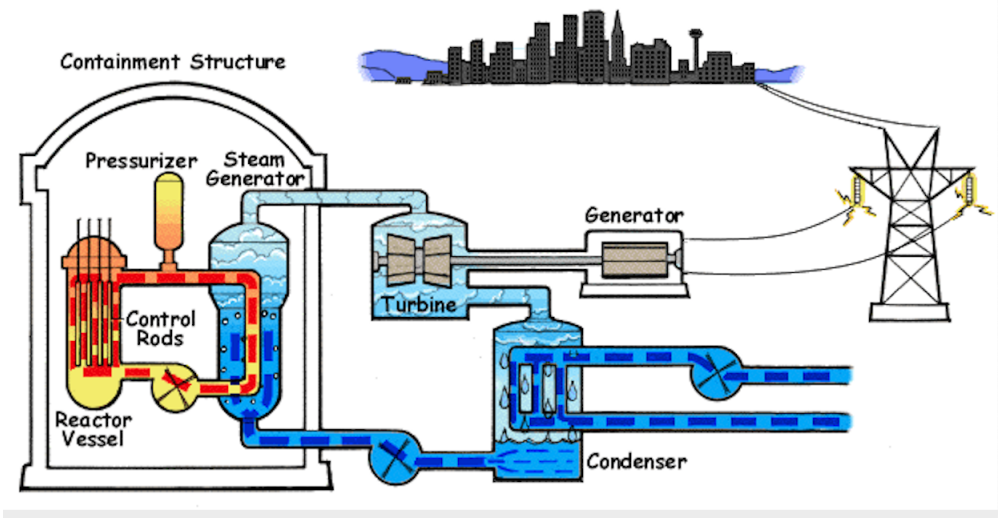

FIGURE 1.2: Working principle diagram of nuclear power plant. Image is issued from Wikipedia (https://en.wikipedia.org/wiki/Nuclear_power_plant).

- Reactor pressure vessel made from low-alloys steels cladding with stainless steels isolates the radiation produced from core fuel assembly
- Concrete dome is build up outside of the reactor to reinforce the protection against both internal and external impacts

The principal components in the secondary circuit are steam generator and steam turbine. The extraction of heat source from primary circuit allows the generation of steam. The heat energy of the steam is brought to the turbine and transformed into mechanical energy, which drives the electric generator to produce electricity. At last, the steam is cooled down into water through a condenser, which is usually alimented by cold water source from river or sea. Both the secondary circuit and the cooling systems are not exposed to radiation, thus not harmful to the environment.

In a nuclear power plant, the core structure is the reactor pressure vessel (RPV), in which the chain reaction of fuel assembly is occurring. The cross-section of a reactor pressure vessel is schematized in Figure 1.3. The dimension of a french RPV of 1300 MW capacity is 13.6 m high, 4.4 m in diameter and 22 cm thick in vessel shell (actual dimension could vary for different reactors). During the normal operation in service, the pressure inside the RPV is around 150 bar and the temperature of water varies from 293 °C to 329 °C between inlet and outlet nozzle.

To ensure the reliability of RPV, the issue of irradiation-induced ageing in RPV's structural components needs to be addressed. Two major structural components are

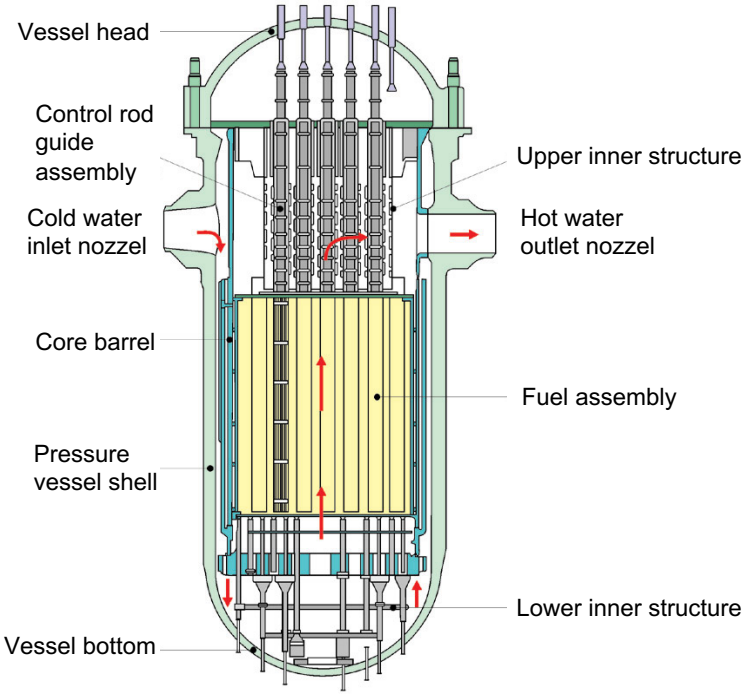

FIGURE 1.3: Cross section of reactor pressure vessel and its inner structures. Image is issued from Institut de Radioprotection et de Sûreté Nucléaire (Source: Didier Jacquemain/IRSN).

concerned: pressure vessel shell and inner structures. Both are made from steels of different grades. In nuclear material field, the steels used in RPV shell and inner structures are referred as RPV steels and internals, respectively. In a recent paper, modeling and experimental results of nuclear materials are reviewed in order to derive constitutive equations for calculating yield stress by taking into account the microstructure features of steels and the irradiation defects (Monnet, 2018).

In the following sections, a brief presentation will be made on the state of the art of the two steels. In particular, some experimental results of the characterization of microstructures in the received state will be detailed.

1.2.1 RPV steels

RPV steels are considered as the core structural component in a nuclear reactor. It ensures the integrity of reaction core assembly, controlling rods and other inner components in a confined cylinder. More importantly, it prevents the dispersion of radiation into the environment during the service lifetime of a RPV for at least 40 years. As RPV steels is the first barrier to ensure nuclear safety, a lot of work has been devoted to studying the properties of this material. On the experimental side, the influences of microstructure features, such as morphology and spatial distribution of crystallographic

orientations, on the local tensile behavior of RPV steels was analyzed (Sekfali, 2004). The heterogeneous microstructure of RPV steels was quantitatively characterized, more particularly, the effect of processing parameters on the formation of final microstructure was discussed (Diawara, 2011). The mechanical properties of RPV steels at microscopic scale was studied by *in situ* experiments, in which an effort was dedicated to improve the image processing techniques (Shi, 2018). On the numerical side, the plastic behavior of RPV steels was studied by DD simulations in both athermal and thermal regime (Queyreau, 2008; Naamane, 2008). A multiscale modeling taking into account the heterogeneous microstructure of RPV steels enabled defining a local micromechanical fracture criterion for crystallographic cleavage (Mathieu, 2006). The application of a large deformation crystal plasticity model using dislocation density as internal variables allowed the prediction of temperature-dependent local mechanical fields in RPV steels (Libert, 2007).

Steel of grade AISI A508cl3 or 16MND5 in French nomenclature is used for RPV shell. This material is a body-centered cubic low-alloyed steel. Its chemical composition is listed in Table 1.1. RPV steels are fabricated after several major steps; austenitization, quenching and tempering, the details of processing conditions are given in (Diawara, 2011). RPV steels consist of bainite and ferrite phases and exhibit excellent properties on strength and toughness.

C	Mn	Si	Cr	Ni	Mo	S	P	Cu	Al
0.25	1.29	0.23	<0.05	0.72	0.49	0.008	0.014	0.03	0.035

TABLE 1.1: Typical chemical composition of 16MND5 cast steel in mass percentage (%) (Libert, 2007).

With the help of different image acquisition techniques, the microstructure of RPV steels is illustrated in Figure 1.4. The size of ferrite grains is roughly ranging from 5 to 20 μm. The bainite laths are very fine around 1 μm. Usually, several bainite laths are grouped into bainite packets, which have the same size as ferrite grains. The identification of bainite laths and packets is determined by the crystallographic misorientation between the test regions. According to the measurements by Diawara (Diawara, 2011), the misorientation between bainite laths is several degrees (15 degrees accumulated across all the laths inside bainite packet), whereas the misorientation between ferrite grains and bainite packets is quite high, up to 60 degrees. A significant concentration of carbides in RPV steels, precisely in bainite phase, is shown in Figure 1.5. According to the different types of bainite, carbide clusters are formed in different sites varying from lath center to lath boundaries region.

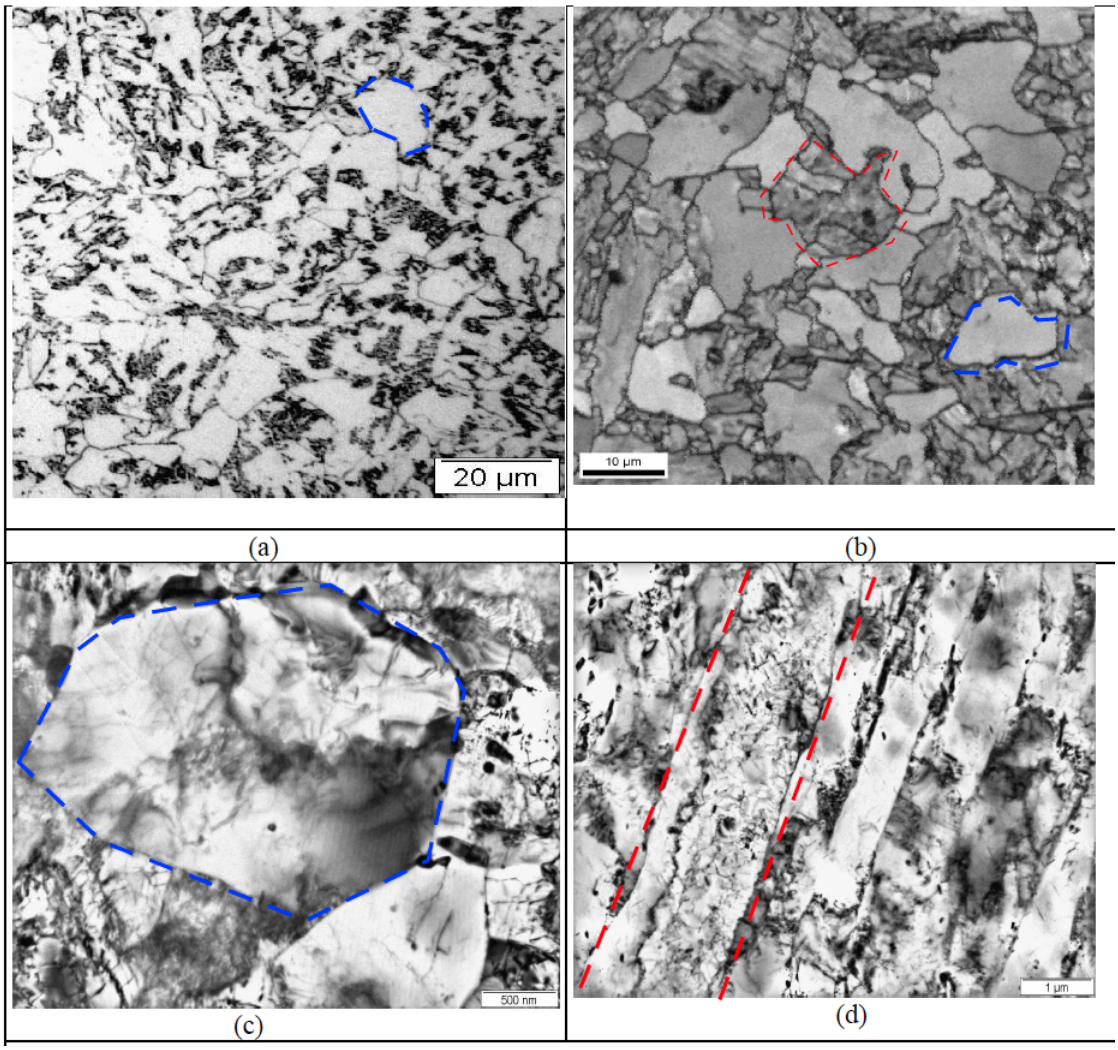

FIGURE 1.4: Microstructure of RPV steel includes a mixture of ferrite phase (in blue zone) and bainite phase (in red zone). (a) Optical micrograph. (b) Image quality (IQ) map constructed from EBSD. (c) Image of ferrite grain obtained by MET. d) Image of lath-like bainite obtained by MET. (Diawara, 2011)

Subjected to radiation, some irradiation-induced defects are emerged in RPV steels (Odette and Lucas, 1998; English and Hyde, 2012). The primary radiation defects are Solute Clusters formed of Cu, Mn, Ni, Si, and P. The secondary radiation defects include dislocation loops, small vacancy and interstitial clusters, etc.

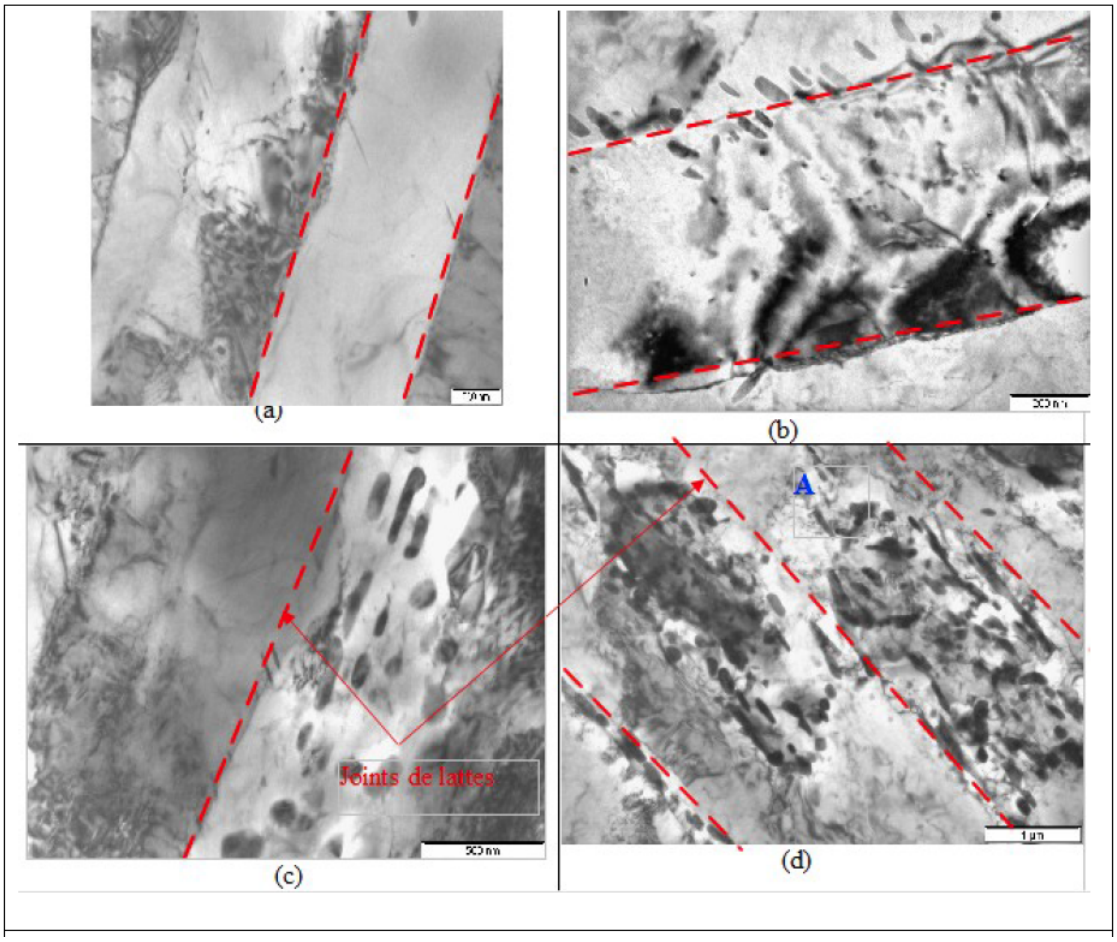

FIGURE 1.5: Distribution of carbides in bainitic laths. (a) Bainitic lath free of carbides. (b) Carbides concentrated on the lath boundaries. (c) Carbides precipitated in the central region, along the longitudinal direction. (d) Carbides precipitated in the central region and the lath boundaries region (Diawara, 2011).

1.2.2 Internals

Generally, structural steels used inside reactor vessels to hold together the fuel and control rod assemblies are named internals. The basic material of internals is austenitic stainless steel nominated usually as AISI 304 or 316 steel according to American standard AISI. The whole family of austenitic stainless steels has a face-centered cubic crystal structure and exhibits excellent resistance to corrosion. Furthermore, this material has good mechanical strength as well as high formability. Its structural stability allows its application in a large span of temperatures. Owing to the excellent properties of austenitic stainless steel, it is widely used not only in basic materials of everyday life but also in industrial infrastructures. In order to deepen understanding the mechanical behavior of such material, it has been the subject of a lot research work. Here, we comment several PhD projects made in the past few years. In 2004, Déprés used DD simulation method to analyze the persistent slip bands occurred in surface grains of

316L steel in order to understand the plastic mechanisms involved in crack initiation and then proposed a dislocation-based model for cyclic plasticity (Déprés, 2005). The sensibility of embrittlement of 316L steel to mercury was characterized by experiments and a correlation between mercury-induced crack localization and loading rate was identified (Medina Almazan, 2008). Quantification of the influence of surface roughness on crack initiation by thermal fatigue tests on 304L steels allowed to develop a fatigue criterion based on a micro/macro modelling approach (Pécheur, 2008). The formation of slip bands relating to the activation of slip systems having the greatest Schmid's factor was experimentally observed with low cycle fatigue tests on 316LN steel; furthermore, an improved crystal plasticity model with the introduction of geometrically necessary dislocations enabled a finer computation of local stress field (Schwartz, 2011). Thanks to targeted *in-vacuum* fatigue tests on 304L steel, the influences of parameters such as temperature, strain rate and strain amplitude on the damage kinetics were extensively investigated as to propose a fatigue life prediction accounting for environment factors (De Baglion, 2011).

Austenitic stainless steels have very low content of carbon that does not exceed 0.08% in mass percentage, which limits the formation of chrome-based precipitates. The principal alloy elements in austenitic stainless steels are chrome, nickel and molybdenum and they play an important role to increase the resistance to corrosion and enhance the formability. The main grades of austenitic stainless steels are classified with respect to alloy element contents, summarized in Table 1.2.

Grade	Cr	Ni	Mo	C	N
304	17-20	9-12	-	0.08	-
304L	17-20	9-12	-	0.03	-
304LN	18.8-20	9-12	-	0.04	0.08
316	16-19	10-14	2.3-2.8	0.08	-
316L	16-19	10-14	2.3-2.8	0.03	-
316LN	17-18.2	10-14	2.3-2.8	0.04	0.08

TABLE 1.2: Typical chemical composition of austenitic stainless steel of grades 304 and 316 in mass percentage (%) (Schwartz, 2011). L indicates low content of carbon, N indicates low content of nitrogen.

In the PhD project of Schwartz (Schwartz, 2011), the microstructure of 316LN steels as received state was characterized. EBSD analysis were carried out on a laminated plate underwent austenitization treatment between 1050 and 1150 °C followed by a hyperquenching. Cubic samples were extracted from two regions of the plate: interior and surface. The IQ maps captured in three directions (rolling, transverse and normal directions) on cubic samples are shown in Figure 1.6. It illustrated that the microstructure of 316LN steel was strongly heterogeneous with average grain size of 26 μm with standard

deviation 16 μm in interior region and they are 28 μm with standard deviation 21 μm on surface region. A few number of residual ferrite grains were measured but negligible in total quantity, the texture of 316LN steel could be considered as isotrope. This remark was in agreement with a previous observation in (Haddou, 2003). The majority is austenite phase having many annealing twins, the misorientation was characterized by a peak of values of 60 degrees. In austenite phase, the dislocation density observed by MET was about 2.1 $\times 10^{13} m^{-2}$.

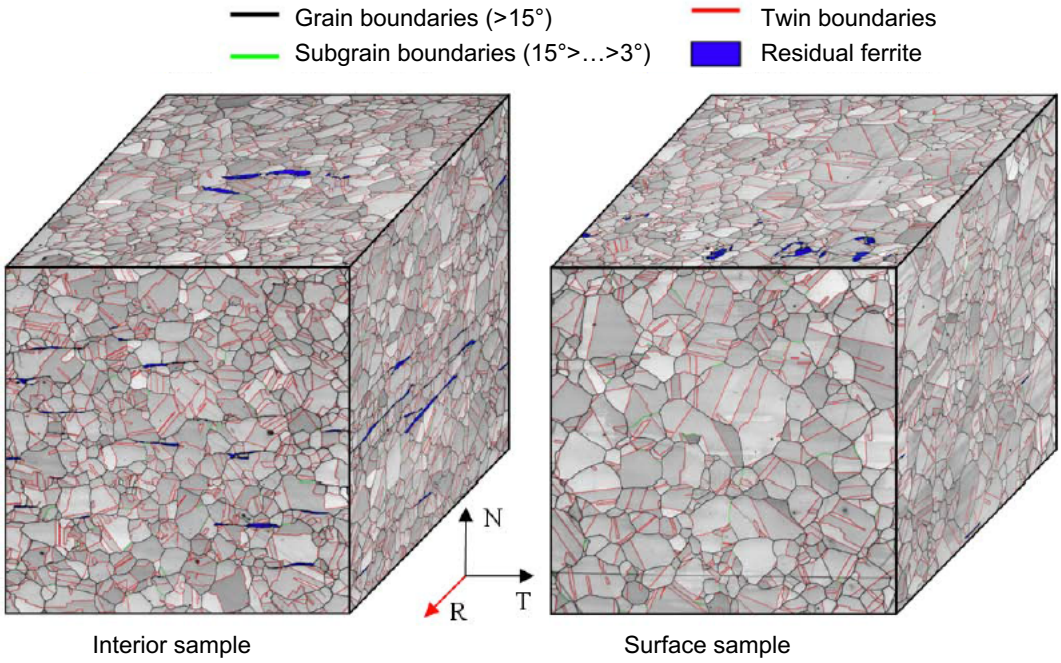

FIGURE 1.6: Image quality (IQ) maps constructed from EBSD on cubic facets normal to R (rolling direction), T (transverse direction) and N (normal direction): interior sample on the left, surface sample on the right. The dimension of cubic samples is 850 μm (Schwartz, 2011).

Subjected to radiation, the predominant irradiation defects emerged in austenitic stainless steels are faulted and perfect dislocation loops, cavities and unresolved spots (Garner et al., 1981; Zinkle, Maziasz, and Stoller, 1993).

1.3 Scientific background

EDF R&D develops crystal plasticity law (CPL) for the characterization of mechanical behavior of structural components used in RPV. Past developments were mainly focused on the question of isotropic strain hardening associated with local strengthening mechanisms such as dislocation forest and irradiation defect interactions. For FCC structure materials, a dislocation-density based CPL taking into account a full description of dislocation interactions strengths between different slip systems was established

(Kubin, Devincre, and Hoc, 2008; Devincre, Hoc, and Kubin, 2008). Dislocation Dynamics (DD) simulations were used to determine the corresponding hardening related to other microstructure features in nuclear materials, like dislocation loops and precipitates (Monnet, 2015b)(Monnet, 2015a). For ferrite of BCC structure, the principal phase in RPV steels, DD simulations were implemented to investigate of physical mechanisms controlling athermic (Queyreau, Monnet, and Devincre, 2009; Queyreau, Monnet, and Devincre, 2010) and thermally activated plastic deformation (Naamane, Monnet, and Devincre, 2010; Monnet, Naamane, and Devincre, 2011). A physically justified CPL synthesizing the results of the DD simulations, was thus developed from these foregoing work (Monnet, Vincent, and Devincre, 2013).

FEM simulations based on such CPLs allow for an accurate prediction of the mechanical behavior of single crystals under monotonic loading. However, the modeling of plastic deformation for industrial materials involves additional dislocation mechanisms such as the accumulation of polarized dislocations at grain boundaries (GB). This particular distribution of dislocations inside the grains of polycrystals is at the origin of additional strain hardening mechanisms and justifies the existence of long-range stress field, i.e. back stress. In most conventional crystal plasticity modelings, the effect of back stress on the strain hardening is usually calculated by introducing the field of second gradient of displacement into the constitutive equations. This type of calculation is complex and time-consuming, making it difficult to generalize to all industrial applications. In this work, in order to meet the industrial need to build a fast and reliable modeling framework, we try to propose a new approach for calculating back stresses. First, we will investigate the physics of back stress inside grains of polycrystal aggregate with different sizes and shapes. Then, based on the results of DD simulations, we will develop an original and efficient model to quantitatively calculate the back stress at low strain to improve the existing CPLs at EDF.

1.3.1 Effects of grain boundary

Heterogeneous deformation induced by GB

A polycrystal can be considered as the assembling of small crystals and each of them has a specific crystallographic orientation. Grain boundary (GB) is an interface area where the neighboring grains are joint together. At GB interface, the atoms are usually arranged into small connected facet to minimize the energy, see Figure 1.7. The effects of GB on the properties of materials are involved in many aspects: the electrical and thermal conductivity, preferred site of corrosion, precipitation of new phase, creep behavior etc. One of the most important effects of GB is increasing the mechanical strength by

inhibiting the motion of dislocations inside materials. Dislocation is an intrinsic defect of crystalline material and it is considered as the carrier of plastic deformation.

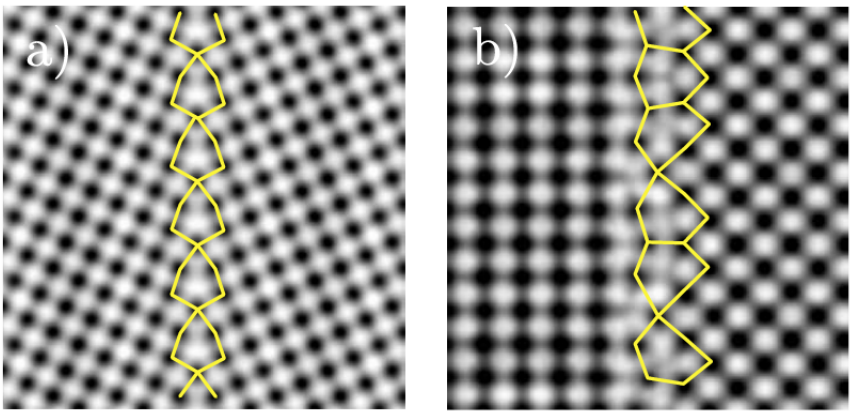

FIGURE 1.7: TEM image simulations of theoretical MgO models. (a) Σ 5(210)[001] symmetric tilt grain boundary and (b) (100)/(110)[001] asymmetric tilt grain boundary (Bean et al., 2017).

According to the misorientation resulted from two neighboring grains, GB is generally categorized into two types. The first type is Low-angle GB or Subgrain boundary having a misorientation angle lower than 15 degrees. They are made of regularly spaced dislocations allowing the transmission of dislocation under specific conditions (Shen, Wagoner, and Clark, 1988; Lee, Robertson, and Birnbaum, 1990; Kacher, Liu, and Robertson, 2011). The second type is High-angle GB having a misorientation angle higher than 15 degrees. In this case, the direct transmission of dislocation is somehow very difficult to take place. It needs to point out, GBs between ferrite grains in RPV steels and between austenite grains in internals are generally of high-angle (Diawara, 2011; Schwartz, 2011). At low strain, GBs are regarded as impassable barriers to the motion of dislocations that introduces a strong heterogeneity of deformation. When the strain increases, the plastic deformation of polycrystalline materials is accommodated by dislocation glide through adjacent grains with direct or indirect transmission of dislocations in the vicinity of GBs (Hingwe and Subramanian, 1975; Shen, Wagoner, and Clark, 1986; Baillin et al., 1987; Shen, Wagoner, and Clark, 1988). In some recent numerical studies, taking into account the transmission of dislocations across GB has an effect on the evolution of dislocations and subsequently the strain hardening behavior (Fan et al., 2015; Stricker et al., 2016; Hamid et al., 2017).

Any obstacle to the gliding of dislocations is a potential source of deformation heterogeneity. Depending on the nature of obstacles, they are more or less difficult to overcome. The main cause of deformation heterogeneity in polycrystalline materials

results from the presence of GBs limiting the free expansion of dislocations. The accumulation of dislocations against GBs has been observed by experiments (Haddou, 2003; Schwartz, 2011). Unlike the dislocation storage occurring inside single crystals at low strain, the dislocations accumulated at GBs of polycrystals are polarized, i.e. the resulting Burgers vector is non zero. This particular population of dislocations is called geometrically necessary dislocations (GND), to be distinguished from other dislocations, called statistically stored dislocations (SSD) (Ashby, 1970). SSDs are mainly responsible for isotropic hardening while GNDs are involved to accommodate the deformation incompatibility imposed by microstructure. According to Ashby, the density of SSDs is a characteristic of "*material*" while the density of GNDs is "*microstructure*" dependent. Since the role of these two types of dislocation density differs in strengthening and strain hardening, their effects should be separately taken into account for crystal plasticity modeling.

The stack of dislocations close to GBs leads to a heterogeneous distribution of dislocations density inside grains. This arrangement of dislocations is more pronounced in ultrafined materials (Calcagnotto et al., 2010). For instance, TEM observations showed the dislocation density localized in lath boundary areas was significantly higher than dislocation density in lath interior (Caballero et al., 2011; He et al., 2018). In the PhD work of Daveau, the laue microdiffraction technique was used to estimate the evolution of GND density in compression test on a tricrystal copper sample (Daveau, 2012). In a 0.2% deformed grain with one activated slip system, the increase of GND density in the close vicinity of GB was 2 to 4 times higher than in the interior region. It has been demonstrated that the apparition of long-range stress field is related to the storage of GND density.

Influence of GB on mechanical properties

The mechanical properties of polycrystalline materials are strongly influenced by the GBs. When more GBs are formed inside a polycrystal, grain size becomes smaller and mechanical strength increases subsequently. Therefore, the GB strengthening behavior gives rise to the well-known size effect that affects both flow stress stress and strain hardening of polycrystals. In this section, the mechanical behavior influenced by GBs under monotonic and cyclic loading will be briefly presented.

Tensile tests were performed on 316L steel, the work hardening rate is plotted with flow stress in Figure 1.8. The work hardening behavior could be divided into three distinguished stages (Haddou, 2003; Feaugas and Haddou, 2003).

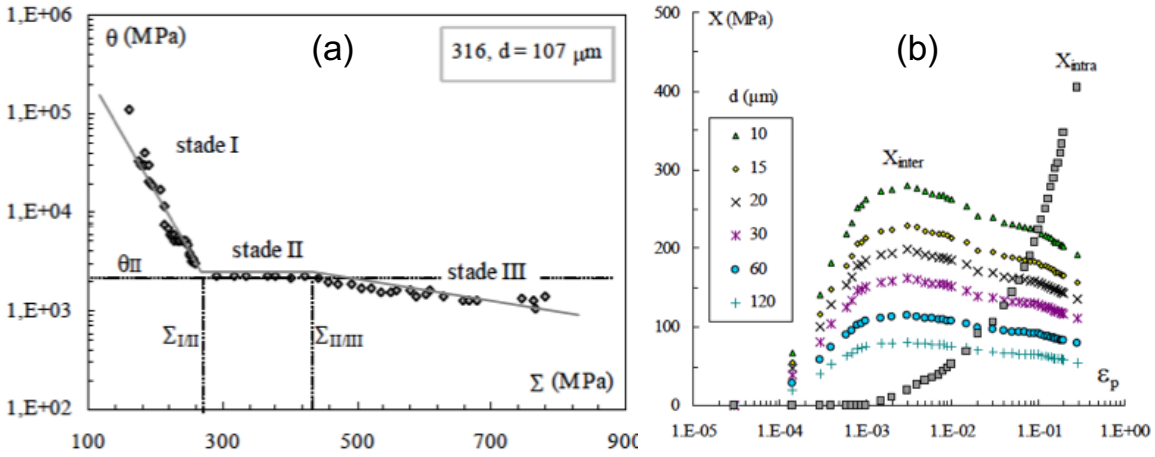

FIGURE 1.8: (a) Evolution of the work hardening rate as a function of flow stress for 316L steel. (b) Evolution of intergranular and intragranular back stress with plastic strain in 316L steels (Haddou, 2003).

– In stage I, the activation of single slip and planar slip is observed in more than 50% of grains. The increase of flow stress is mainly induced by internal long-range stresses due to the storage of dislocations at GBs including the formation of dislocation pile-ups. Such internal long-range stress is considered as intergranular back stress originated from strain incompatibility between adjacent grains. There is no evidence of significant intragranular internal stress in the early stages of plastic strain without the formation of heterogeneous dislocations structures inside grains.

– In stage II, the work hardening rate is constant with flow stress. The cause to such phenomenon resulted from two aspects. On one hand, the simultaneous activation of multiple slip and cross-slip reduces intergranular internal stresses leading to a stress relaxation. On the other hand, intragranular internal stresses increase significantly when heterogeneous dislocation structures (clusters, walls and cell) are formed inside grains. The constant increase of flow stress is an outcome of a balance between these hardening and softening effects.

– In stage III, the increase of flow stress is slowed down due to the process of dislocation annihilation. The effect of intragranular internal stresses surpasses the intragranular internal stress, but the work hardening rate of the latter back stress component decreases.

In this work, we focus on the study of GB strengthening behavior at low strain limited in stage I and II. At lower strain, the GB strengthening behavior is reflected by the influence of grain size on the evolution of flow stress with plastic strain. As can be seen

in Figure 1.9, the amplitude of flow stress is higher while grain size is smaller for both nickel and 316L steel. The phenomena of *smaller is stronger* holds true from the beginning of plastic deformation until 30% of plastic strain. It justifies that the mechanical properties of materials are dominated by grain size. From submicron to micron scale, similar grain size effect exists in FCC, BCC and HCP materials.

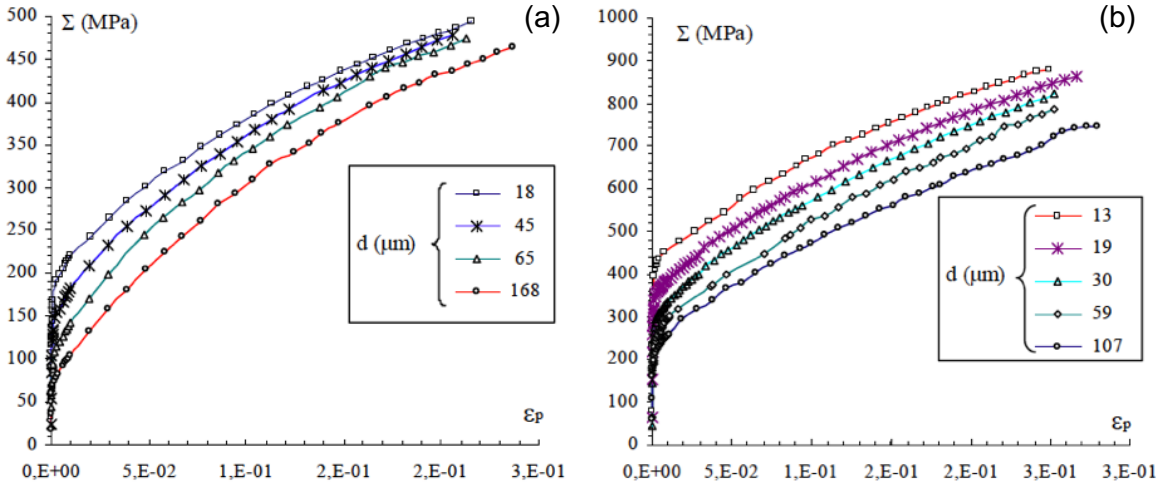

FIGURE 1.9: Stress-strain curves for (a) pure nickel and (b) 316L steel of different grain sizes (Haddou, 2003).

In the case of polycrystals under cyclic loading, some particular mechanical properties are associated with GBs as well. The cyclic strengthening behavior of material is dependent on applied loading and deformation history due to the collective properties of dislocations evolved during deformation. The critical stress for the irreversible propagation of dislocations in a given microstructure is decomposed into two stress contributions. The first is isotropic hardening component resulted from the resistant shear stress located in a short range. The second is kinematic hardening component resulted from long-range stress depending on the history and direction of movement of the dislocations. This notion of decomposition of stress is firstly proposed by Cottrell (Cottrell, 1953) and the followers further developed this methodology for the crystal plasticity modeling in solid materials (Lemaitre and Chaboche, 1994). Although frequently discussed in the literature, the physical mechanisms behind kinematic hardening are not fully understood. One of identified mechanisms is related to the back stress generated by GNDs in thin structured layers or close to GBs (Xiang and Vlassak, 2005; Bouaziz, Allain, and Scott, 2008; Hu et al., 2017).

Among the manifestations of the kinematic hardening in crystalline materials, the effect of loading asymmetry such as the Bauschinger effect is well-known in loading-unloading test. For instance, when the loading direction is reversed on a pre-deformed

metal by tension, usually the yield strength in compression is lower. This is a common mechanical property found in most of cold-worked metals and it is mainly induced by the back stress associated with GND density. In the work of (Schwartz, 2011), low cycle fatigue tests were carried out on 316LN steels and the Bauschinger effect was identified as shown in Figure 1.10.

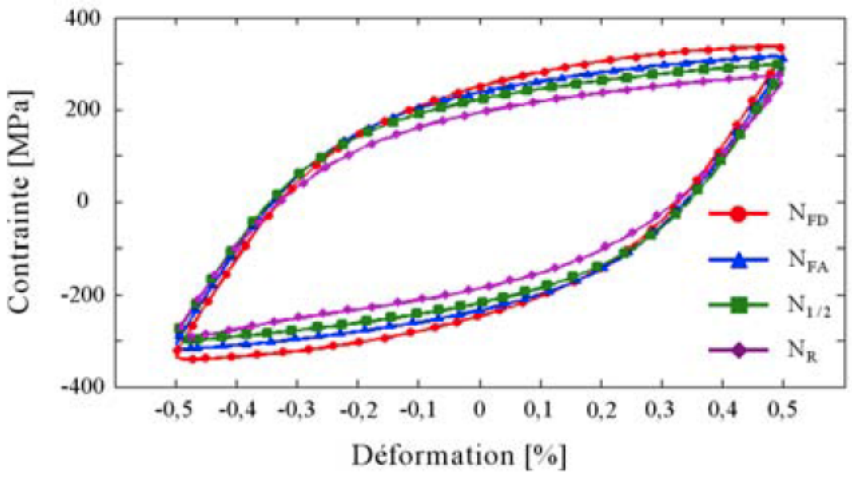

FIGURE 1.10: Hysteresis loops for 316LN steel with $\Delta\varepsilon/2 = 0.5$ % (Schwartz, 2011). N_{FD}=20 cycles, N_{FA}=200 cycles, $N_{1/2}$=5×10^3,N_R=10^4.

1.3.2 The Hall-Petch effect

Since the discovery of Hall and Petch about the grain size effect on the mechanical properties of mild steels (Hall, 1951; Petch, 1953), much progress has been made on the optimization of material properties. In the majority of cases, for grain sizes between one tenth of micrometers and a few hundreds of micrometers, the yield stress of polycrystals increases as the grain size decreases. Then the validity of grain size dependence strengthening is extended from yield stress to flow stress along plastic deformation stage (Armstrong et al., 1962). This grain size effect is classically described using a phenomenological law named as Hall-Petch law:

$$\sigma_y = \sigma_0 + \frac{K}{\sqrt{d}} \tag{1.1}$$

where σ_y is flow stress, σ_0 is the necessary yield strength required for the movement of dislocations in a large single crystal, d is the characteristic grain size and K is commonly considered as a material constant. Experimental studies have demonstrated the existence of the Hall-Petch (HP) effect for a wide span of metals and alloys (Hansen, 2004; Armstrong, 2014; Cordero, Knight, and Schuh, 2016). Nonetheless, the modeling of this phenomenon is still based on strong assumptions. The existing HP models differ

mainly in the nature of the hardening mechanism described within the grains. However, the identification of underlying physical mechanism to the HP effect is still a matter of debate. Polycrystals are assumed made of grains whose size and shape are relatively homogeneous and uniformly distributed. However, the true microstructure of polycrystalline materials is generally complex. For instance, many industrial materials have an anisotropic granular morphology. In RPV steels, bainite laths of non-equiaxed shapes are wrapped into packets (Diawara, 2011). In some ultrafined polycrystals, the grains have elongated shape and arranged into arrays of strips or needles (Tasan et al., 2015). The study of the influence of grain shape on the mechanical properties of polycrystal is therefore an important issue.

In the following, we will give a general presentation of the Hall-Petch effect in polycrystals across grain size scales. Then, we summarize the classical models for the Hall-Petch law.

General presentation

According to the Schmid law, plastic strain in polycrystals initiates in the grains which are the most favorably oriented in relation to the loading direction. Thus, at low strain, only slip systems with the highest Schmid factor in some grains are activated. With increasing deformation, plastic slip is then propagated into the other grains of polycrystal. At room temperature and in ductile bulk materials, plasticity is controlled by the conservative motion of a small fraction of dislocations. Dislocations glide on different slip planes inside the grains promotes the mutual interaction of dislocations and the formation of junctions. Since the mobility of dislocation is reduced, such mechanism leads to a hardening behavior commonly named as forest hardening (Saada, 1960). The critical stress derived from forest hardening is formulated by Taylor equation (1934) as a function of dislocation density:

$$\tau_c = \alpha \mu b \sqrt{\rho} \tag{1.2}$$

where α is a coefficient representing for average strength of short-range interactions between dislocations. For FCC materials, $\alpha = 0.35 \pm 0.15$ was computed with the help of DD simulations (Madec, Devincre, and Kubin, 2002).

Besides the motion of dislocations is slowed down in forest network, mobile dislocations can be stopped by obstacles. Among all kinds of obstacles, at low and intermediate applied stress levels, the GBs act as hard interfaces that generally block the transmission of dislocations from grain to grain. Hence, to further deform a polycrystal, one must increase applied stress to generate new mobile dislocations. The process of dislocation

multiplication results in the work hardening of materials. This analysis allows us to deduce that effect of GBs is directly related to mechanical strength. Inside a given bulk material, when there are more GBs, the whole structure is divided into smaller grains and thus the higher applied stress is required to move dislocations to deform the material. For the grain size at the micrometer scale, such property obeys to the classic HP law in Eq. 1.1.

Advances in material manufacturing process enable the fabrication of materials with severe grain refinement down to the grain size at submicron and nano scale. The longtime recognized notion of *smaller is stronger* has been challenged by controversial mechanical properties (Kumar, Swygenhoven, and Suresh, 2003). For the ultrafined polycrystals having grain size smaller than 100 nm, flow stress continues increase with decreasing grain size but no more proportional to $\sqrt{d}$. When grain size is down to 10 nm, the conventional HP effect breaks, a weakening effect appears when decreasing the grain size. Such phenomenon is schematized in Figure 1.11, however the limit grain size for an inverse HP effect is reported with scattered value in literature (Meyers, Mishra, and Benson, 2006).

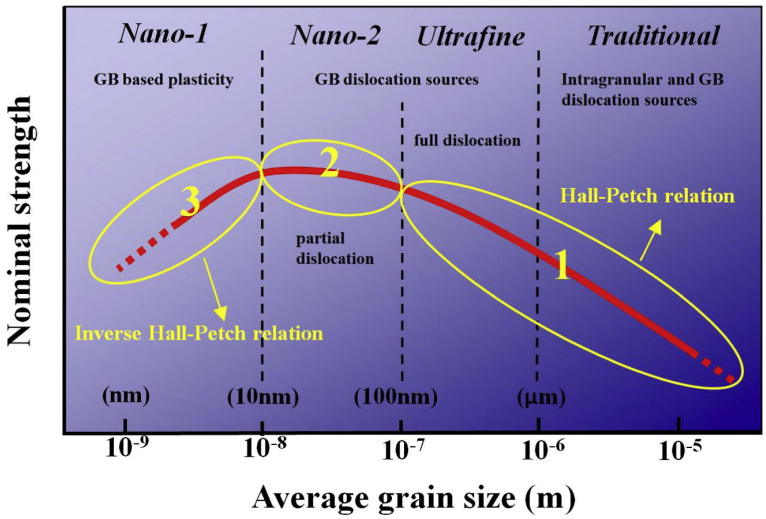

FIGURE 1.11: Schematic representation of the variation of nominal strength as a function of grain size across wide scales (Zhang, Lu, and Tieu, 2016). GB plays a significant role on influencing the mechanical property of polycrystalline materials.

Based on the observed size depending behavior in a wide range of grain sizes, an alternative power law equation is proposed:

$$\sigma_y = \sigma_0 + Kd^m \tag{1.3}$$

where σ_y, σ_0 and K have the same definition as in Eq. 1.1. However, the H-P exponent, m, becomes a variable sensitive to the scale of grain size. It is generally given as $m = -1/2$ for coarse-grained polycrystals, $m \approx -1$ in ultrafined polycrystals and $m \approx 1$ for nano-polycrystals. The size effect of polycrystals across scales illustrated in Figure 1.11 suggests that the GBs have an important impact on deformation behaviors.

The classical Hall-Petch law ($m = -1/2$) is well respected in most coarse-grained metals and alloys. The grains are large enough to contain a high initial dislocation density, hence there are enough dislocations sources to satisfy the imposed deformation rate. There is a change in slope (exponent m) for ultrafined polycrystals with grain sizes between 100 and 10 nm in Figure 1.11. This change in HP exponent can be explained by a transition of elementary mechanisms that control plastic deformation. The plasticity of coarse-grained polycrystals is mainly dominated by traditional mechanisms, such as the multiplication of dislocations from forest network. The accumulation of dislocations at GBs introduces back stress to strengthen materials. However, when grain size refines to the submicron scale, the multiplication of dislocations requires high stress in order to bow out shorter pinned source similar to Frank-Read source (Frank and Read, 1950). The accumulation of dislocations at GBs is less important and the flow stress is rather characterized by the necessary strength to overcome the line tension of dislocations (Foreman, 1967). The critical stress to the free expansion of Frank-Read source is approximated as:

$$\tau_c \simeq \frac{\mu b}{R} \simeq \frac{\mu b}{d} \tag{1.4}$$

where R the radius of critical dislocation curvature of a semi-circle. R is proportional to the grain size d since FR sources are confined within ultrafined grains. The critical stress is then dominated by grain size d and the power component in Eq. 1.3 tends to $m = -1$. This type of grain size strengthening is often referred to as the single source strengthening (Parthasarathy et al., 2007; Zhou, Beyerlein, and Lesar, 2011).

When grain size goes down to tens of nanometer, GBs strongly influence the deformation behavior where the inverse HP effect is found. As the grain size is extremely refined, few even none dislocation sources are included inside grains. In this case, GBs are no more barriers to the motion of dislocation but becomes the reservoir of dislocations. An important quantity of dislocations are nucleated from GBs and propagates through grains (Schall et al., 2006; Li et al., 2015). Another dominant mechanism responsible for the inverse HP effect is GB sliding (Conrad, 2004).

The Hall-Petch models

As the average grain size in RPV and internal steels is at the micrometer scale, we will restrict our studies on the conventional HP effect. Classical models for the HP law are presented in the following. The aim is to establish a fundamental understanding of the physical mechanisms controlling the HP effect.

- The pile-up model

In a dislocations pile-up configuration, a shear stress τ is imposed to stack dislocations against GB. Each dislocation exerts back stress in their glide plane opposed to dislocation multiplication. After stacking n dislocations, the dislocation source and the dislocation pile-up reach equilibrium and their dynamics are stopped. Thus, to continue to deform the grain, larger stress must be applied to overcome back stress. A grain size d depending relationship is established between number of dislocations in pile-up n and applied shear stress τ: $n = \pi d\tau/\mu b$.

The stress concentration at the head of pile-up leads to the slip propagation through direct or non direct transmission of dislocation. A critical stress $\tau_c = n\tau$ is defined for activating plastic deformation in adjacent grains. Combination of the n and the τ_c allows to obtain an equation giving the applied shear stress τ needed to deform all the grains as function of the average grain size, d. This equation justifies the H-P law:

$$\tau \approx \sqrt{\frac{\tau_c \mu b}{\pi d}} = \frac{K}{\sqrt{d}} \tag{1.5}$$

- The slip distance model

The Taylor equation 1.2 defines the yield stress in ductile bulk materials as a function of the dislocation density. Also, for geometrical reasons, the mean slip distance of dislocations in a polycrystal must be at low dislocation density in the same order of the grain size d. Then, the dislocations generated during deformation do not annihilate each other until reaching GB. The relationship between the storage rate of dislocations density and the grain size is derived from Orowan equation: $d\rho/d\gamma = \beta/bd$. Finally, replacing ρ in Taylor equation, we obtain an equation justifying the H-P law:

$$\tau \approx \alpha\mu\sqrt{\frac{\beta b\gamma}{d}} = \frac{K(\gamma)}{\sqrt{d}} \tag{1.6}$$

- The GND model

The grains inside a polycrystal have random crystal orientations, so they are more or less deformed undergoing the imposed loading. To accommodate the strain incompatibility developed between adjacent grains, a number of dislocations with the same sign of Burgers vector are lined up at the GBs. These dislocations are named as GNDs by Ashby (Ashby, 1970).

If we admit that n GNDs are needed to accommodate the GB misorientation, the corresponding plastic strain can be calculated from the Orowan equation. In the case of cubic grains, the GND density at GB with low misorientation degree is $\rho_{GND} = 4n/d^2 = 4\gamma/bd$. Then, substituting GND density into the Taylor equation 1.2 results into an equation justifying the H-P law:

$$\tau \approx \alpha\mu\sqrt{\frac{4b\gamma}{d}} = \frac{K(\gamma)}{\sqrt{d}} \tag{1.7}$$

To summarize, the two terms σ_0 and Kd^m involved in HP law of Eq. 1.1 are treated separately in these models. The first term σ_0 accounts for the strengthening effects unrelated to grain size. The second term is attributed to grain size strengthening, in which HP constant K and HP power component m are encoded with different hypothesis of deformation mechanism. In the pile-up model, K is considered as constant while in another two models, K varies as a function of plastic deformation γ, listed in following table 1.3:

	Pile-up model	Slip distance model	GND model
m	$\frac{1}{2}$	$\frac{1}{2}$	$\frac{1}{2}$
K	$\sqrt{\tau_c\mu b/\pi}$	$\alpha\mu\sqrt{\beta b\gamma}$	$\alpha\mu\sqrt{4b\gamma}$

TABLE 1.3: Parameters of the three principal Hall-Petch models.

In the literature, research work on the HP effect is extremely rich. We have presented here only the basic characteristics of the HP effect, including the most known HP models. Further comments and discussions on the effect of HP will be given in the following chapters so as to address some specific issues.

1.4 Dislocation Dynamics simulations method

The evolution of computer technologies and algorithmic methods makes it possible to carry out computationally intensive simulations. Among the simulation methods that have been developed rapidly in recent years, Dislocation Dynamics (DD) is no doubt one of the most important techniques for plasticity modeling. DD simulations have been

developed to study the dynamics, interactions and collective properties of a population of dislocation lines over time. This simulation method reproduces the plastic deformation of crystalline materials in a physically-justified way at the scale of several tens of micrometers down to the atomic scale.

The plastic deformation of crystalline materials is essentially controlled by the motion and interaction of dislocations in the crystal. DD simulation is performed at mesoscopic scale, which is an intermediate scale linking the elementary properties of dislocations to continuous approaches with deformation and stress fields described in representative volume element at macroscopic scale. Owing to the increase in computing power, DD simulations have evolved from 2D to 3D. 2D approaches are obviously easier to implement with a reduced computation time, but its geometry is too simplified. It does not allow for simulating all the properties of a realistic dislocation density. 3D approaches take into account precisely the effects of line tension as well as interactions at short distances between dislocations. These simulations are therefore much more realistic and allow us to be quantitative.

1.4.1 Calculation procedure

The DD simulation code *microMégas* (*mM*), developed at the LEM CNRS-ONERA, was used in my PhD project. This code allows the performance of 3D DD simulations with finite or periodic boundary conditions. At the same time, the important parameters for plasticity modeling are all recorded during simulations, such as dislocation density and internal stress field etc. In the context of my work, this code offers the essential possibility to investigate the deformation behavior of grain aggregates.

A detail description of the principles of the *mM* code is documented in (Devincre et al., 2011). Its calculation procedure can be schematically into four main steps:

- An initial configuration is constructed from a population of randomly distributed dislocation sources. The dislocation lines are discretized into a succession of elementary segments. For each time step, the positioning of dislocations is updated in space while respecting the characteristics of the crystal lattice.

- An effective stress calculation on each dislocation segment is performed using analytical formulas from the elastic dislocation theory. This effective stress is the result of stress imposed by loading associated with all dislocation segments present

in the simulated volume.

- The prediction of the movement of the set of dislocations is controlled by a mobility law. This step requires, at each time step, information of the stress field for the dislocations in the simulated volume.

- Local rules are eventually applied to reproduce certain properties of the dislocation core, such as the cross-slip of the screw dislocations.

1.4.2 Strain compatibility

The microstructure of polycrystals is usually very complex, for a first approach we can consider that a polycrystal is composed of several grains perfectly assembled by GBs. As each grain differs from the others in size, shape and crystal orientation, a heterogeneity of grain deformation develops in the polycrystal during its deformation. In conventional DD simulations, GB acts as a rigid interface between two adjacent grains. The presence of this interface therefore induces a necessary internal stress to satisfy the condition of mechanical equilibrium and cohesion of the polycrystal.

In the current study, for reasons of simplicity, the formalism of small deformation is used in the simulated grains. The simulation material is considered as elastically isotropic. The latter hypothesis implies that all grains deform homogeneously in the elastic regime and that no internal stresses are introduced during elastic deformation. On the other hand, the problem of plastic strain incompatibility, which is the most important phenomenon, is automatically taken into account here with DD simulations. Indeed, during plastic deformation, the grains rotate and change shape resulting from the motion of dislocations. Plastic deformation discontinuity therefore gradually develops between neighboring grains. The image of figure (1.12 (a)) illustrates an initial state of a bicrystal. We assume that each grain of the bicrystal can deform independently as shown in Figure (1.12 (b)). Shape differences will quickly appear during deformation and the cohesion of the polycrystal is no longer possible since each grain are deformed differently. In reality, the misorientation induced by the plastic deformation between adjacent grains is accommodated by the dislocations of same sign lined up in Figure (1.12 (c)). The dislocations are classed as GND and they ensure the cohesion of the material.

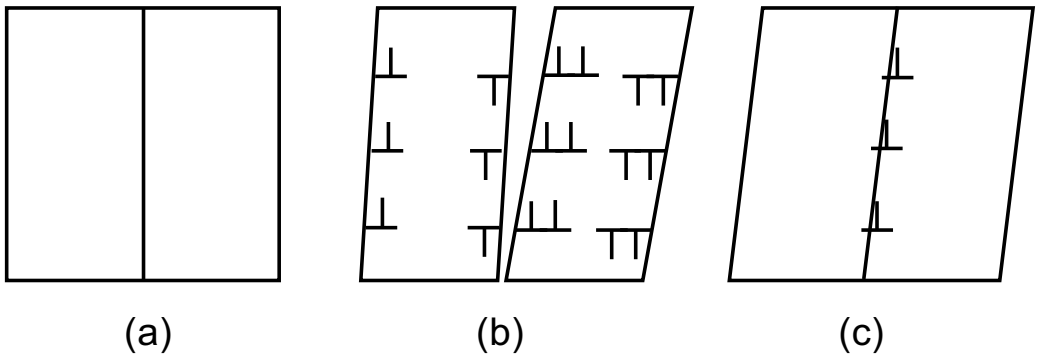

FIGURE 1.12: A schematic illustration of plastic deformation for an infinite bicrystal. (a) Initial state. (b) Shape variation of the independent grains. (c) Accommodation of misorientation induced by the plastic deformation.

Considering a GB is localized between two neighboring grains, dislocations emitted from two grains are accumulated on both sides of the GB. It's quite possible for dislocation of the positive sign on one side of GB encounters dislocation of the negative sign on the other side of GB. This pair of dislocations with opposite sign annihilates the stress field of each other and we call them elastically screened. These screened dislocations do not generate long-range stress field. The other accumulated dislocations do not meet the stress annihilation condition, so the stress fields generated by these dislocations are not screened. In fact, these unscreened dislocations are GNDs and that give rise to strong internal stress that allows the polycrystal to sustain the continuity. No additional conditions need to be integrated in DD simulations to ensure plastic strain compatibility, because GNDs are naturally taken into account within the evolution of crystalline microstructure.

Chapter 2

Effects of the grain size and shape on the flow stress

Reproduced from: Jiang, M., Devincre, B., Monnet, G., 2019. Effects of the grain size and shape on the flow stress: A dislocation dynamics study. Int. J. Plast. 113, 111–124.

Dislocation dynamics simulation is used to investigate the effect of grain size and grain shape on the flow stress in model copper grains. We consider grains of $1.25 - 10\ \mu m$ size, three orientations ([135], [100] and [111]) and three shapes (cube, plate and needles). Two types of periodic aggregates with one or four grains are simulated to investigate different dislocation flux at grain boundaries. It is shown that in all cases the flow stress varies linearly with the inverse of the square root of the grain size, with a proportionality factor varying strongly with the grain orientation and shape. Simulation results are discussed in the light of other simulation results and experimental observations. Finally, a simple model is proposed to account for the grain shape influence on the grain size effect.

2.1 Introduction

Intensive research has been dedicated to the effect of grain size on the mechanical properties of metals and alloys (Armstrong, 2014; Cordero, Knight, and Schuh, 2016; Lasalmonie and Strudel, 1986; Li, Bushby, and Dunstan, 2016). At the beginning of 1950, Hall (Hall, 1951) used the dislocation pileup model proposed by Cottrell (Cottrell, 1953) to explain the relation observed experimentally between the lower yield stress of mild steels and the grain size, d. This relation is recognized today as the Hall-Petch (HP) law:

$$\sigma_y = \sigma_0 + Kd^{-1/2} \tag{2.1}$$

where σ_0 is a reference stress generally called friction stress and K the HP constant. In the following, the quantity $Kd^{-1/2}$ is called the HP term. Some years later, Petch (Petch, 1953) has shown that the cleavage stress of mild steels also varies consistently with the HP law and Armstrong *et al.* (Armstrong et al., 1962) provided evidence that the HP law applies to the whole stress-strain curve and remains valid for most polycrystalline metals and alloys. It was also shown by Conrad and Schoeck (Conrad and Schoeck, 1960) and Petch (Petch, 1953) that the HP law applies to BCC metals at low temperature, with a temperature quasi-independent HP constant. In some experiments, K is found to be constant or to slightly decrease with deformation in BCC (Pechkovskii et al., 1989; Tsuchida et al., 2008), FCC (Feaugas and Haddou, 2003; Meyers, Andrade, and Chokshi, 1995) and HCP (Chia, Jung, and Conrad, 2005) metals and alloys. However, Cordero *et al.* have shown that some pure metals show an opposite behavior with increasing K with deformation. On the other hand, Li *et al.* (Li, Bushby, and Dunstan, 2016) have shown that statistical analysis of the ensemble of experimental data on the Hall-Petch effect does not allow discriminating between the dependencies on $1/d$, $1/d$, $\ln(d)/d$, etc. This has been attributed by Li *et al.* to the dispersion of results and the experimental errors in determining the grain size.

While the grain size effect applies to many mechanical properties of crystalline materials (including microhardness (Hughes et al., 1986)), several phenomenological rationalizations are possible (Hirth, 1972). Among the different interpretations, one can cite *dislocation pileup* models (ex. (Navarro and Rios, 1988; Smith and Worthington, 1964)), which refer to the original mechanism proposed by Hall and assume a stress concentration at the head of the dislocation pileup leading to the deformation propagation to the neighbouring grain by either activating dislocation sources in the next grain or enabling the transmission of dislocation across the grain boundaries (GBs). The *incompatibility-type* model relies on the original work of Ashby (Ashby, 1970) who

introduced the concept of Geometrically Necessary Dislocations (GNDs) versus Statistically Stored Dislocations (SSDs). Such models interpret the HP effect as a result of the GND accumulation, necessary to accommodate strain incompatibility between grains. In this approach, the HP constant K is proportional to the square root of the plastic strain. However, Cordero *et al.* (Cordero, Knight, and Schuh, 2016) have shown that even in the cases where K increases with deformation, the increasing rate is not found to follow a square root. Also, Li *et al.* (Li, Bushby, and Dunstan, 2016) has pointed out another serious concern about this type of models: as K goes to zero in the absence of plastic deformation, the grain size effect must vanish at the threshold of plastic strain. Such behavior is not supported by experimental observations. A third type of models assumes a composite behavior of polycrystals where the grain interior and a layer bounding GBs have different strength (Kocks, 1970). Plastic flow is initiated in the GBs region owing to the incompatibility in elastic deformation of adjacent grains (Benson, Fu, and Meyers, 2001; Meyers and Ashworth, 1982). In another approach, Li (Li, 1963) (see also (Bata and Pereloma, 2004)) suggested that grain size effects are induced by dislocation emission from GB ledges. More recently, Sinclair *et al.* (Sinclair, Poole, and Bréchet, 2006) proposed a new model accounting for dislocation storage at GBs and for their interaction with dislocations on the opposite side of the grain. The resulting elastic screening decreases the back stress, which in turn predicts a decrease of K with deformation.

A strong limitation of all existing models is that they do not provide a detailed description of dislocation arrangement and interactions in the vicinity of GBs. Numerical simulations are then needed to develop more physically justified models. Molecular dynamics are frequently used to analyze the GB response to one or few impinging dislocations (e.g. (Dewald and Curtin, 2007; Wang, Beyerlein, and Tomé, 2014)). But the collective dislocation properties responsible for the HP effect can only be investigated with larger scale simulations such as discrete Dislocation Dynamics (DD). Based on 2D-DD simulations, Biner and Morris (Morris and R, 2002) studied the evolution of the flow stress in polycrystals with one slip system per grain and grain size ranging from 2–16 μm. Lefebvre *et al.* (Lefebvre, Devincre, and Hoc, 2007) made simulations with grains in the range 0.5–2 μm size and two slip systems per grain. In both studies, the yield stress was found to vary as d^n, with an exponent n rather different from -1/2. 3D-DD simulations appear to be the only approach for quantitative investigations. Very few 3D-DD simulations of polycrystalline aggregate have been reported. Ohashi *et al.* (Ohashi, Kawamukai, and Zbib, 2007) studied the effect of grain size on the stress necessary to activate Frank-Read sources. Their results suggest that sources with lengths close to one third of the grain size are the first to be activated. This effect was accounted for by introducing an addition hardening term proportional to the inverse of the grain

size. On the other hand, the accumulation of GNDs at GBs was reproduced by Zhang *et al.* (Zhang et al., 2014) and connected to strain gradient in crystal plasticity. Only, De Sansal *et al.* (Sansal, Devincre, and Kubin, 2009) investigated the plasticity of a periodic polycrystalline aggregate made with regular polyhedral grains. The calculated yield stress in these simulations was found to vary with a HP exponent n between -1/2 and -1. In addition, this study underlined the absence of dislocation pileups and intensive cross-slip activity in the simulations with grain sizes lower than 1 μm. On the other hand, using 3D-DD simulations, El-Awady (El-Awady, 2015) has shown that, depending on the initial dislocation density, size effects may result from dislocation starvation, single-source strengthening or exhaustion hardening.

Remarkably, most published studies are concerned with the HP effects in polycrystals made of homogeneous equiaxed grains. Nevertheless, many materials of technological importance are composed of heterogeneous and non-equiaxed grains, such as bainitic and martensitic steels. Using the self-consistent scheme, Berbenni et al (Berbenni, Favier, and Berveiller, 2007) have shown that, not only the average grain size, but the type of the grain size distribution function and its standard deviation strongly affect the flow stress as well. The heterogeneity in grain size basically reduces the sensitivity to grain size. On the other hand, although grain shape is suspected to have strong effect on the flow stress (Van Houtte, 1982), little is known about the influence of grain shape on the HP Law (Delannay and Barnett, 2012; Hansen, Bronkhorst, and Ortiz, 2010). Using DD simulations, only Yellakara and Wang (Yellakara and Wang, 2014) investigated the response of polycrystalline thin films and reported a variation of the HP exponent with the simulated volume shape. In the latter study, only cubic and hexagonal shapes were investigated, with close aspect ratios.

Giving the above underlined difficulties in measuring, interpreting, simulating and predicting the grain size effects in polycrystals, it is necessary to split the problem into different issues: (i) the effect of grain size and shape on the flow stress of individual grains and small aggregates with impenetrable boundaries as a function of the loading direction, (ii) the effect of dislocation – GB interactions such as absorption, repulsion, transmission, etc. (ex. (Lee, Robertson, and Birnbaum, 1990; Shen, Wagoner, and Clark, 1988)) and (iii) the elasto-plastic interactions between adjacent grains (ex. (Raabe et al., 2003; Sachtleber, Zhao, and Raabe, 2002)). Clearly, the Hall-Petch effect cannot be correctly addressed without accounting for these three issues together. However, these features cannot be investigated by any individual simulation technique because they pertain to different scales. Feature (ii) involves the GB atomic structure and disorientation, while feature (iii) requires simulations at the macroscopic scale of a

representative volume element. In contrast, feature (i) is related to the collective dislocation behavior inside one grain, which is the scope of mesoscopic simulations such as dislocation dynamics. The complete investigation of the Hall-Petch effect is thus still beyond the reach of one numerical simulation method. Many simulations at the three relevant scales are still necessary to provide a comprehensive picture of grain size effect.

In this paper, we report on 3D-DD simulations at the mesoscopic scale, pertaining to feature (i). It must be noted that the assumption of impenetrable GBs used in the present study does not give a fully description of the dislocation-GB interactions. Such proposition is made for reason of simplicity and because the development of more realistic constitutive rules accounting for all the phenomena observed at GBs in experiments or in atomistic simulations does not exist today. The development of such rules goes far beyond the goal of the present study. Still, 2D and 3D-DD simulations, accounting for dislocation transmission at GBs, have been proposed with some success (Zhou and Lesar, 2012; Quek et al., 2014; Fan et al., 2015; Burbery et al., 2017) to model plastic strain hardening in ultrafine-grains polycrystalline aggregates. These studies are considering grain size smaller than 1.5 μm and therefore dislocation dynamics at very high stress. Contrarily, the present investigation considers grain sizes from 1.25 to 10 μm and small plastic strain up to 0.2% . Hence, the stress on the dislocation arrested at GBs is always relatively low. This is why, the assumption of impenetrable GBs is expected to be an appropriate solution to investigate the Hall-Petch effect. The objective is to shed light on the evolution of the flow stress of one grain and small periodic clusters of grains as a function of the grain/cluster size, shape and orientation. In particular the collective dislocation properties are explored and a simple method is proposed to account for the grain shape effect. The paper is organized as follows: simulation technique and conditions are given in Section 2.2; then DD calculations on the grain size effect (Section 2.3) and on the grain shape effects (Section 2.4) are presented. The obtained results are discussed in Section 2.5 and general conclusions are summarized in Section 4.4.

2.2 Simulation technique and conditions

The 3D-DD simulation code used in this study is *microMegas*. The basic features of this code are presented in reference (Devincre et al., 2011). In the following, only features important for the present simulations are specified. Pure copper is the model FCC material considered in the study. As illustrated in Figure 2.1, initial dislocation microstructures are built up from random distributions of dipolar loops with square shape inside the simulated volumes. Every loop is composed of two pairs of edge segments

Shear modulus G (GPa)	Poisson ratio	Burgers vector b (A°)	Lattice friction τ_f (MPa)	Schmid factor m_{001}	Schmid factor m_{111}	Schmid factor m_{135}
42	0.431	2.5525	2.5	0.408	0.272	0.49

TABLE 2.1: Main 3D-DD simulation parameters used to model Cu plastic strain

belonging to a given slip system s and two edge segments belonging to the collinear system of s, i.e. sharing the same Burgers vector in a different glide plane. Dipolar loop distribution is preferred here to a distribution of Frank-Read sources, because it avoids infinitely strong dislocation pinning points that come with the use of sources (Mohles, 2001) and favors the emergence of a realistic 3D dislocation networks. At the beginning of simulations, the initial dislocation configuration is relaxed to generate an energy-minimized microstructure where dislocation segments are free to form junctions or annihilate. This relaxed 3D interconnected microstructure is thus closer to the "real" microstructure of un-deformed crystals and avoid using a distribution of Frank-Read sources with arbitrary length. The faces bounding the simulated volume are perpendicular to the <100> axes of the FCC lattice. Tensile tests are usually simulated by imposing a constant uniaxial strain rate in three specific crystalline directions ([100], [111] and [135] directions) in order to investigate different slip dynamics in single and multi-slip conditions. Unless specified, all values of the yield stress $sigma_y$ are taken at 0.1% of plastic strain. The copper elastic constants, the Burgers vector and the Schmid factors calculated for the 3 tensile directions are listed in Table 2.1

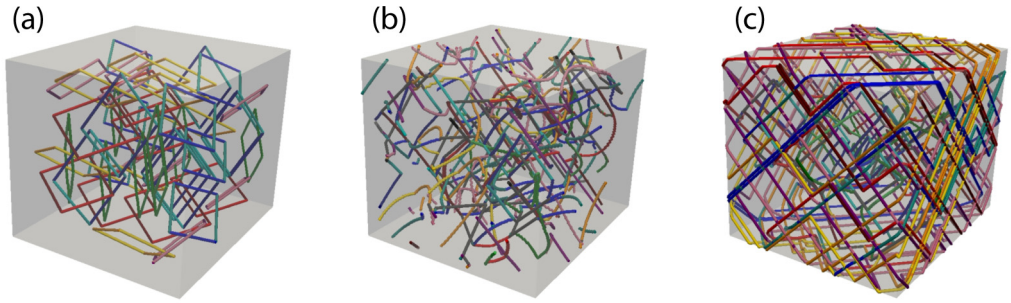

FIGURE 2.1: (a): example of an initial dislocation configuration with a random distribution of dipolar loops; each color corresponds to a specific slip system. (b) and (c) are the dislocation microstructures obtained after deformation using transparent boundaries (TBs) and impenetrable boundaries (IBs), respectively.

To make sure that simulations are close to quasi-static conditions, all computations are made at relatively low strain rate amplitude. It must be noted here that the strain

rate used in simulations must be decreased when increasing the grain size since a fixed dislocation displacement produces less plastic deformation. The strain rate solutions used with each grain size are given in Table 2.2. Tests have been made systematically to control that the simulation results are not modified when the simulated strain rate is decreased by a factor 2.

Screw dislocation segments are allowed to cross-slip following a framework described in (Raabe et al., 2003). As previously discussed in (Dewald and Curtin, 2007), cross-slip is a key mechanism in the simulation of polycrystals with grains in the micrometer range. This mechanism is needed to avoid rapid exhaustion of dislocation sources when artificial pinning points are not considered in the initial dislocation microstructure.

2.2.1 Boundary conditions

Periodic conditions (PC) are applied to the simulated volume in all calculations and two types of boundaries are used. With the *transparent boundary* (TB) condition, dislocations are free to cross the simulated volume borders and they automatically reinter the simulated volume from the opposite face due to the PC. Alternatively, the *impenetrable boundary* (IB) condition confines dislocation motion inside the grain. Dislocations inside these grains are then immobilized when they reach an IB. Hence, TB condition is used to investigate the properties of an infinite *single crystal* (or bulk crystal) and the IB condition is employed to simulate plastic slip in grains with non-penetrable boundaries.

In this study two sets of calculations that make use of IB condition are performed. The first geometry is made with *one grain* occupying the total simulated volume. This simulation condition reproduces a polycrystal made of one periodic grain, which is named as the "*one-grain*" polycrystal simulation. Comparison between the *one-grain* polycrystal simulations and *single crystal* simulations that make use of TBs is illustrated in Figure 2.1 In the *one-grain* simulations, by virtue of the PCs, dislocations accumulating against the IBs experience elastic interactions with dislocations accumulated on the other side of the IB. Obviously, this feature is a strong limitation of the *one-grain* simulations since in real polycrystals, dislocations on one side of a GB experience interactions with dislocation belonging to an adjacent grain with different orientation and therefore different slip activity.

In order to check the pertinence of the *one-grain* simulations, a second type of geometry with larger simulation volumes made of four grains is also considered (see Figure 2.2). In these "*four-grain* simulations" , adjacent grains are loaded along different

Cubic grain size dimension d (μm)	1.25	2.5	5	10
Dislocation loop size l (μm)	0.375	0.75	1.5	3
Dislocation density ρ_{ini} (10^{12} m^{-2})	30	7.7	2	0.48
Strain rate amplitude (s^{-1})	250	200	50	15
Average dislocation strength	0.33	0.38	0.42	0.45

TABLE 2.2: Simulation conditions and initial dislocation microstructure definition as function of grain size. The Taylor coefficient is calculated from the simulated stress-strain curves at yield.

axes and contain initially different distributions of dislocation loops. This results in different slip activity on both sides of the IBs.

2.2.2 Grain size and initial dislocation density

To ideally simulate the HP effect, the influence of grain size on the flow stress should be computed, keeping all other microstructure features (such as dislocation density) unchanged. It turns out that this requirement is hard to fulfill for the following reason. The initial dislocation density is given by $\rho = (n \times 4l)/d^3$, where n is the number of dislocation loops with a squared shape randomly inserted in a grain; l the dislocation loop size and d the grain size (see Figure 2.1a). As the grain size is increased by a factor of 10 in the simulations, considering initial loops size independent of the grain size imposes a variation up to a factor of 1000 in the dislocation number between simulations to keep the dislocation density unchanged. Hence, working at constant dislocation density leads to strong computational time issues as well as geometrical difficulties to set up a realistic 3D dislocation network whatever the grains size. Rather, it is simpler to fix an initial loops size proportional with the grain size and to keep their number n and distribution unchanged. This simpler solution, similar to the one previously used in micro-pillars simulations (see for instance (El-Awady, 2015)), allows for simulations at different grain size with a dislocation density variation smaller than a factor 100 in good agreement with experimental observations. This is why the dislocation density we used in the DD simulations varies with the grain size as reported in Table 2. In addition, as discussed by many authors (see for instance (El-Awady, 2015)), many experimental evidences show that it is unrealistic to expect that the dislocation density in the different grain sizes would be the same.

Since the interaction coefficient of the Taylor equation (see Section 2.3.1) varies with the initial dislocation density, the corresponding coefficient (usually called forest interaction strength or Taylor coefficient) is calculated from the simulations. The corresponding values are given in Table 2.2.

2.2.3 Simulated grain shapes

One of the main goals of this work is to quantitatively evaluate the impact of grain shape on the HP law. Hence, three different grain shapes are considered (see Figure 2.2). We consider cube, plate and needle grain shapes, to simulate the shapes frequently found in polycrystals. These shapes are close to those observed in recrystallized polycrystals with equiaxed grains, or lathes and needles observed during allotropic transformations (bainite, perlite and martensite, etc. (Bhadeshia and Honeycombe, 2006)) and thin film (Yoshinaga et al., 2008).

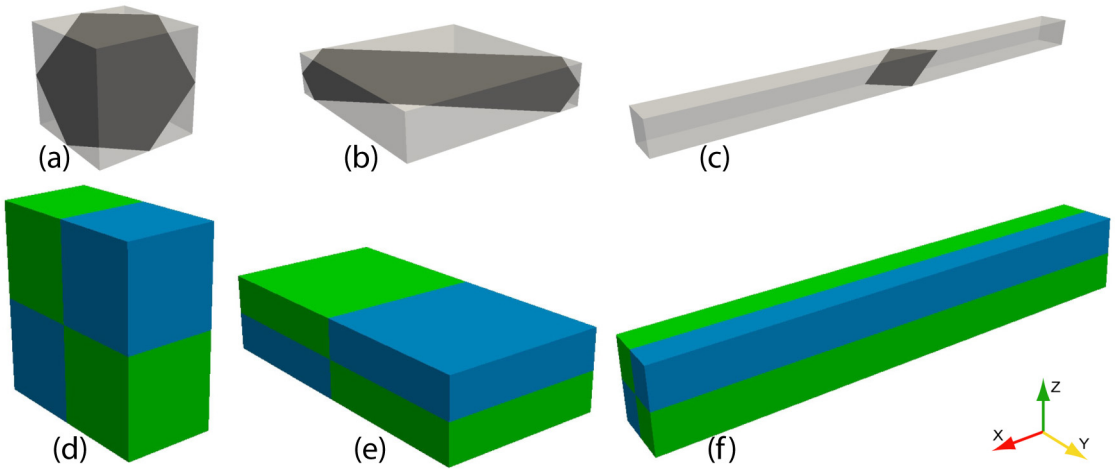

FIGURE 2.2: (a, b, c) the three grain shapes investigated with the simulations. One {111} FCC slip plane at the center of each grain is drawn to illustrate the variation of the slip plane area; (d, e, f) the three different types of four-grained simulated aggregates. Grains of the same color are mechanically loaded identically but contain different dislocation distributions.

The ratios between the linear dimensions of the three grain shapes are as follows: three almost equal dimensions (5;5;5) for the cube grain, two large dimensions (8;8;2) in the plate grain and one large dimension (31;2;2) in the needle grain. By convention, the grain size in all cases is defined as $d = \sqrt[3]{V}$.

2.3 The grain size effects

Given the limitation of DD calculations, it is clear that DD cannot entirely address the grain size effect observed in polycrystals. However, a formulation similar to that in Eq. 1 represents a useful framework for the analysis and interpretation of our results. In this context, the friction stress σ_0 in the HP law accounts for the *intragranular* yield stress, as suggested by Cordero *et al.* (Cordero, Knight, and Schuh, 2016). σ_0 is material dependent and this quantity must be defined to calculate the HP term. We suppose in the simulations that σ_0 is equal to the yield stress of an ideal Taylor polycrystal, i.e. a

polycrystal of random texture and very large grains. For such polycrystals, σ_0 is directly related to the Critical Resolved Shear Stress τ_c measured in a single crystal made with the same material. In addition, in the *one-grain* polycrystal simulations, σ_0 reduces to the yield stress of an infinitely large grain and the HP law becomes:

$$\sigma_y = \frac{\tau_c}{m} + Kd^n \tag{2.2}$$

with m is the highest Schmid factor of slip systems calculated in the simulated grain. Here, it must be noted that this is the main advantage of the *one-grain* simulations. Such simulations give the possibility to study the grain size effect at the slip system level and to reduce the HP law on the active slip systems to:

$$\tau_y = \tau_c + kd^n \tag{2.3}$$

where $\tau_y = m\sigma_y$, $\tau_c = m\sigma_0$ and $k = mK$ the reduced HP constant.

To test the validity of Eq. 2.2 or Eq. 2.3, the plastic behavior of a single crystal is first determined to calculate the value of τ_c in all simulations. In single crystals, τ_c is controlled by forest interactions and is expected to follow the Taylor equation:

$$\tau_c = \tau_f + \alpha Gb\sqrt{\rho} \tag{2.4}$$

where τ_f is a lattice friction (solid solution) accounting for dislocation interaction with impurities. In the present study, τ_f is fixed to the value of 2.5 MPa in the simulation to mimic common copper polycrystals with a low purity.

In the Taylor equation, the coefficient is the forest strength coefficient, which was directly calculated by DD simulations (Madec, Devincre, and Kubin, 2002). In the following, a simple procedure proposed by Devincre *et al.* (Devincre, Kubin, and Hoc, 2006) is used to account for the variation of α with the dislocation density ρ:

$$\alpha == \frac{\ln\left(\frac{1}{\alpha_{ref} b\sqrt{\rho_{ini}}}\right)}{\ln\left(\frac{1}{\alpha_{ref} b\sqrt{\rho_{ref}}}\right)}\alpha_{ref} \tag{2.5}$$

where α_{ref} is evaluated to 0.4 at $\rho_{ref} = 10^{12} m^{-2}$ in the case of a uniform distribution of slip systems.

Since the initial dislocation density increases with decreasing grain size (see Table 2.2), the friction stress σ_0 in the HP law is following Eq. 2.4 expected to increase with decreasing grain size. This variation in σ_0 cannot be neglected when calculating the HP term (Kd^n). This is why σ_0 must be assessed. In order to do so, simulations of

copper single crystals with increasing initial dislocation density are reported in the next section.

2.3.1 Assessment of the single crystal behavior

For each tested initial dislocation density (see Table 2.2), three different tensile axes were considered: [001], [111] and [135]. As explained in Section 2.2.1, single crystal simulations are made replacing in the *one-grain* simulations the impenetrable boundary (IB) condition by the transparent boundary (TB) condition.

As illustrated in Figure 2.3a, the resolved shear stress τ computed in the single crystal simulations does not evolve rapidly with the strain. Hence, strain hardening is low. To complete this general remark, it can be seen that the [111] orientation as a higher strain hardening rate than the [001] orientation while both are under multiple-slip condition. On the other hand, the orientation [135], leading to single slip condition, has non-visible strain hardening. The computed strain hardening rates are: $\theta_{001} \approx 170$MPa, $\theta_{111} \approx 320$MPa and $\theta_{135} \approx 0$. Such behavior is in good agreement with experiments where strain hardening is in the order of $G/200$ in multislip and $G/3000$ in single slip conditions (Devincre, Hoc, and Kubin, 2008). In these conditions, it is possible to evaluate without ambiguity τ_c in each simulation. The computed values are plotted as a function of the initial dislocation density in Figure 2.3b. As expected, all the simulation results are in good agreement with the predictions of the Taylor equation (Eq. 2.5), when the drift of the forest strength coefficient α associated to the variation of the dislocation line tension with the dislocation density ρ is considered.

Two additional observations can be made from Figure 2.3b: (i) τ_c is only slightly affected by the orientation of the tensile axis. Hence, the nature and number of active slip systems have little influence on the yield stress of single crystal. (ii) Predictions of Eq. 2.4 constitute a lower bound for the values of τ_c obtained in DD simulations. This is the signature of the effective stress needed to impose plastic strain by imposing a finite velocity of mobile dislocations, which necessarily causes a shift from the quasi-static critical stress prediction made with the Taylor equation. Nevertheless, the difference between the computed values and the model predictions never exceeds a few percent.

2.3.2 Impenetrable boundaries and plastic strain hardening

In a second step, comparison is made between the results of the *single crystal* and the *one-grain* polycrystal using the same simulation volumes and the same initial dislocation configurations. Going from one simulation to the other implies only to switch from TB

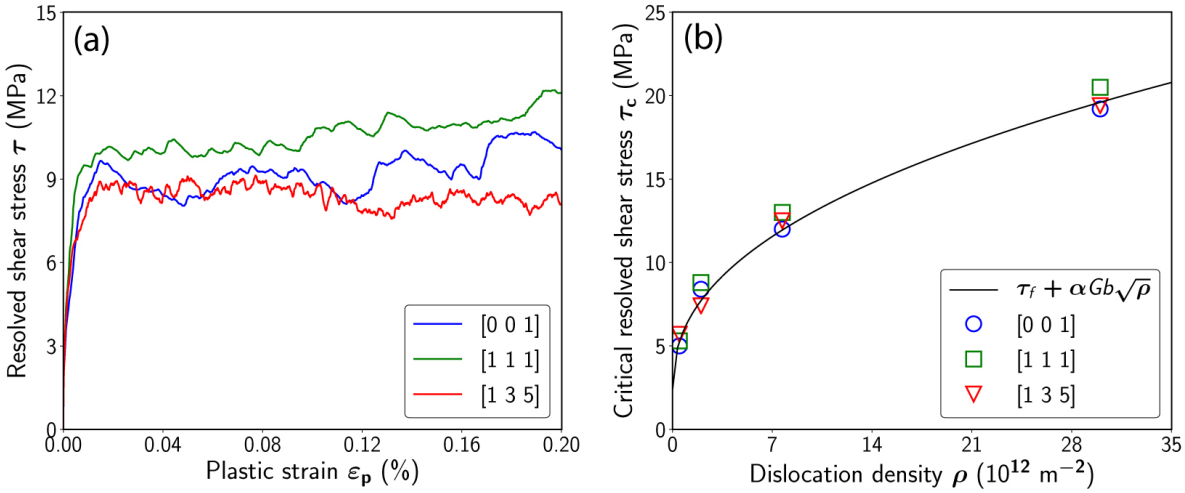

FIGURE 2.3: (a) Stress-strain curves of 3 single crystal simulations with 3 different crystal orientations. Computations are made using transparent boundaries of simulation volume of 5 μm size. (b) Evolution of the CRSS as a function of the initial dislocation density (see Table 2.2). The full line is the prediction of the Taylor equation (Eq. 2.4).

to IB condition. In Figure 2.4 we show an example of the evolution of the applied stress (a) and the dislocation density (b) as a function of the plastic strain in a cubic volume of 5 μm loaded in the [001] orientation. One can easily see that the flow stress and the dislocation density increase with strain much faster in the *one-grain* simulation than in the *single crystal* simulations. This is a direct outcome of IB condition and a signature of the size effect. The large dislocation storage rate observed in the *one-grain* simulation is a consequence of dislocation accumulation at the GBs.

Strain hardening calculated in the *one-grain* simulation is almost constant and amounts to approximately 13 GPa in Figure 4, which corresponds to approximately $G/3$. This hardening rate is 100 times larger than that found in the *single crystal* simulation. It is computed up to a plastic strain of 0.2% , i.e. the conventional elastic limit considered for the determination of yield stress in most experiments. As revealed in Figure 2.4a, the huge hardening rate we found in the *one-grain* simulation takes place from the very beginning of the plastic deformation and cannot be justified by an increase of forest hardening induced by the increase of the dislocation storage rate (see § Discussion in Section 2.5).

2.3.3 Hall-Petch effects in the one-grain simulations

Now, we investigate the effect of the grain size on the yield stress using the *one-grain* simulations. Variations of the grain size are tested from 1.25 μm to 10 μm (see Table 2.2). In this section, the grains are cubic and tensile tests are made in different

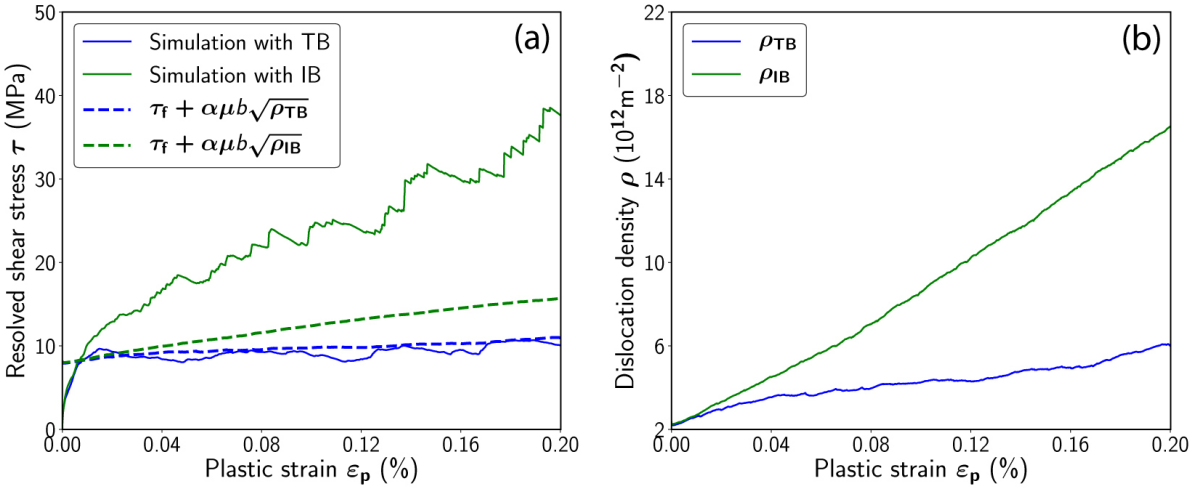

FIGURE 2.4: Comparison between simulations using transparent boundaries (TBs) and impenetrable boundaries (IBs) in a 5 μm cubic simulation volume loaded in the [001] tensile axis: (a) stress-strain curves and (b) dislocation density as a function of plastic strain. Dashed lines in (a) correspond to the prediction of Eq. 2.4 with the dislocation density recorded in (b).

orientations: [001], [111] and [135]. Examples of stress-strain curves computed for the *one-grain* simulations deformed in the [135] direction are shown in Figure 2.5a. Results of these simulations are compared with the single crystal behavior obtained with the same dislocation configuration, i.e. an initial dislocation density of $2.10^{12}m^{-2}$. One sees that the flow stress increases substantially with decreasing grain size. Again, it must be emphasized that this strengthening cannot be explained by the modification of initial dislocation density with the grain size. Moreover, when comparing the different curves in Figure 2.5a, it appears that strain hardening is weakly sensitive to grain size in those simulations.

In order to investigate the grain size effect using Eq. 2.3, the critical stress τ_c computed from the single crystal simulation is subtracted from the resolved yield stress τ_y recorded in the *one-grain* simulations. Results of those calculations are plotted as a function of grain size d in Figure 2.5b for the twelve simulations we performed. Simulation results systematically exhibit linear dependency on the inverse of the square root of the grain size. In addition, in the case of the *one-grain* simulations oriented for single slip deformation, the grain size effect is tested at two plastic strain amplitude (0.1% and 0.2%). From this last set of simulation results, it is clear that the slope of the linear fit increases with the selected plastic strain offset.

Hence, the HP constant K given by the slope of the linear fit (see dashed lines in Figure 2.5b) varies with the loading axis and selected offset of the yield stress. Such variation is not a discrepancy of the simulations, but the consequence of the *one-grain*

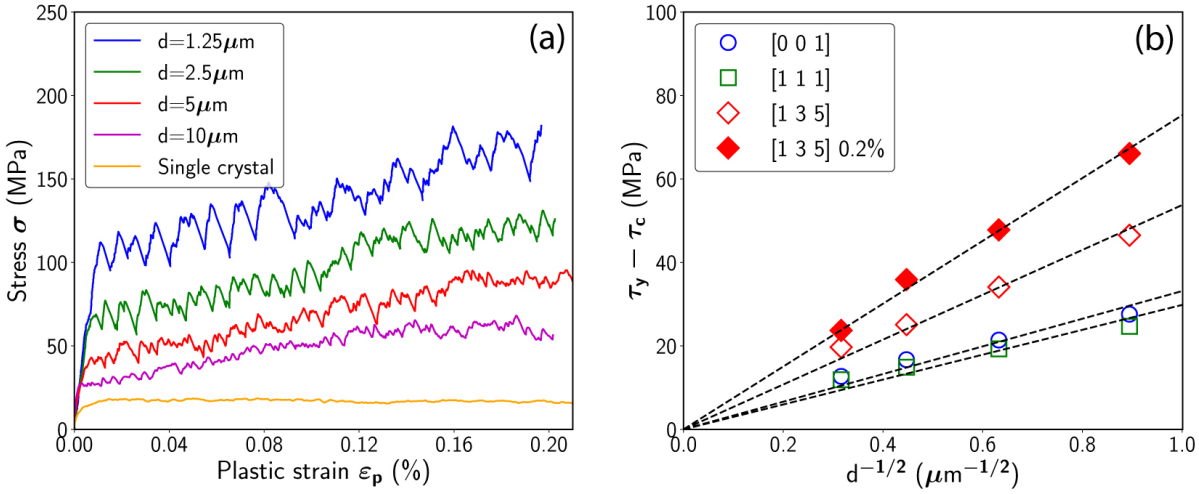

FIGURE 2.5: (a) Example of stress-strain curves obtained with the one-grain simulations for tensile tests along the [135] axis and for different grain sizes. The stress-strain curve simulated with TBs is added for comparison; (b) evolution of the HP term calculated at plastic strain equal to 0.1% and with the grain size of different orientations (full diamonds correspond to solutions obtained with 0.2% offset of plastic strain).

simulation condition. We will see in the discussions section that a realistic value of K can be defined as an average of those obtained from the *one-grain* simulations with different plastic strain amplitudes and different grain orientations.

2.4 Results on the grain shape effects

2.4.1 The one-grain simulation

The same set of simulations described in the previous section was repeated with grains of plate and needle shapes. The increase in the critical stress as a function of the grain size for the three tensile directions is depicted in Figure 2.6. For the sake of clarity, simulation results are split into three figures depending on the loading axis.

As can be seen, the HP term, i.e. the term $(\tau_y - \tau_0)$, is always approximately proportional to $1/\sqrt{d}$. The HP law seems to be still valid in the case of non-equiaxed grains. However, the slope of the curves, i.e. the HP constant K, depends strongly on the grain shape. For the three investigated shapes, K has the largest value in the case of needles and weakest for cubic grains. On the other hand, the HP constant is higher in the single slip condition ([135] orientation), while it remains substantially the same in multislip conditions ([001] and [111] axes).

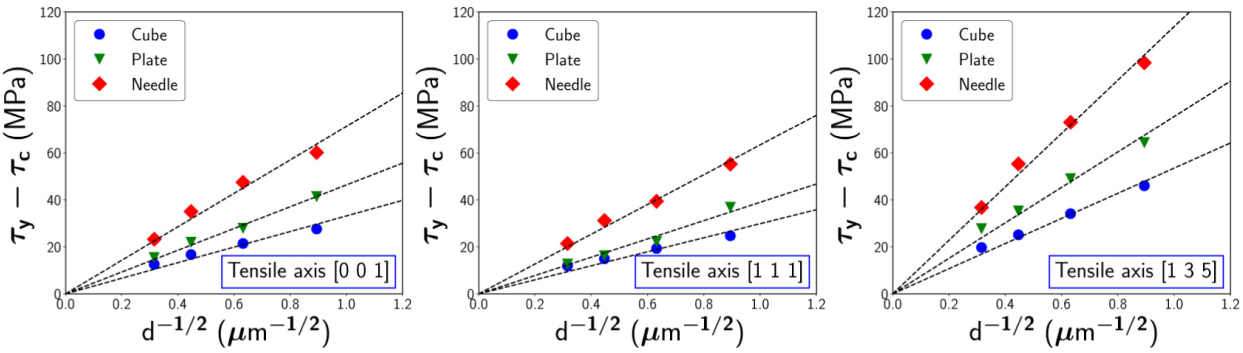

FIGURE 2.6: Variation of the HP term as function of the grain size for the three simulated grain shapes and loading axis.

2.4.2 Four-grain simulations

In the previously reported simulations, the HP effect is investigated with particular aggregates made of one grain surrounded by its periodic images. We can suspect this configuration to induce artifacts due to the equal slip activity on both sides of the GBs. To investigate the effect of plastic strain incompatibility at GBs, the behavior of *four-grain* aggregates (described in Section 2.2) is now investigated. For the sake of simplicity, these simulations are performed at imposed stress rate (stress-controlled mode). As the previous simulations have been made at constant strain rate (strain controlled mode), we first check the consistency between the two controlling modes in the simulation. In Figure 7a, the results of *one-grain* simulations with a 2.5 μm cubic grain deformed along the [001] and the [111] axis are shown as a function of loading modes. From such tests, we see that the two controlling modes give basically the same mechanical response and both controlling modes can be used indiscriminately in the aggregate simulations.

In addition, in Figure 2.7a two stress-strain curves taken from simulations of *four-grain* aggregate with grains alternatively oriented in [001] and [111] and different in their random initial dislocation distribution are presented. Again, it can be seen that both stress-strain curves are very close to each other. This ensures that the initial dislocation microstructure has little influence on the simulation results.

Furthermore, it can be noted in Figure 2.7a that the *four-grain* aggregate stress-strain curves are close to the average of the stress-strain curves (black dashed line) of the *one-grain* simulations of the [111] and [001] orientations.

Results relative to the evolution of the HP term calculated with the *four-grain* simulations as a function of grain size and for different grain shapes (cube, plate and needle) are reported in Figure 2.7b. In this figure, we see that the linear dependency of the HP

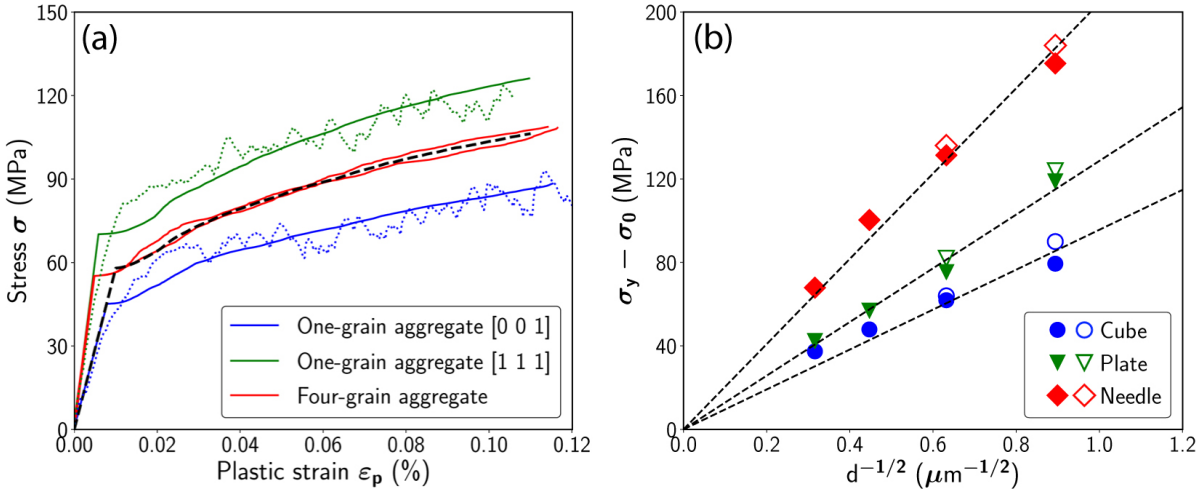

FIGURE 2.7: (a) Comparison between stress-controlled (full lines) and strain-controlled (dotted lines) modes for the one-grain simulations. The cubic grain is 2.5 μ m size and two loading axes ([100] and [111]) are considered. For comparison, two stress-strain curves calculated with the four-grain simulations using the same grain shape, same size and two loading orientations are reproduced in red curves. The two reported four-grain simulations only differ in the initial dislocation distributions. The black dashed line is the average of the one-grain simulations; (b) evolution of the HP term calculated with the four-grain simulations (open symbols) and calculated as an average of the one-grain simulations made with the [100] and [111] loading axis (full symbols).

term on the inverse of the square root of the grain size applies in all cases. Also, the values of the HP constant K (slope of the straight lines in Figure 2.7b) vary substantially with the grain shapes. The largest value of K is obtained with the needle shapes and the lowest for the cubic grains.

2.4.3 The Bauschinger effect

Since most of the dislocation content in the grains are accumulated at grain boundaries, it is interesting to investigate a possible Bauschinger effect in our simulation conditions. To do so, a specific simulation is performed on the 5 μm grain using the impenetrable boundary condition. The tensile axis is [135] and the loading is reversed at 0.3% of plastic slip. The corresponding stress-strain curve is given in Figure 2.8.

As can be noticed on the curve, the strain reversion leads first to a vertical drop of the stress with respect to the plastic strain axis. This elastic unload step is followed by approximately 0.1% of plastic strain reversal. This plastic strain relaxation reveals that one third of the dislocation microstructure accumulated at the grain boundary is pushed back when unloading. In addition, plastic strain in the compression direction is

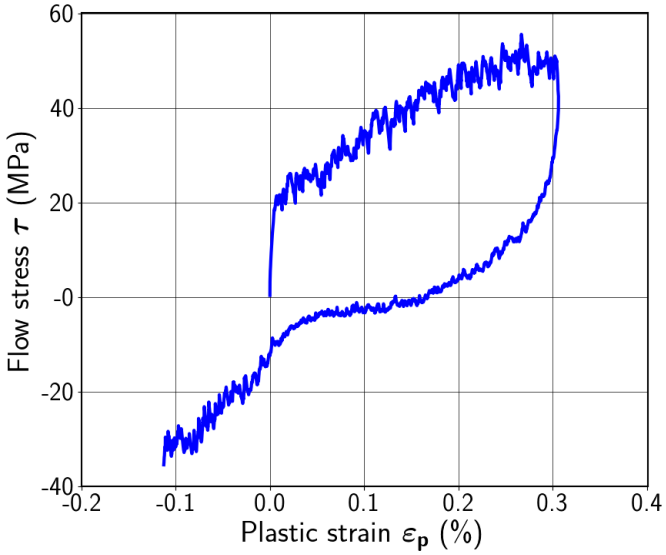

FIGURE 2.8: Stress strain curve associated to the Bauschinger test made for the 5 μm grain size simulation and the loading axis [135].

observed at stress amplitude smaller than -5MPa. The Bauschinger effect we calculate is thus very strong and indicates the presence of a strong back-stress with an amplitude close to the flow stress. This test clearly shows that kinematic hardening is predominant with respect to the isotropic hardening in our simulations.

2.5 Discussion

According to the usual interpretation of the HP effects (Armstrong et al., 1962; Cordero, Knight, and Schuh, 2016), the yield stress of polycrystals is composed of two linearly superposed contributions: the intragranular one, represented by the friction stress σ_0 and the intergranular component represented by the HP term (Kd^n). The main objective of this work is to investigate the evolution of the HP term as a function of the grain size and shape when assuming that GBs are impenetrable barriers to dislocation motion (i.e. in the relatively low stress and low strain conditions). To do so, the HP term must be isolated from the friction stress σ_0 in the simulated flow stress. In the periodic aggregates models we investigated (*one-grain* and *four-grain* simulations), $\sigma_0$is by definition the flow stress of the same aggregates, but with very large grain size. Because of DD simulation limitations, it is not possible to compute directly σ_0. This is why the friction stress of each simulation condition must be evaluated. In the case of the *one-grain* simulations, σ_0 becomes the yield stress of a large single crystal oriented in the same direction as the grain in the simulation. The results reported in Figure 2.4 prove that σ_0 can be precisely evaluated by the Taylor equation (Eq. 2.4) provided that the variation of the

forest strength with the initial dislocation density is taken into account. In the *four-grain* simulations, the results reported in Figure 2.7 show that σ_0 can be considered as the average of the Taylor equation predictions of the critical stress of all grain orientations present in the aggregate.

2.5.1 Size effects in equiaxed grains

In all simulations performed in this work, we calculated the HP term and examined the dependency on d, as given in Eq. 2.2. Our results show good alignment with d^n when $-0.7 < n < 0.3$. This is in partial agreement with the statistical analysis made by (Dunstan and Bushby, 2014) which shows that there is no conclusive experimental evidence of the linearity with $n = -0.5$ dependency. However, when we impose that the fitting lines pass by the origin, only values of $-0.5 < n < -0.4$ provide good fit to our results. This is why, we consider in this discussion the exponent to be equal to -0.5. The good alignment with $1/sqrtd$ is evidenced, in Figure 2.5 and Figure 2.6 for the *one-grain* simulations and in Figure 2.7 for the *four-grain* simulations. This choice is consistent with the initial HP relation (Hall, 1951) and many experimental investigations (Armstrong et al., 1962; Cordero, Knight, and Schuh, 2016; Li, Bushby, and Dunstan, 2016).

Since dislocation storage strongly increases when grain size decreases, it is interesting to check whether the obtained size effects can be explained by an isotropic hardening resulting from the increase in dislocation density. To this end, we first calculate the forest strengthening as a function of the recorded dislocation density. Dislocation density increases basically only on active slip systems. Therefore, the use of the Taylor equation with an average forest strength α is not justified at finite strain. Instead, the tensor form of the Taylor equation accounting for dislocation density on each slip system proposed by Franciosi *et al.* (Franciosi, Berveiller, and Zaoui, 1980) is preferable:

$$\tau^s = \tau_f + \mu b \sqrt{\sum_{i=1}^{12} a^{si} \rho^i} \tag{2.6}$$

In Eq. 2.6, a^{si} is the interaction matrix known from previous DD simulations investigations (Hansen, Bronkhorst, and Ortiz, 2010), accounting for the interaction strength between slip system i and s. Since dislocation density evolution on every slip system is recorded in the simulations, Eq. 2.6 gives a precise evaluation of the flow stress all along the stress strain curves. This is done in Figure 2.4a, where predictions of Eq. 2.6 are plotted in dashed lines for a single crystal simulation (transparent boundaries) and for the equivalent *one-grain* simulations (impenetrable boundaries). It can be seen that Eq. 2.6 correctly predict the flow stress of the single crystal simulation but not that

of the aggregate simulation, where the predicted shear stress is far below the recorded flow stress. Indeed, in the presence of IBs a large number of dislocations (with the same Burgers vector and direction) is accumulated close to the boundaries. This phenomenon of polarized dislocation structure at GBs leads to a strong intergranular strengthening that cannot be predicted by the Taylor equation, used to calculate forest strengthening.

Another feature of interest is the effect of grain size on the evolution of the dislocation density storage. It is interesting to compare the dislocation storage computed within the DD simulations with a simple geometrical analysis. Neglecting forest interactions, every dislocation loop accommodates in cubic grains a shear increment $\mathrm{d}\gamma \simeq bd^2/V$, and contributes to an increase in dislocation density $\mathrm{d}\rho \simeq 4d/V$. The rate of dislocation storage is thus $\mathrm{d}\rho/\mathrm{d}\gamma \simeq 4/bd$.

This prediction is compared with simulation results in Figure 2.9, gathering the results of all the *one-grain* simulations with grains of cubic shape and different sizes and orientations. It can be seen that the storage rate recorded in DD simulations is inversely proportional to the grain size. Furthermore, the above geometrical prediction is in good agreement with DD results, which confirm that almost all stored dislocations are accumulating at the IBs. In other terms, we checked that, in the present simulation conditions, dislocation storage in the bulk of the grains is almost negligible with respect to that at GBs. The forest dislocation storage term $(\alpha\sqrt{\rho}/b)$ frequently used in the literature when modeling the HP effect is not justified. These results are in full agreement with the classical Kocks-Mecking formulation of crystal plasticity simulations of polycrystal behavior by (Haouala, Segurado, and LLorca, 2018).

Although the storage rate is proportional to the grain size, it has been shown in Section 2.3.3 that work hardening is little sensitive to grain size. This discrepancy is only apparent, because stored dislocations are immobilized at grain boundaries as GNDs. With increasing deformation, dislocations of opposite sign are stored on the other side of the boundaries. These two GND groups screen increasingly their distortion field, which leads to the saturation of their effect on the flow stress. On the other hand, the Taylor term involves only SSD density (bulk dislocations), which was found to be almost independent of the grain size.

2.5.2 Estimation of the HP constant K

As discussed before, the HP exponent n is found close to -0.5 in all simulations. Therefore, the square root dependency is adopted in the following discussion. By subtracting the flow stress of large single crystal σ_0 estimated with Eq. 2.6, it is possible to calculate

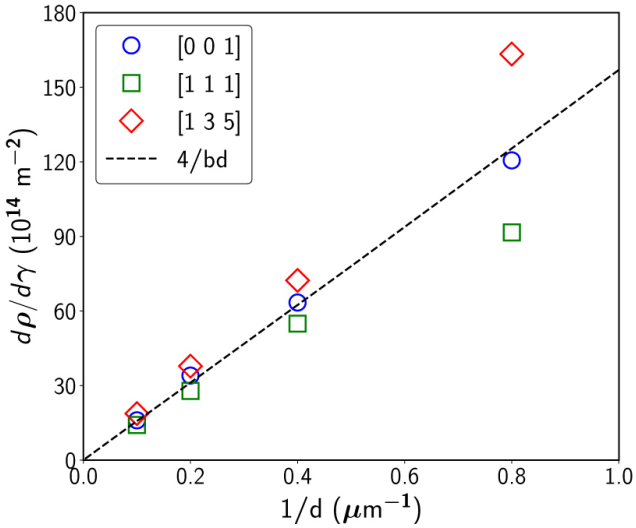

FIGURE 2.9: Rate of dislocation storage as a function of grain size. The dashed line represents the geometrical prediction proposed in this work.

the HP constant K as a function of grain size and shape. For the *one-grain* simulations of cubic shape, the computed values of K (in MPa$\sqrt{m}$) is found to vary with respect to the tensile axis: 0.1 for the [135] axis, 0.06 for the [111] axis and 0.07 for the [001] axis. This variation is expected because the arrangement of dislocations accumulated at the IBs depends on the number of active slip systems.

As discussed in the introduction, the evolution of the flow stress of one grain or small grain clusters as a function of the grain size and shape is only one feature of the grain size effects in real polycrystals. Therefore, it is useful to compare the value of K calculated in the simulations with experimental observations. To do so, one must bear in mind that the experimental values are usually obtained on polycrystals with many grain orientations, while we have only one grain orientation in the *one-grain* periodic simulation. Using the Taylor hypothesis, which has been confirmed in copper (Kocks, Tomé, and Wenk, 2000), the macroscopic stress becomes the average of the loading stress of the different constituent grains. Considering that the three simulated orientations are representative of common polycrystal texture, the HP constant measured in experiment can be compared with the average of the K values obtained in the simulations. The simple average of our results is $K = 0.092$ MPa $\sqrt{m}$, which is below the values reported in the literature (in MPa $\sqrt{m}$): 0.14 (Thompson, Baskes, and Flanagan, 1973), 0.19 (Meyers, Andrade, and Chokshi, 1995), 0.11 (Feltham and Meakin, 1957), 0.15 (Thompson and Backofen, 1971), 0.16 (Hansen and Ralph, 1982)(Hansen and Ralph, 1982). The latter values yield an average experimental value $K = 0.15$ MPa$\sqrt{m}$, which is 39% larger than that estimated with the simulations.

Additional thinking suggests that the difference observed between simulations and experiments may be due to the selection of the 0.1% strain offset for the definition of yield in the simulations, while it is 0.2% strain in the experimental investigations. The 0.1% offset was considered in order to reduce the significant computation times. Examining the stress-strain curves of the *one-grain* simulations (see for example Figure 2.5a), it is clear that the flow stress increases strongly and monotonously with the strain. The value of K must thus increase when fixing the offset of yield strain at 0.2% in the simulation. Only four simulations with grains oriented parallel to the [135] tensile axis was conducted to 0.2% of plastic strain. The HP terms calculated for these simulations are reported in Figure 2.5b (full diamond marks). The corresponding HP constant K is 0.16 MPa$\sqrt{m}$, which better matches with the experimental values. It is worth noting that the presence of solute element in the grain boundary layer increases the stability of grains, which is known to raise the value of K in industrial Cu alloys compared to pure Cu (see for ex. (Thompson, Baskes, and Flanagan, 1973). This finding has recently been confirmed in atomistic simulations of the Cu-Al systems by (Borovikov, Mendelev, and King, 2017).

2.5.3 Effect of grain shape

As revealed in Figure 2.6, for all grain orientations the HP constant K increases strongly when the grain shape considered in simulation is not cubic. The largest value of K is found with the needle shape, with a value two times larger than that obtained for cubic grains. This indicates that the HP effect increases when the aspect ratio of the grain is different from 1. We propose the following model to account for this property.

Let us consider grains in the form of parallelepipeds with three independent dimensions. As the accumulation of polarized dislocations close to IBs and its associated back stress is at the heart of the interpretations of the HP effect, we consider a dislocation loop expanding on a slip plane from the center of the grain. Its final length C is equal to the circumference of the surface of the slip plan bounded by the grain faces. During expansion, the accommodated plastic deformation is proportional to the area S of this surface. If the back stress is mainly associated with the polarized dislocation accumulated against IBs, it must be proportional to C. On the other hand, during deformation, the back stress increase with deformation is likely to be inversely proportional to S. Consequently, we expect K to be proportional to C/S. This factor has dimensionality [m^{-1}] and has to be normalized by the corresponding factor of a cubic grain shape to recover a factor of unity in the case of equiaxed grains. One can thus define a shape factor as:

$$\psi = \frac{C}{S}\frac{S_{cube}}{C_{cube}} \tag{2.7}$$

When considering FCC slip system symmetry and parallelepipedic grains with boundaries perpendicular to <100> directions, this shape factor takes the value $\psi = 1$ (cube), $\psi = 1.51$ (plate) and $\psi = 2.52$ (needle). The HP terms deduced from Figure 2.6 are plotted in Figure 2.10 as a function of $1/\sqrt{d}$ weighted by the shape factor. It can be seen that all data now collapse on the same straight line going through zero at very large grains. This confirms that the effect of grain shape revealed in the simulations is well taken into account using the shape factor defined in Eq. 2.7.

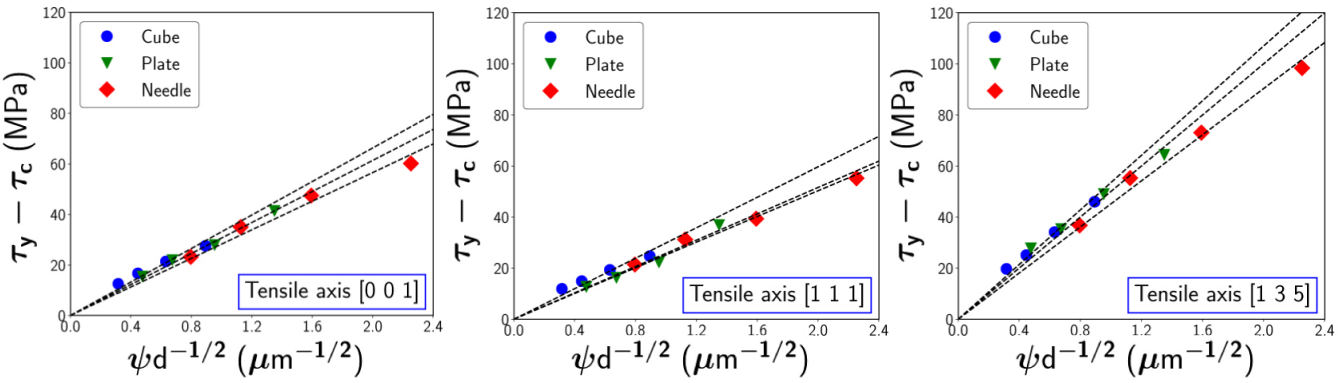

FIGURE 2.10: Evolution of the HP term with the grain size multiplied by the shape factor ψ for the three tested grain orientations and three grain shapes.

In other words, our simulations suggest that in order to apply the HP relation in the case of non-isotropic grain shapes of a volume V, one should define an effective grain size d_{eff} accounting for the shape factor given in Eq. 2.7. The present model is based on the calculation of the average dislocation loop length C and the average area swept by dislocations S, suggesting the following generalized Hall-Petch relation:

$$\sigma_y = \sigma_0 + \frac{K}{\sqrt{d_{eff}}} \qquad \text{with} \qquad d_{eff} = \frac{4S^2}{C} \times \frac{1}{\sqrt[3]{V}} \tag{2.8}$$

Eq. 2.8 involves three independent parameters because it is developed for parallelepipedic grains of three independent dimensions. Of course, for the geometries used in our simulations (needles and plates), Eq. 2.8 reduces to only two independent parameters.

2.5.4 Plastic strain incompatibility in the four-grain simulations

As shown in Figure 2.7, the stress-strain curve of *four-grain* simulations including [001] and [111] grains is close to the average of the stress-strain curves calculated with the

one-grain simulations for the [001] and [111] grain orientations. This result is surprising, since every grain is surrounded by grains of different slip activity in the *four-grain* simulations, while slip activity is identical on both sides of the boundaries in the *one-grain* simulations. The long range stress field associated with the polarized dislocation density accumulated at IBs is then expected to be different. Thus, in the case of periodic cluster simulations, it seems that the flow stress is little sensitive to the details of the grain neighborhood; the overall behavior is a simple average of the individual responses of its grains. This result supports the assumption made in homogenization methods (Roters et al., 2010) and XRD observations made on grain rotations in polycrystals deformation (Poulsen et al., 2003; Winther et al., 2004), at least, at the beginning of plastic deformation.

Consequently, it is relevant to check if the shape factor defined in the previous section still applies to the *four-grain* simulations with non-cubic grains (see results in Figure 2.7b). The corresponding HP analysis as a function of the effective grain size d_{eff} is plotted in Figure 2.11 in which d_{eff} was normalized by the norm of the Burgers vector b.

It can be seen that results of the *four-grain* simulations with different grain shapes (cube, plate and needles) are again aligned on the same line passing roughly by the origin. The corresponding HP constant K is equal to 0.087 MPa$\sqrt{m}$, which is quite close to the average of the values obtained for the [001] and [111] *one-grain* simulations (given in full symbols in Figure 2.11). In addition, this value is lower than that obtained from averaging the K values we obtained in Section 2.5.2 when accounting for all the *one-grain* simulations. This discrepancy comes from the absence of grains oriented for single slip condition (e.g. <135> orientation) in the *four-grain* simulations. Indeed, we show in Figure 2.6 that these grains induce the largest HP effect. Hence, our simulations show that polycrystal aggregates with texture endorsing single slip deformation in the grains are expected to provide enhanced HP effect at the yield strain.

Following the analyses made by Li *et al.*(Li, Bushby, and Dunstan, 2016), where it has been shown that experimental results fit well on different functions : $1/\sqrt{d_{eff}}$, $1/d_{eff}$ and $\ln d_{eff}/d_{eff}$, it is important to check if this feature applies also on our results. In Figure 2.11c and d, we plot the values of the HP term given in Figure 2.11a as a function of $1/d_{eff}$ and $\ln d_{eff}/d_{eff}$, respectively. Also, as sometime proposed in the literature, we plot in Figure 2.11b calculated values of the HP term as a function of d_{min}, the smallest edge length of grains. It can be noticed that any of these tests gives data aligned on a straight line passing by the origin. The trends observed in Figure 2.11c and d cut the y-axis at a significantly high value ($\simeq$ 30 MPa). This feature cannot be easily rationalized using physical arguments. Consequently, the best rationalization

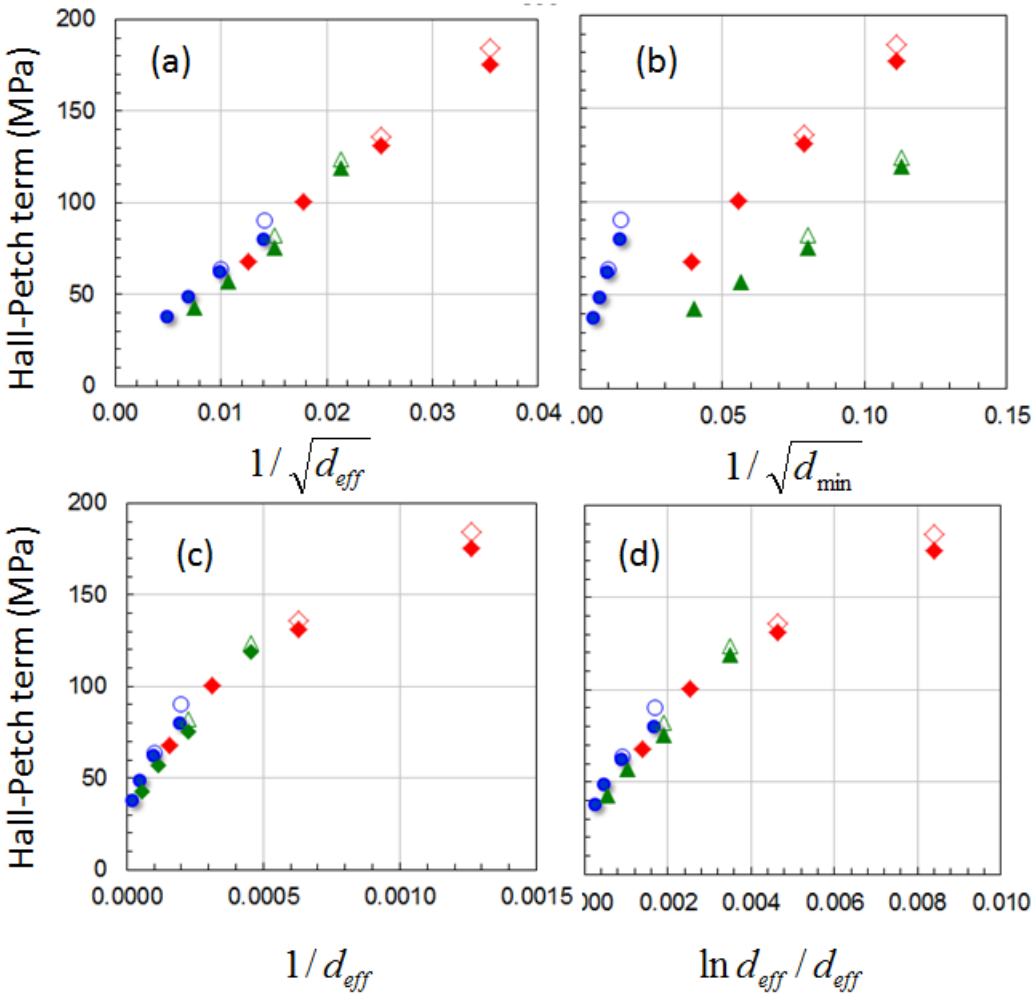

FIGURE 2.11: HP term vs different functions of the effective grain size d_{eff} and the smallest edge length of grain d_{min}, for simulations of grains of cubic (circles), plate (triangles) and needle (diamonds) shapes in one-grain (full symbols) and *four-grain* clusters (open symbols) with [001] and [111] orientations.

of our results seems to be given using the inverse of the square root of the effective grain size.

2.6 Conclusion

In this paper, we investigated the flow stress of periodic grains and 4-grain clusters of different sizes and shapes with impenetrable boundaries. The following conclusions can be drawn from the DD simulations reported in this paper:

– The critical resolved shear stress of single crystals is correctly predicted by the forest model given by the Taylor equation providing that the logarithmic dependency on the dislocations density of the forest strength (α) is appropriately accounted for.

- Strengthening induced by dislocations accumulated at GBs cannot by predicted using the Taylor equation. An alternative constitutive equation will be proposed in a forthcoming paper.

- The yield stress at 0.1% and 0.2% offset of plastic strain in grains of orientations <100>, <111> and <135> and shapes cube, plate and needle, is found to vary almost linearly with the inverse of the square root of the grain size.

- The grain size effect on the flow stress varies strongly with the grain orientation. The average of the HP constant values (K) calculated at 0.2% offset of plastic strain is close to the values reported in experiments on copper polycrystals. This suggests that the strong assumption we made when considering GBs as impenetrable captures the basic mechanical features that take place at low plastic strain and low stress.

- The HP constant varies strongly with the grain shape. A shape factor is proposed to account for this sensitivity and an effective grain size is defined in order to keep using the HP relation in the case of non-equiaxed grains.

- The mechanical response of periodic four-grain aggregates is well approximated by the average of responses of its constituent periodic grains.

Modeling the grain boundary interactions with moving dislocations (absorption, repulsion, emission) requires specific physically based constitutive rules for the boundary response. Such rules can only be addressed in atomistic simulations, where the atomic structures and thermodynamics of the boundaries are fully accounted for. On the other side, only DD simulation gives the possibility to reproduce the kinematic conditions associated to realistic dislocation patterns accumulated in the vicinity of grain boundaries. This information is essential to investigate the long-range internal stresses and stress concentrations affecting plastic deformation of polycrystals. Multiscale modeling of the inter- and intragranular features of plastic deformation of polycrystals is an exciting perspective that remains to be explored.

Chapter 3

The prediction of back stress with a surface GNDs based model

In the last chapter, polycrystalline aggregates made of grains with different sizes and shapes were tested with tensile loading by DD simulations (Jiang, Devincre, and Monnet, 2019). Although in this study, simple microstructure morphology was computed, a size effect could be identified and the Hall-Petch relationship is found to apply on the simulation results. One of the interesting features is that dislocation storage rate $\mathrm{d}\rho/\mathrm{d}\gamma$ recorded in the DD simulations is proportional to the inverse of grain size $1/d$, as predicted early by Ashby (Ashby, 1970). This prediction is consistent with simple geometrical arguments, assuming dislocation loops to depose at Grain Boundaries (GBs) of cubic grains. This comparison evidences that dislocation density in the bulk of grains is hardly increased during the deformation and that dislocation storage occurs mostly at GBs. These results are in full agreement with the Kocks-Mecking type crystal plasticity simulations of polycrystal made for instance by Haouala *et al.* (Haouala, Segurado, and LLorca, 2018). As known from Ashby's work since 1970 (Ashby, 1970), the dislocations accumulated at GBs are highly polarized. By definition, this type of polarized dislocations is named as Geometrically Necessary Dislocations (GNDs), leading to long-range internal stress that might be at the origin of size effect. This is the main issue to be investigated in this chapter.

When an external loading is applied to a polycrystal, plastic slip starts in well-oriented grains. Before deformation propagation, these well-oriented grains can be considered as embedded in an elastic medium, represented by the surrounding grains. When elastic anisotropy is neglected, this medium can be considered as a homogeneous medium characterized by its isotropic elastic constants.

In this chapter, we first describe a theoretical model we used to predict the stress associated with dislocation walls. Then we present DD simulations of tensile deformation of cubic grains embedded in an elastic matrix. These simulations are used to address the

formation of dislocation microstructure and determine the back stress, induced by the GNDs accumulated at the GBs. Finally, we present a GNDs–based model for the prediction of back stress inside polycrystalline aggregates and compare the model predictions with the solutions computed with DD simulations.

3.1 Theoretical background

3.1.1 Solution by Field Dislocation Mechanics

While the dislocation density tensor characterizes the polarized dislocation content in an elementary volume (Nye, 1953), the accumulation of dislocation at GBs or interfaces is better characterized by a surface singularity. This can be achieved using the concept of surface dislocation density tensor (Bullough and Bilby, 1956; Mura, 1987) as follows. We present here the calculation of stress field related to surface dislocation density tensor with the Field Dislocation Mechanics (FDM) theory developed by Acharya (Acharya, 2001).

In the framework of continuum description of plasticity, the transformation tensor $\underset{\sim}{\boldsymbol{F}}$ is a compatible field derived from the displacement vector $\underset{\sim}{\boldsymbol{u}}$:

$$curl\underset{\sim}{\boldsymbol{F}} = curl(\underset{\sim}{\boldsymbol{I}} + \nabla\underset{\sim}{\boldsymbol{u}}) = 0 \tag{3.1}$$

The elastic and plastic deformation tensors are generally incompatible fields. Following the well-known multiplicative decomposition, one may write:

$$\underset{\sim}{\boldsymbol{F}} = \underset{\sim}{\boldsymbol{F}_e}\underset{\sim}{\boldsymbol{F}_p} \quad \text{and} \quad curl\underset{\sim}{\boldsymbol{F}_e} \neq 0, \quad curl\underset{\sim}{\boldsymbol{F}_p} \neq 0 \tag{3.2}$$

where $\underset{\sim}{\boldsymbol{F}_e}$ and $\underset{\sim}{\boldsymbol{F}_p}$ are elastic and plastic deformation tensors, respectively.

If a smooth surface containing lattice vector $\underline{\boldsymbol{x}}$ in the current configuration and bounded by the closed line c, the Burgers vector $\underline{\boldsymbol{b}}$ is defined by:

$$\underline{\boldsymbol{b}} = -\oint_c \underset{\sim}{\boldsymbol{F}_e}^{-1}\mathrm{d}\underline{\boldsymbol{x}} = -\int_s curl\underset{\sim}{\boldsymbol{F}_e}^{-1}\underline{\boldsymbol{n}}\mathrm{d}s \tag{3.3}$$

where $\underline{\boldsymbol{n}}$ the normal to the smooth surface. Meanwhile, the Burgers vector $\underline{\boldsymbol{b}}$ can be obtained by integrating a volume dislocation density tensor $\underset{\sim}{\boldsymbol{\alpha}}$:

$$\underline{\boldsymbol{b}} = \int_s \underset{\sim}{\boldsymbol{\alpha}}\underline{\boldsymbol{n}}\mathrm{d}s \tag{3.4}$$

Often $\underset{\sim}{\boldsymbol{\alpha}}$ is referred to as the Nye's tensor, although the original definition of $\underset{\sim}{\boldsymbol{\alpha}}$ is linked to the lattice rotation gradient (Nye, 1953). Resolving under the assumption

of small deformation, Nye's tensor is related to the elastic distortion tensor by the expression:

$$\underset{\sim}{\boldsymbol{\alpha}} \simeq curl \underset{\sim}{\boldsymbol{U}}_e \tag{3.5}$$

Here one must note that the elastic distortion tensor $\underset{\sim}{\boldsymbol{U}}_e$ is composed of two components. The first is an incompatible part $\underset{\sim}{\boldsymbol{U}}_e^{\perp}$, and the second is a curl-free part $\underset{\sim}{\boldsymbol{U}}_e^{\parallel}$, which, in some situations, guarantees the boundary conditions (Fressengeas, Taupin, and Capolungo, 2011; Fressengeas et al., 2012). Therefore, in an infinite medium the Nye's tensor is connected only to the incompatible part:

$$\underset{\sim}{\boldsymbol{\alpha}} = curl \underset{\sim}{\boldsymbol{U}}_e^{\perp} \tag{3.6}$$

When the dislocation distribution is restricted to a given plane (interface, boundary, wall, etc.), the Nye's tensor becomes a measure of the content of Burgers vectors of dislocations perpendicular to a unit length along a given direction (Bullough and Bilby, 1956). Then, the components of the Nye's tensor become dimensionless. Some simple and relevant cases of stress generated by surface GNDs, are discussed by Fressengeas in (Fressengeas, 2017). The general formulation of Eq. 3.5 is applied to calculate analytically the incompatible part of the elastic distortion associated with infinite-size dislocation walls containing infinite straight dislocations in a linear isotropic elastic medium. Eq. 3.6 can be explicitly expressed as:

$$\underset{\sim}{\boldsymbol{\alpha}} = \begin{pmatrix} \alpha_{xx} & \alpha_{xy} & \alpha_{xz} \\ \alpha_{yx} & \alpha_{yy} & \alpha_{yz} \\ \alpha_{zx} & \alpha_{zy} & \alpha_{zz} \end{pmatrix} = \begin{pmatrix} U_{xz,y} - U_{xy,z} & U_{xx,z} - U_{xz,x} & U_{xy,x} - U_{xx,y} \\ U_{yz,y} - U_{yy,z} & U_{yx,z} - U_{yz,x} & U_{yy,x} - U_{yx,y} \\ U_{zz,y} - U_{zy,z} & U_{zx,z} - U_{zz,x} & U_{zy,x} - U_{zx,y} \end{pmatrix} \tag{3.7}$$

where the upper index ($\perp$) is removed for clarity. When dislocations in a given volume V are divided into small segments, the formulation of $\underset{\sim}{\boldsymbol{\alpha}}$ is given as the following (Kröner, 1963):

$$\underset{\sim}{\boldsymbol{\alpha}} = \frac{1}{V} \sum_{j}^{n} \underline{\boldsymbol{b_i}} \otimes \underline{\boldsymbol{l_j}} \tag{3.8}$$

where $\underline{\boldsymbol{b_i}}$ and $\underline{\boldsymbol{l_j}}$ are, respectively, the Burgers and the line vectors of each dislocation segment. The singularity of surface dislocation density tensor is set when all the line vectors of the segments belong to a given plane. Such distribution is characterized by a 3D – Dirac function ($\delta(x)$) centered on the habit plane.

Now, let us consider three important arrangements of dislocations in a wall. The first one is the twist wall sketched in Figure 3.1a and formed by an infinite number of

infinite straight screw dislocations.

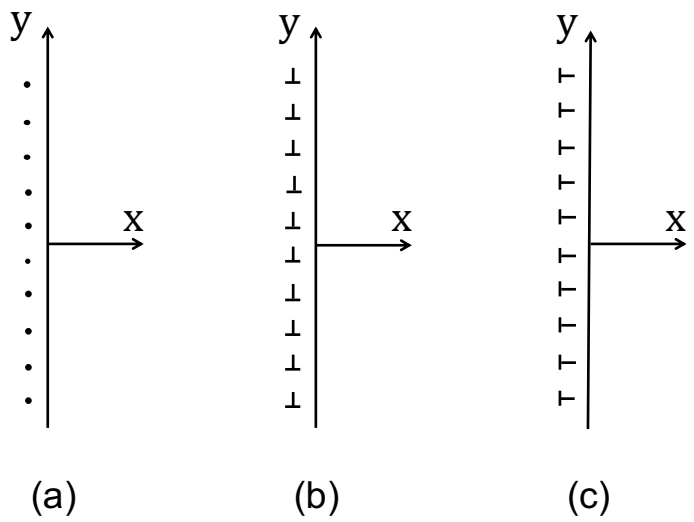

FIGURE 3.1: Schematic illustrations of three fundamental dislocation walls: (a) Infinite straight screw dislocations with Burgers vector in the z direction (twist wall), (b) infinite straight edge dislocations with Burgers vector perpendicular to the wall (tilt wall) and (c) infinite straight edge dislocations with Burgers vector parallel to the wall (epitaxial wall).

Instead of using Eq. 3.8, a surface Nye's tensor is proposed as:

$$\underset{\sim}{\boldsymbol{\alpha}}^{\boldsymbol{s}} = \frac{1}{S}\sum_{j}^{n} \underline{\boldsymbol{b_i}} \otimes \underline{\boldsymbol{l_j}} \tag{3.9}$$

For the "twist wall", only one component of the dislocation density tensor, $\alpha^s_{zz}\delta(x)$, does not vanish. Since the derivative of $\underset{\sim}{\boldsymbol{U}}_{\boldsymbol{e}}$ with respect to y and z are zero, Eq. 3.7 is simplified in the form:

$$\underset{\sim}{\boldsymbol{\alpha}}^{\boldsymbol{s}} = \begin{pmatrix} 0 & 0 & 0 \\ 0 & 0 & 0 \\ 0 & 0 & \alpha^s_{zz}\delta(x) \end{pmatrix} = \begin{pmatrix} 0 & -U_{xz,x} & U_{xy,x} \\ 0 & -U_{yz,x} & U_{yy,x} \\ 0 & -U_{zz,x} & U_{zy,x} \end{pmatrix} \tag{3.10}$$

One equation is given:

$$\alpha^s_{zz}\delta(x) = U_{zy,x} \tag{3.11}$$

To obtain the distortion tensor term, Eq. 3.11 is integrated with a Heaviside function:

$$U_{zy} = \int \alpha^s_{zz}\delta(x)\mathrm{d}x = \alpha^s_{zz}H(x) + A \tag{3.12}$$

The shear stress must change its sign when passing through the surface. By applying this condition to Eq. 3.12, one obtains:

$$U_{zy}(x > 0) = -U_{zy}(x < 0) \tag{3.13}$$

The constant A must thus be equal to -0.5α^s_{zz}, which allows the determination of the elastic distortion $\underset{\sim}{\boldsymbol{U}}_e$. Computing the symmetrical part, and using the Hooke's law, one obtains the stress tensor $\underset{\sim}{\boldsymbol{\sigma}}$. The non-zero stress component on the right side of the surface is:

$$\sigma_{zy}(x \geq 0) = \sigma_{yz}(x \geq 0) = \frac{E}{4(1+\nu)}\alpha^s_{zz} \tag{3.14}$$

where E is the Young's modulus and ν the Poisson's ratio.

When apply to the case of a "tilt wall" illustrated in Figure 3.1b, the same method provides:

$$\sigma_{xy}(x \geq 0) = \sigma_{yx}(x \geq 0) = \frac{E}{4(1+\nu)}\alpha^s_{xz} \tag{3.15}$$

At last, for the "epitaxial wall" illustrated in Figure 3.1c, one obtains three non-zero normal stress components:

$$\begin{aligned}
\sigma_{xx}(x \geq 0) &= \frac{\nu E}{2(1+\nu)(1-2\nu)}\alpha^s_{yz} \\
\sigma_{yy}(x \geq 0) &= \frac{(1-\nu) E}{2(1+\nu)(1-2\nu)}\alpha^s_{yz} \\
\sigma_{zz}(x \geq 0) &= \frac{\nu E}{2(1+\nu)(1-2\nu)}\alpha^s_{yz}
\end{aligned} \tag{3.16}$$

From these three theoretical identifications, one can note that the value of the $\underset{\sim}{\boldsymbol{\sigma}}$ components is always proportional to the surface Nye's tensor $\underset{\sim}{\boldsymbol{\alpha}}^{\boldsymbol{s}}$. This result makes sense as dislocations are the source of stress. In all cases, we can then write:

$$\underset{\sim}{\boldsymbol{\sigma}} \propto \underset{\sim}{\boldsymbol{\alpha}}^{\boldsymbol{s}} \tag{3.17}$$

However,as we will see in the following, the stress solutions in Eqs. 3.15 and 3.16 are not complete. While the solution for the screw dislocations wall (Eq. 3.14) is exact, walls formed of edge dislocations are found to associate with compatible elastic distortion field, which is not accounted for in the integration of Eq. 3.7. The stress components in Eqs. 3.15 and 3.16 represent only the stress induced by the incompatible part of the distortion field generated by the dislocation walls.

In spite of this drawback, we will see that Eqs. 3.15 and 3.16 allow for predictions of the exact wall solutions with the improvements we proposed. To do this, some features of the surface dislocations we observe in realistic dislocation walls should be investigated in priority. First, the dislocation character accumulated at grain boundaries is not always pure (edge or screw) (Sutton and Balluffi, 1995) and, second, the length of the dislocation lines in the walls and the height of the wall are finite and limited by the grain size. These issues will be addressed with dedicated DD simulations latter in this chapter. Another point that needs to be validated with DD simulations is the existence of a linear relation between $\underset{\sim}{\boldsymbol{\sigma}}$ and $\underset{\sim}{\boldsymbol{\alpha}}^s$ in the case of finite walls.

3.1.2 Analytical solution of discrete distribution

In the literature, analytical solutions of the total stress field induced by a stack of straight dislocation lines lined up in a wall are reported. Such solutions make use of the elastic field of infinite straight dislocation given in (Hirth and Lothe, 1982). Two cases must be differentiated: either infinite or finite height wall made of equidistantly distributed infinite dislocation lines. The spacing between dislocations is noted h. Such characteristic length is related to the scalar surface dislocation density ρ^s_{GND} (total length per unit surface) by:

$$h = \frac{1}{\rho^s_{GND}} \tag{3.18}$$

For the three basic dislocation walls illustrated in Figure 3.1, i.e. twist, tilt and epitaxial walls, the discrete dislocation solutions take the form given in the following.

Twist wall

The stress field of a straight screw dislocation with infinite length is by definition:

$$\begin{aligned} \sigma_{xz} &= -\frac{\mu b}{2\pi}\frac{y}{x^2+y^2} \\ \sigma_{yz} &= \frac{\mu b}{2\pi}\frac{x}{x^2+y^2} \end{aligned} \tag{3.19}$$

At first, let's consider a twist wall made of an infinite number of screw dislocations lines. The corresponding stress field is obtained by integration Eq. 3.19:

$$\begin{aligned} \sigma^{\infty}_{xz} &= -\frac{\mu b}{2h}\frac{\sin(2\pi Y)}{\cosh(2\pi X)-\cos(2\pi Y)} \\ \sigma^{\infty}_{yz} &= \frac{\mu b}{2h}\frac{\sinh(2\pi X)}{\cosh(2\pi X)-\cos(2\pi Y)} \end{aligned} \tag{3.20}$$

where $X = x/h$ and $Y = y/h$. As x tends to infinity, for $y = 0$, we have:

$$\begin{aligned} \sigma_{xz}^{\infty} &\to 0 \\ \sigma_{yz}^{\infty} &\to \frac{\mu b}{2h} = \frac{\mu b}{2}\rho_{GND}^{s} = \frac{\mu}{2}\alpha_{zz}^{s} \end{aligned} \tag{3.21}$$

Far from the infinite twist wall, the stress field associated to such screw wall have only one non-zero constant stress component σ_{yz}^{∞}. This result is then in agreement with the continuous solution we reported in the previous section when integrating the surface dislocation density tensor with (see Eq. 3.14).

Secondly, we consider the case of a twist wall with a finite height of $2L$. The stress field of such finite wall is obtained by integrating the stress field of a single screw dislocation line with y bounded between $-L$ to L. Solution for this problem was first reported by Li and Needham (Li and Needham, 1960):

$$\begin{aligned} \sigma_{xz}^{2L} &= -\frac{\mu b}{4\pi h}\ln\frac{x^2+(y+L)^2}{x^2+(y-L)^2} \\ \sigma_{yz}^{2L} &= \frac{\mu b}{2\pi h}\left(\tan^{-1}\frac{y+L}{x} - \tan^{-1}\frac{y-L}{x}\right) \end{aligned} \tag{3.22}$$

In the plane $y = 0$ cutting the finite wall in its middle and far from the finite twist wall, we see that the stress component σ_{xz}^{2L} tends to zero, while σ_{yz}^{2L} decreases with x and take the form:

$$\sigma_{yz}^{2L} = \frac{\mu b}{\pi h}\left(\tan^{-1}\frac{L}{x}\right) = \frac{\mu b}{\pi}\rho_{GND}^{s}\left(\tan^{-1}\frac{L}{x}\right) = \frac{\mu}{\pi}\alpha_{zz}^{s}\left(\tan^{-1}\frac{L}{x}\right) \tag{3.23}$$

Here, it must be noted that the maximum of the stress component σ_{yz}^{2L} is calculated in the close vicinity of the twist wall, i.e. with $x \simeq 0$. In this region, the stress amplitude is $\mu b\rho_{GND}^{s}/2$, which is again the same solution as σ_{yz}^{∞} in Eq. 3.21, the solution obtained in the case of infinite twist wall.

Tilt wall

The stress field of a straight edge dislocation with infinite length is by definition:

$$\begin{aligned} \sigma_{xx} &= -\frac{\mu b}{2\pi(1-\nu)}\frac{y(3x^2+y^2)}{(x^2+y^2)^2} \\ \sigma_{yy} &= \frac{\mu b}{2\pi(1-\nu)}\frac{y(x^2-y^2)}{(x^2+y^2)^2} \\ \sigma_{xy} &= \frac{\mu b}{2\pi(1-\nu)}\frac{x(x^2-y^2)}{(x^2+y^2)^2} \\ \sigma_{zz} &= \nu(\sigma_{xx}+\sigma_{yy}) \end{aligned} \tag{3.24}$$

In the case of an infinite tilt wall and following the same procedure as the one used for twist dislocation wall, the infinite tilt wall stress field solution is:

$$\begin{aligned}
\sigma_{xx}^{\infty} &= -\sigma_0 \sin(2\pi Y)[\cosh(2\pi X) - \cos(2\pi Y) + 2\pi X \sinh(2\pi X)] \\
\sigma_{yy}^{\infty} &= -\sigma_0 \sin(2\pi Y)[\cosh(2\pi X) - \cos(2\pi Y) - 2\pi X \sinh(2\pi X)] \\
\sigma_{xy}^{\infty} &= \sigma_0 2\pi X[\cosh(2\pi X)\cos(2\pi Y) - 1]
\end{aligned} \tag{3.25}$$

where $X = x/h$, $Y = y/h$ and:

$$\sigma_0 = \frac{\mu b}{2h(1-\nu)[\cosh(2\pi X) - \cos(2\pi Y)]^2} \tag{3.26}$$

Here we see that as x tends to infinity and $y = 0$, all the stress components decrease exponentially to zero. Hence, for an infinite tilt wall, no stress field exists far from the wall. This result is in strong disagreement with the solution we previously obtained by integrating the surface dislocation density (Eq. 3.15). The reason is that edge dislocations generate also compatible elastic distortion field, which is absent from the integration of Eq. 3.6. To our knowledge, no analytical treatment is available in the literature to account for the $\underset{\sim}{\boldsymbol{U}}_e^{\parallel}$ distortion field.

Alternatively, in the case of a finite tilt wall of height $2L$, the stress field variation at large distance from the wall takes the form (Li, 1960):

$$\begin{aligned}
\sigma_{xx}^{2L} &= \frac{\mu b}{2\pi(1-\nu)h}\left[\frac{1}{2}\ln\frac{x^2+(y-L)^2}{x^2+(y+L)^2} + \frac{x^2}{x^2+(y+L)^2} - \frac{x^2}{x^2+(y-L)^2}\right] \\
\sigma_{yy}^{2L} &= \frac{\mu b}{2\pi(1-\nu)h}\left[\frac{1}{2}\ln\frac{x^2+(y-L)^2}{x^2+(y+L)^2} + \frac{x^2}{x^2+(y-L)^2} - \frac{x^2}{x^2+(y+L)^2}\right] \\
\sigma_{xy}^{2L} &= \frac{\mu b}{2\pi(1-\nu)h}x\left[\frac{y+L}{x^2+(y+L)^2} - \frac{y-L}{x^2+(y-L)^2}\right]
\end{aligned} \tag{3.27}$$

Again, in the middle plane when $y = 0$, both σ_{xx}^{2L} and σ_{yy}^{2L} are zero and the expression of σ_{xy}^{2L} reduces to:

$$\sigma_{xy}^{2L} = \frac{\mu b}{\pi(1-\nu)h}x\left(\frac{L}{x^2+L^2}\right) = \frac{\mu b \rho_{GND}^s}{\pi(1-\nu)}x\left(\frac{L}{x^2+L^2}\right) = \frac{\mu}{\pi(1-\nu)}\alpha_{xz}^s x\left(\frac{L}{x^2+L^2}\right) \tag{3.28}$$

Thus, we must note here that σ_{xy}^{2L} first increases with x then decreases to zero when x tends goes to infinity. The maximum amplitude is reached at $x = L$ and amounts to $\mu b \rho_{GND}^s / [2\pi(1-\nu)]$.

Epitaxial wall

In the reference system of Figure 3.1c, the stress field of an infinite edge dislocation line take the form given in Eq. 3.24.

From such expression, one can calculate the stress field solution for an infinite epitaxial wall:

$$\begin{aligned}
\sigma_{xx}^{\infty} &= -\sigma_0 2\pi X[\cosh(2\pi X)\cos(2\pi Y) - 1] \\
\sigma_{yy}^{\infty} &= -\sigma_0[2\sinh(2\pi X)(\cosh(2\pi X) - \cos(2\pi Y)) - 2\pi X(\cosh(2\pi X)\cos(2\pi Y) - 1)] \\
\sigma_{xy}^{\infty} &= \sigma_0 \sin(2\pi Y)[\cosh(2\pi X) - \cos(2\pi Y) - 2\pi X \sinh(2\pi X)]
\end{aligned} \tag{3.29}$$

where $X = x/h$, $Y = y/h$ and σ_0 is given in Eq. 3.26.

When x tends goes to infinity, then:

$$\sigma_{xx}^{\infty} \to 0 \quad \text{and} \quad \sigma_{zz}^{\infty} \to 0 \tag{3.30}$$

the only non-zero component σ_{yy}^{∞} converges to:

$$\sigma_{yy}^{\infty} \to -\frac{\mu b}{(1-\nu)h} = -\frac{\mu b}{(1-\nu)}\rho_{GND}^{s} = -\frac{\mu}{(1-\nu)}\alpha_{yz}^{s} \tag{3.31}$$

This result is partly in agreement with the continuum solution we obtained in Eq. 3.16 where three non-zero stress components could be identified. Again, the difference we observe between the continuous and discrete solution comes from the integration of Eq. 3.6 when the compatible part $\underset{\sim}{\boldsymbol{U}}_e^{\parallel}$ is not taken into account.

Alternatively, in the case of a finite epitaxial wall of height $2L$, the stress field takes the form:

$$\begin{aligned}
\sigma_{xx}^{2L} &= -\frac{\mu b}{2\pi(1-\nu)h} x \left[\frac{y+L}{x^2+(y+L)^2} - \frac{y-L}{x^2+(y-L)^2}\right] \\
\sigma_{yy}^{2L} &= -\frac{\mu b}{2\pi(1-\nu)h} x \left[\frac{2}{x}\left(\tan^{-1}\frac{y+L}{x} - \tan^{-1}\frac{y-L}{x}\right) - \frac{y+L}{x^2+(y+L)^2} + \frac{y-L}{x^2+(y-L)^2}\right] \\
\sigma_{xy}^{2L} &= \frac{\mu b}{2\pi(1-\nu)h}\left[\frac{1}{2}\ln\frac{x^2+(y-L)^2}{x^2+(y+L)^2} + \frac{x^2}{x^2+(y-L)^2} - \frac{x^2}{x^2+(y+L)^2}\right]
\end{aligned} \tag{3.32}$$

Now, for $y = 0$ we see that, σ_{xy}^{2L} is equal zero and the expressions of σ_{xx}^{2L} and σ_{yy}^{2L} reduce to:

$$\begin{aligned}\sigma_{xx}^{2L} &= -\frac{\mu b}{\pi(1-\nu)h}\frac{xL}{x^2+L^2} \\ \sigma_{yy}^{2L} &= -\frac{\mu b}{\pi(1-\nu)h}\left[2\tan^{-1}\frac{L}{x} - \frac{xL}{x^2+L^2}\right]\end{aligned} \tag{3.33}$$

The first stress component σ_{xx}^{2L} increases first with x and then decreases to zero at large values of x. This stress profile is similar to the stress field we found for the finite tilt wall. The maximum amplitude equals to $-\mu b\rho_{GND}^{s}\left[2\pi(1-\nu)\right]$ and take place at $x = L$. The second stress component σ_{yy}^{2L} decreases monotonously from $-\mu b\rho_{GND}^{s}/(1-\nu)$ in the vicinity of the wall (when $x = 0$) and goes to zero far from the wall. One must notice that the maximum stress amplitude of σ_{yy}^{2L} is found in agreement with the stress constant σ_{yy}^{∞} calculated above for an infinite epitaxial wall in Eq. 3.31. However there is no consistence between σ_{xx}^{2L} and σ_{xx}^{∞} since the latter converges to zero in Eq. 3.30 .

3.2 Additional investigation with DD simulations

3.2.1 The embedded grain problem

In order to show the possibilities offered by DD simulations on tracking the back stress in a grain and to reproduce size effect, a simple example of simulation is presented in the following. The 3D-DD simulation code and parameters used in this chapter are the same as in Chapter 2. The basic features of this code are presented in the reference (Devincre et al., 2011).

A tensile loading is applied to deform a cubic grain of copper embedded in an elastic continuum up to 0.2% plastic strain. The size of the embedded cubic grain is 10 μm. The tensile axis is chosen in order to plastically deform the grain in single slip. The final state of the dislocation microstructure is shown in Figure 3.2a. The total dislocation density in the grain can be separated into two groups (Figure 3.2b and c).

The first group of dislocations in Figure 3.2b is in the bulk of the grain; they are randomly distributed inside the grain and can be called Statistically Stored Dislocations (SSDs) as the net Burgers vector of their dislocation density equals zero. The second group of dislocations in 3.2c is accumulated very close to the GBs and contains polarized dislocations (dislocations with the same Burgers vector sign). Such dislocation density can be affiliated to Geometrically Necessary Dislocations (GNDs). GNDs are accumulated at the GBs during plastic deformation. In our simulations, GBs are considered as impenetrable interfaces, i.e. GBs act as barriers to dislocation glide. The variation

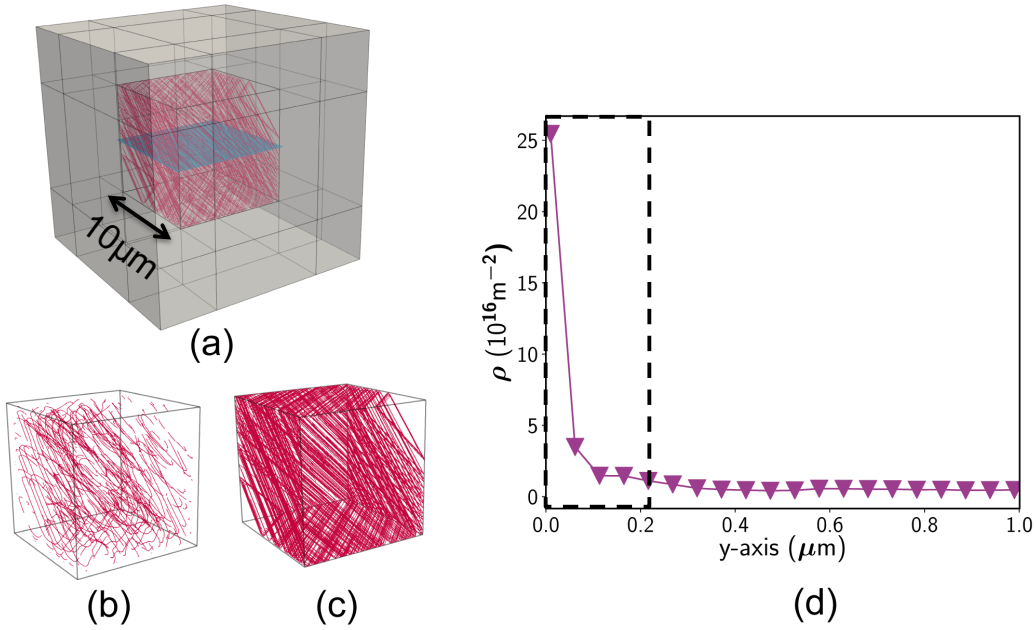

FIGURE 3.2: (a) Distribution of dislocations inside a cubic grain embedded in an elastic continuum at 0.2% of plastic strain. The grain is deformed in single slip with the slip system $(\bar{1}11)[101]$. (b) The dislocations in the bulk of the grain, (c) polarized dislocations (GNDs) accumulated at GBs, (d) dislocation density ρ as a function of the distance to the GBs (ρ is averaged in layers of 0.05 μm thickness parallel to the GB planes.

of the average dislocation density as a function of the distance from the GB is plotted in Figure 3.2d. For such calculation, the dislocation density is computed in layers of 0.05 μm thick parallel to the GB and up to a distance of 1 μm. The dislocation density calculated close to the GB is extremely high and then decreases rapidly to a plateau value of the density. A ratio of about 20 exists between the density found in the vicinity of the GBs and in the grain bulk. Not shown in Figure 3.2d, we checked that beyond the 1 μm region, the dislocation density remains almost constant.

The contribution of SSDs to strengthening and hardening mechanisms is relatively well known. This dislocation density generate short-range stress through the mechanisms of forest interaction and line tension. The mechanical properties associated with SSDs and their contribution to strain hardening was extensively studied with DD simulations for FCC (Devincre, Kubin, and Hoc, 2006) and BCC (Queyreau, Monnet, and Devincre, 2009) crystals during the past years. On the other hand, the detail contribution of GNDs to strain hardening is still a debated question. The goal of the present study is to quantify the mechanical properties of GNDs.

Thanks to the simulation reported in Figure 3.2 as well as other simulations, the distribution of the internal stress inside a grain was investigated to get inputs regarding

the distribution of the back stress inside an embedded grain. As illustrated in Figure 3.2a, a reference plane grid (20 × 20 voxels drawn in blue) cutting the grain in its middle was defined to calculate the internal stress associated with the total density of dislocations (SSDs and GNDs) existing inside the grain. Results of this calculation are reported in Figure 3.3. One must notice here that the internal stress tensor σ_{int} is calculated in each voxel by considering the dislocation microstructure under loading. In Figure 3.3, the distribution of two scalar quantities is used to illustrate the variation of the internal stress, i.e. σ_{vm}, the Von Mises stress and τ, the shear stress resolved on the active slip system. Except for the outermost layer of the grid, the amplitudes of σ_{vm} and τ are found almost constant inside the grain. Such homogeneous distribution of the stress inside the grain can be explained by the homogeneous density of dislocations accumulated at the GBs. Such distribution presents strong similitude with the solutions previously discussed for the infinite dislocation walls. The stress calculated in the outermost layer is close to the GBs. Then, it is a region where the stress locally can vary rapidly and strongly as function of the relative position of the closest dislocation staying at the GBs. This is why in average the stress in the outermost layer goes to zero. In summary, one must note that the internal stress distribution was always found to be relatively homogeneous inside the tested embedded grains.

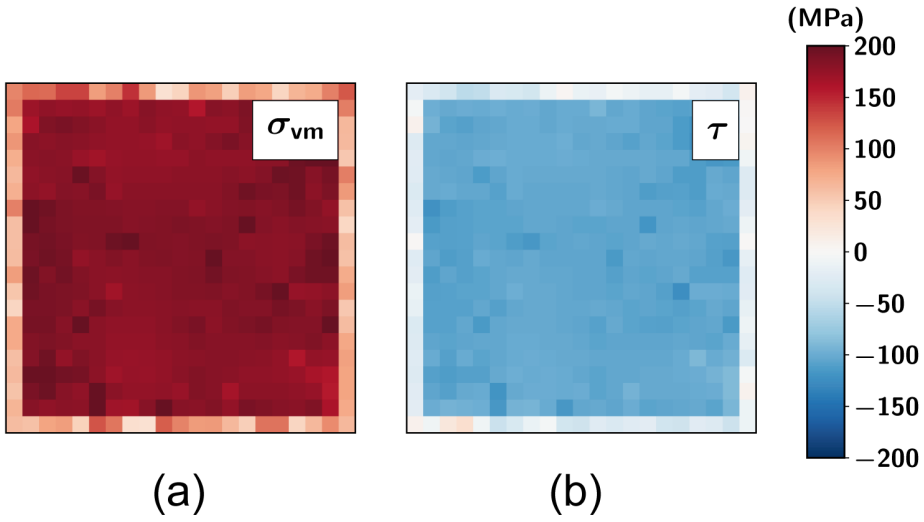

FIGURE 3.3: The stress state calculated at 0.2% (under load) in a grid of 20x20 voxels, normal to z-axis and cutting the middle of the embedded grain (see Figure 3.2). (a) The Von Mises stress (σ_{vm}) and (b) the resolved shear stress τ on the active slip system are calculated from the total internal stress tensor.

In the following, we made some additional DD simulations to identify some relevant parameters needed to calculate the amplitude of the internal stress inside a grain assuming that we know the surface density of dislocation accumulated at the GBs.

3.2.2 Simulations of regular dislocation facets

The aim of this section is to precisely characterize the stress field induced by a wall composed of dislocations of finite length. As we are now dealing with the walls of dislocations limited in both height and width, for the sake of clarity, this type of wall is hereafter referred to as "facet". In Figure 3.4, three sets of dislocation arrangements was generated to model the basic characters of dislocation wall first presented in Section 3.1.2. DD simulations allow computing the exact stress fields associated with such microstructure and comparison with the theoretical expressions reported above.

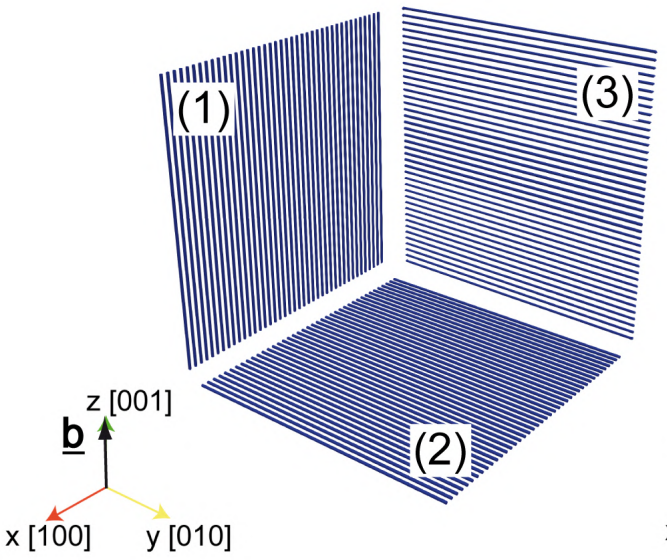

FIGURE 3.4: Different characters of surface dislocations. The three directions of the basis (xyz) coincide with the lattice orientations <100>. In simple cubic symmetry lattice having fixed Burgers vector $\underline{\boldsymbol{b}}$ parallel to [001] orientation, three facets containing finite straight dislocation lines are lined up equidistantly. (1) Twist facet; (2) tilt facet and (3) epitaxial facet.

The geometry and dimension of the dislocation facets considered for those simulations are reported in Table 3.1 and Table 3.2, respectively.

	Twist facet	Tilt facet	Epitaxial facet
Burgers vector $\underline{\boldsymbol{b}}$	[001]	[001]	[001]
Plane normal $\underline{\boldsymbol{n}}$	[010]	[001]	[010]
Line direction $\underline{\boldsymbol{l}}$	[00$\bar{1}$]	[010]	[0$\bar{1}$0]

TABLE 3.1: Crystallographic definition of the three facet configurations investigated with DD simulations.

All the tested dislocation facets are of rectangular shapes, with two independent dimensions; the height H and the width L. For each type of facets, different shapes and

sizes were considered (noted S1, S2, S3 and S4 as reported in Figure 3.5 with an identical surface dislocation density $\rho^s_{GND} = 4.1 \times 10^6$ m^{-1}). In the following, the dimensionless variable R denotes the aspect ratio of the facet height H and the facet width L.

	S1	S2	S3	S4
H (μm)	10	5	10	5
L (μm)	10	5	5	10
$R = H/L$	1	1	2	0.5

TABLE 3.2: Definition of the different facet shapes investigated with the DD simulations. All the tested dislocation facets are rectangular with height noted H and width noted L. The facets shapes S1-S4 are illustrated in Figure 3.5.

To compute the average stress induced by the tested facet as a function of the distance to the facet, the stress field of each dislocation in the facets is averaged on a 3D grid parallel to the wall, as illustrated in Figure 3.5. The height and width of this computation grid are by definition taken half of the tested wall height and width, respectively.

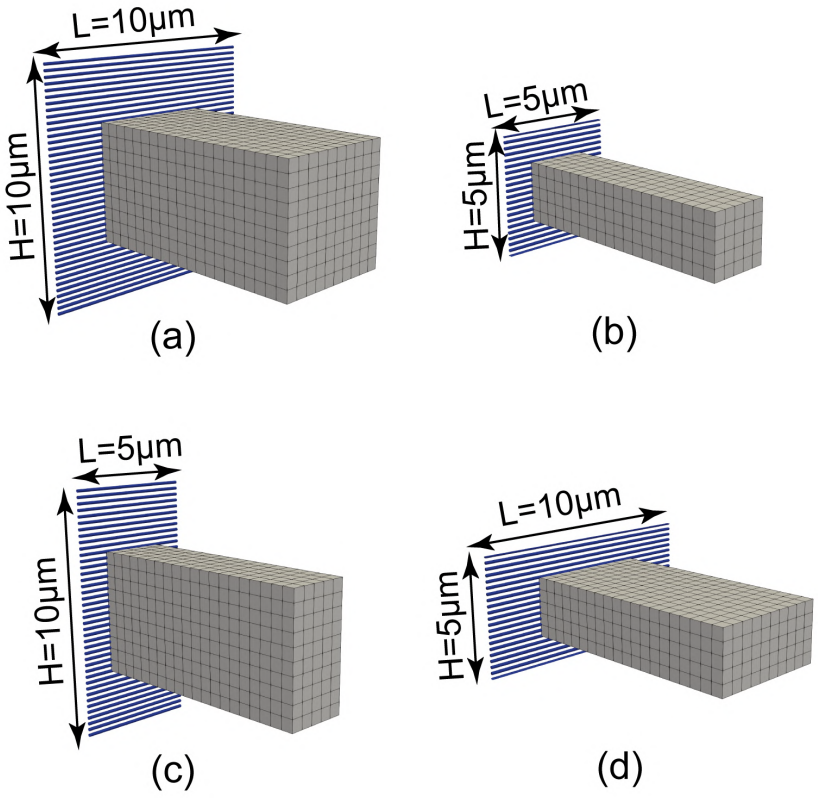

FIGURE 3.5: For each facet character, different shapes of the facets are considered. The grey slices indicates the layers in which the stresses are averaged. The images (a)-(d) correspond to the facets shapes S1-S4 defined in Table 3.2.

In addition, to check the influence of the surface dislocation density on the stress field $\underset{\sim}{\boldsymbol{\sigma}}$, three additional configurations was tested. In this second type of simulations, only square facets are considered (type S1 of Table 3.2). To induce a variation of ρ^s_{GND}, the number of dislocations lines is increased as shown in Figure 6. The three different densities we tested for each facet character (twist, tilt and epitaxial) are given in Figure 3.6.

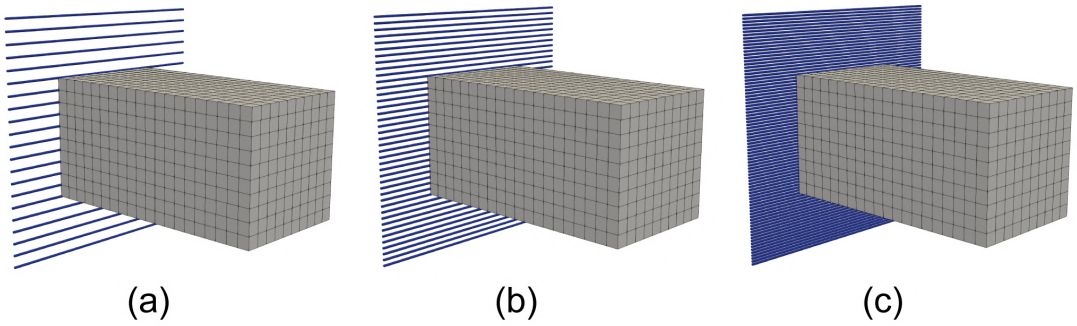

FIGURE 3.6: For a given geometrical facet shape S1 (see Table 3.2), dislocation lines of different numbers are inserted equidistantly. The corresponding surface GNDs densities are $\rho^s_{GND} = 2.1 \times 10^6$ m^{-1} in (a), $\rho^s_{GND} = 4.1 \times 10^6$ m^{-1} in (b) and $\rho^s_{GND} = 8.1 \times 10^6$ m^{-1} in (c).

Twist dislocation facets

Thanks to the simple cubic symmetry we defined in Table 3.1, the plane normal to the twist facets we investigated is parallel to y-axis (see Figure 3.4). The stress variation with distance from the GB calculated for such facets is plotted in Figure 3.7a. In agreement with theoretical solution of FDM, only one non-zero stress component σ_{zx} is found for all the tested facet shapes. The stress variations of σ_{zx} for S1, S2, S3 and S4 are plotted in Figure 3.7a. As expected, the stress amplitude decreases with the distance from the facet. The maximal value we calculate, is the same for all configurations and is always obtained close to the facet, at $y = 0$. This stress calculated close to the facet can be rationalized for all the simulations since the surface dislocation density ρ^s_{GND} is constant. According to the model of infinite twist wall, the stress for an infinite wall is constant given in Eq. 3.14 (this theoretical solution is reported in Figure 3.7a with the plateau in black). Logically, this value is very close to the maximal stress computed in the simulations at short distance of the twist facet.

In addition, the simulation results show that the finite size of a dislocation facet leads to a rapid decrease of the stress with the distance from the facet. From this result, we expect that the back stress of a twist dislocation facet accumulated at GBs decreases rapidly within the grain.

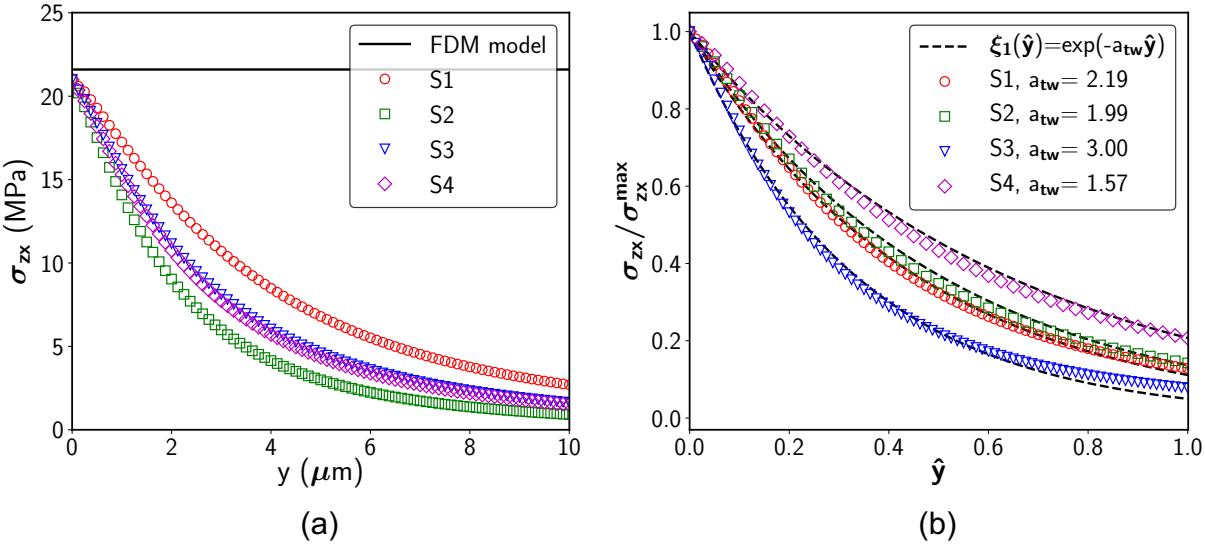

FIGURE 3.7: (a) Variation of σ_{zx} with the distance from the twist facet for the different simulated facet shapes (see Table 3.2). The solid black line corresponds to the theoretical solution calculated for an infinite twist wall given in Eq. 3.14. (b) Same curves as (a) but the stress is normalized by the maximum stress σ_{zx}^{max} and the distance y is normalized by the facet heights H ($\hat{y} = y/H$). Dashed lines are solutions of a fitting made with the shape function $\xi_1(\hat{y})$= exp(-$a_{tw}\hat{y}$) where a_{tw} is the coefficient determined by the fitting procedure.

An additional feature to notice in Figure 3.7a, is that the different shapes, even with a constant surface density, produce different stress profiles. This evidences the fact that a decrease in the facet length is not equivalent to the decrease of the facet height.

Tilt dislocation facets

Edge dislocations are used to build tilt facets with a normal axis parallel to the z-axis (see Table 3.1). The stress variations with the distance z we computed for S1, S2, S3 and S4 are plotted in Figure 3.8a. Again, only one non-zero stress component σ_{zx} is found in all the tested facet shapes. This result is in agreement with the theoretical predictions made in Section 3.1.1. However, instead of being a constant, all the calculated profiles exhibit the same tendency: an increase from zero stress (close to the facet) up to a maximum and a decrease to zero far from the facets. These stress variation profiles are quite different (in magnitude and trends) from the continuum solution given in Eq. 3.15 for an infinite tilt wall. For comparison, the latter prediction is plotted with a straight line in Figure 3.8a.

Based on the Hirth's analytical formulations, Saada *et al.* (Saada and Bouchaud, 1993) calculated the stress field associated with a finite tilt wall made of infinite straight edge dislocations. From such calculation, it was reported that the stress peak, whatever

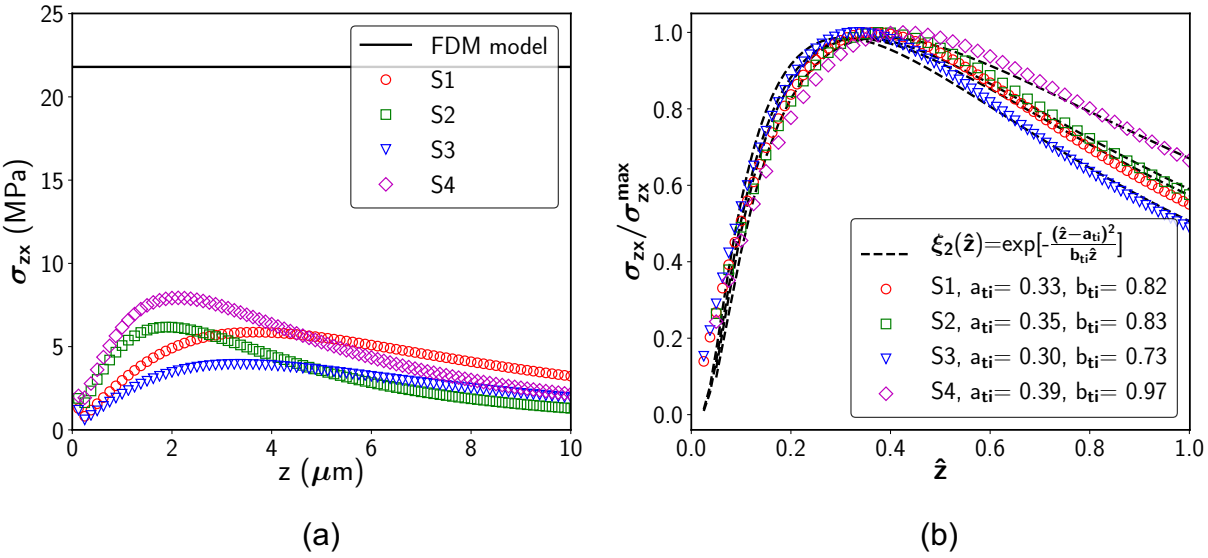

FIGURE 3.8: (a) Variation of σ_{zx} with the distance from the tilt facet for the different simulated facet shapes (see Table 3.2). The solid black line corresponds to the theoretical solution calculated for an infinite tilt wall given in Eq. 3.15. (b) Same curves as (a) but the stress is normalized by the maximum stress σ_{zx}^{max} and the distance z is normalized by the interface heights H ($\hat{z} = z/H$). Dashed lines are fitting results made with the shape function $\xi_2(\hat{z}) = \exp\left[-(\hat{z} - a_{ti})^2/b_{ti}\hat{z}\right]$ where a_{ti} and b_{ti} are the coefficients to determine by the fitting procedure.

the dislocation density in the wall, always appears at a distance equal to half the wall height. Our calculations based on finite facets exhibit a stress peak systematically much closer to the facets. For the calculations S1 and S3, the facets' height is $H = 10\ \mu m$ and the stress maximum is located around $z = 3.5\ \mu m$. For the configurations S2 and S4, the facets' height is $H = 5\ \mu m$ while the stress maximum is found around $z = 2\ \mu m$. Unlike the straight infinite dislocation lines considered in the analytical calculation, the length of dislocation lines in the simulated facets is finite and that results in the shift of the stress peaks.

This remark is consolidated when comparisons are made between the stress curves associated with the calculations S1 and S3 or S2 and S4. The maximal stress amplitude is found to be higher when the dislocation length in the facets is increased. Consequently, we note that the amplitude and position of the maximal stress are both dependent on the shape of the tilt facet.

Epitaxial dislocation facets

In those simulations, edge dislocations with in-plane Burgers vector are used to build facets with a normal axis parallel to the x-axis (see Table 3.1). These epitaxial facets are made of edge dislocations similar to those observed in thin films interfaces to relax misfit

stress. Unlike the two previous types of facets, epitaxial facets give rise to three normal stress components σ_{xx}, σ_{yy} and σ_{zz}. For interface shape S1, the corresponding three stress variations with distance along x-axis are plotted in Figure 3.9. The two normal stress components σ_{yy} and σ_{zz} follow the same trend as the shear stress generated by the twist facets; the last normal stress component σ_{xx} has a behavior similar to the one associated with tilt facets. More details regarding the facet-shape dependency for each stress component are presented in Appendix A.

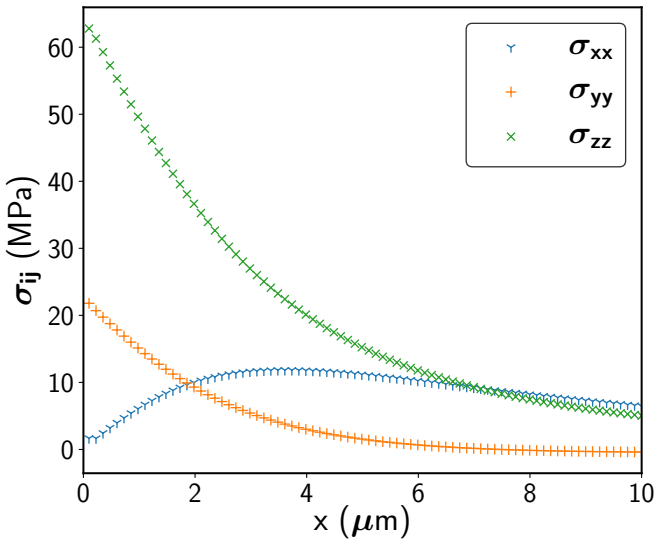

FIGURE 3.9: Normal stress components induced by an epitaxial facet of shape S1.

To facilitate the discussion of the results in the following sections, we decide to denote the three normal stress components in the following order:

- 1^{st} component: parallel to the Burgers vector $\underline{\boldsymbol{b}}$
- 2^{nd} component: parallel to the the plane normal $\underline{\boldsymbol{n}}$
- 3^{rd} component: parallel to the the line direction $\underline{\boldsymbol{l}}$

Adjustment of DD results

As illustrated in the previous sections, analytical forms derived from Eq. 3.14-3.16 do not allow for the prediction of the back stress induced by dislocation facets. Even when no compatible part of the elastic distortion is present, the finite dimensions (height and length) of the dislocation twist facets prevent the use of analytical forms when the back stress is calculated far from the facet. However, the stress solutions developed from FDM for infinite dislocation walls are simple and allow the identification of non-zero

stress components.

Since no analytical description of the back stress associated with a dislocation facet is available, we propose an empirical approach based on a fitting of our DD results scaled with the analytical forms derived from Eq. 3.5. Such fitting procedure is made in two steps. We first determine for the many dislocation facets we simulated, an intensity factor F between the maximum stress computed σ^{max} and the theoretical stress σ^{FDM} calculated with Eq. 3.5. Then, we identify a shape function $\xi(\hat{x})$ dedicated to the description of the stress variation profile with respect to the distance to the facet, in which $\hat{x}$ a dimensionless term is the true distance to the facet normalized by the facet height H. These features could be identified for the three types of dislocation facets we considered with DD simulations results and such calculations are presented below.

- Identification of the intensity factor F

The value for σ_{zx}^{max} we calculated for all the tested twist facets appear to be very close to the theoretical prediction of σ^{FDM} (see Figure 3.7). The intensity factor F_{tw} (the index "$_{tw}$" stands for twist facet) is thus taken:

$$F_{tw} = 1 \tag{3.34}$$

For the simulations of the tilt facets, σ^{max} was found to vary with the dislocation facet shape (see Figure 3.8). The factors F_{ti} we found for the 4 tested facets are listed in Table 3.3.

Tilt facets	$R = H/L$	$F_{ti} = \sigma^{max}/\sigma^{FDM}$
S1	1	1/4
S2	1	1/4
S3	2	1/6
S4	1/2	1/3

TABLE 3.3: Identification of the intensity factor F for the 4 different shapes of tilt facets simulated.

As can be seen in the Table 3.3, F_{ti} evolves according to a rule imposed by the facet shape. Its variations can be expressed with a simple function of the aspect ratio R:

$$F_{ti} = \frac{1}{2(1+R)} \tag{3.35}$$

Finally, the same identification procedure was applied to the case of epitaxial facets. As shown in Appendix A, the 3 factors F_{epi} (the index "$_i$" indicates the order of three

normal stress components given in Section 3.2.2) needed for the epitaxial facets appear to be constant values like in the case of twist facet. The calculated solution for the stress components are :

$$\begin{aligned} F_{ep1} &= 0.36 \\ F_{ep2} &= 0.09 \\ F_{ep3} &= 0.16 \end{aligned} \tag{3.36}$$

- Determination of the shape function $\xi(\hat{x})$

Analysis of the stress profiles reported in Figures 3.7, 3.8 and 3.9 suggested that two shape functions $\xi_1(\hat{x})$ (for monotonous decrease) and $\xi_2(\hat{x})$ (with peak stress) can be used to fit the dislocation facet results:

$$\xi_1(\hat{x}) = \exp(-a\hat{x}) \tag{3.37}$$

$$\xi_2(\hat{x}) = \exp\left[-\frac{(\hat{x}-a)^2}{b\hat{x}}\right] \tag{3.38}$$

With the help of those two shape functions, monotonously decreasing stress component $\sigma(x)$, can be fitted with:

$$\sigma(x) = F_i \sigma^{FDM} \exp(-a_i \hat{x}) \tag{3.39}$$

and the stress profile exhibiting a peak, can be fitted with:

$$\sigma(x) = F_i \sigma^{FDM} \exp\left[-\frac{(\hat{x}-a_i)^2}{b_i \hat{x}}\right] \tag{3.40}$$

where F_i, a_i and b_i are the adjusted parameters we calculated from DD simulation results. $\hat{x}$ the true distance x from the facet center normalized by the facet height H ($\hat{x} = x/H$).

As illustrated in Figure 3.7b, the parameter a_{tw} appearing in the shape function for the twist facets is found to vary linearly with the aspect ratio R:

$$a_{tw} = 1.1 + 0.95R \tag{3.41}$$

In the case of the tilt facets, the two parameters appearing in Eq. 3.37 are also found to vary linearly with the aspect ratio. Such variations take the form:

$$\begin{aligned} a_{ti} &= 0.4 - 0.05R \\ b_{ti} &= 1 - 0.15R \end{aligned} \tag{3.42}$$

For the case of epitaxial facets we must differentiate two cases. The modeling of components σ_{zz} and σ_{yy}, involves shape function with only one fitting parameter given with Eq. 3.37, see Figure A.1-A.3 in Appendix A. Like in the case of twist facets, the variation of parameter a_i is linear and takes the form:

$$\begin{aligned} a_{ep1} &= 1.8 + 0.9R \\ a_{ep3} &= 3.6 + 0.8R \end{aligned} \tag{3.43}$$

Finally, the profile of σ_{xx} associated with epitaxial facets in Figure A.2 exhibits a peak and therefore its modeling involves a shape function with two fitting parameter parameters (Eq. 3.38). Result of the two parameters adjustments gave again a linear function of the facet aspect ratio:

$$\begin{aligned} a_{ep2} &= 0.46 - 0.12R \\ b_{ep2} &= 1.2 - 0.33R \end{aligned} \tag{3.44}$$

Considering a facet of shape S1 ($R = 1$), we can eventually give the simplified expressions of stress calculated at a distance half of the facet height ($\hat{x} = 1/2$) from the facet center for all the three characters of facets. Here, the final stress solutions for twist and tilt facets deduced from Eq. 3.39-3.40 are quite simple.

For a twist facet:

$$\begin{aligned} F_{tw} &= 1 \\ a_{tw} &= 2 \end{aligned} \xrightarrow{Eq.3.39} \sigma_{tw} \simeq \sigma^{FDM} \exp(-1) = 0.37 \times \frac{E}{4(1+\nu)} \alpha^s_{tw} \tag{3.45}$$

For a tilt facet:

$$\begin{aligned} F_{ti} &= 0.25 \\ a_{ti} &= 0.35 \\ b_{ti} &= 0.85 \end{aligned} \xrightarrow{Eq.3.40} \sigma_{ti} \simeq 0.25\sigma^{FDM} \exp(-0.05) = 0.24 \times \frac{E}{4(1+\nu)} \alpha^s_{ti} \tag{3.46}$$

where the theoretical solution of σ^{FDM} is given in Eq. 3.14 and Eq. 3.15.

$\rho^s_{GND}\,(\times 10^6 m^{-1})$	F_{tw}	a_{tw}	F_{ti}	a_{ti}	b_{ti}	F_{ep1}	a_{ep1}	F_{ep2}	a_{ep2}	b_{ep2}	F_{ep3}	a_{ep3}
2.1	1	2.28	0.25	0.34	0.85	0.36	2.70	0.09	0.33	0.83	0.16	4.62
4.1	1	2.19	0.25	0.33	0.82	0.36	2.74	0.09	0.33	0.82	0.16	4.59
8.1	1	2.20	0.25	0.33	0.81	0.36	2.76	0.09	0.33	0.82	0.16	4.58

TABLE 3.4: Based on the configurations illustrated in Figure 3.5, intensity factors F and shape functions $\xi(\hat{x})$ parameters (one parameter a a for inverse-exponential distribution type; two parameters a and b for log normal distribution type) are determined for three tested surface GNDs density ρ^s_{GND}.

Influence of the dislocation density in dislocation facets

As we mentioned before, the stress associated to the dislocation facets is expected to be proportional to the surface dislocation density. However, this result was obtained for infinite dislocation interfaces and it must be confirmed for finite dislocation facets. To do such validation, facets with three surface dislocation densities were tested with the square facet S1 and for the three types of dislocation interfaces, i.e. twist, tilt and epitaxial facets. The stress profiles of these 9 simulations were fitted using the procedure described above. The identified parameters are given in Table 3.4.

From those calculations it is apparent that all the parameters we identified in the previous section are independent or vary very slightly with ρ^s_{GND}. This important result confirms that the long-range stress field (back stress) associated to dislocation facets is always proportional to the surface dislocation density even in the case of small facet of dislocation wall.

3.3 Faceted grain simulations

3.3.1 Back stress calculation in any faceted grain

The calculations presented in the previous section have been made assuming for reason of simplicity a simple cubic crystal symmetry. Besides, computations of the stress associated to dislocations paving the facets have been simplified by considering <100> type planes. In the general case, for instance involving an FCC symmetry and dislocation of mixed character accumulated at GBs, the surface Nye's tensor $\underset{\sim}{\boldsymbol{\alpha}}^s$ may contain up to 9 non-zero components and the GB normal may be of any orientation. In order to generalize the model equations developed in the previous section, we first consider the case of FCC dislocations accumulated at the GBs of a cubic grain with facets of <100> orientations.

With such configuration, the dislocations accumulated at GB are dislocations of mixed character type. Then, the superposition of dislocations coming from different slip systems gives on each grain facets a surface Nye's tensor with 9 components different from zero.

In this section, the procedure we developed to decompose any complex GB configuration is explained. This solution makes use of a decomposition of the dislocation GB facet into in simpler counterparts based on the cubic simple symmetry. This way, we treat each component of the surface Nye's tensor as a separate GB element made of twist, tilt or epitaxial dislocation facet. Here it must be noted that such decomposition into simple cubic symmetry is the one we tested in the previous Section 3.2.2. The forms we proposed can then be used to calculate the stress associated to any facet of GB. Once calculations are made for each Nye's tensor component, the total stress tensor induced by the real dislocations paving a GB facet can be obtained by summing the contributions of every component and common rotation operations to account for the true direction of the facet normal.

The correspondence between the Nye's tensor components and the dislocation lines and Burgers vector symmetry we used are reported in Table 3.5.

$\underset{\sim}{\boldsymbol{\alpha}}^s$	$\underline{\boldsymbol{b}_s}$	$\underline{\boldsymbol{l}_s}$
α^s_{xx}	[100]	[100]
α^s_{xy}	[100]	[010]
α^s_{xz}	[100]	[001]
α^s_{yx}	[010]	[100]
α^s_{yy}	[010]	[010]
α^s_{yz}	[010]	[001]
α^s_{zx}	[001]	[100]
α^s_{zy}	[001]	[010]
α^s_{zz}	[001]	[001]

TABLE 3.5: Projection of the surface tensor Nye's tensor $\underset{\sim}{\boldsymbol{\alpha}}^s$ components on the simple cubic symmetry. The Burgers vector and dislocation line vector are indicated.

A simple example of facet calculation with the FCC crystal symmetry is shown in Figure 3.10. The size of the present facet is 10×10 μm. In such calculation, the facet plane is perpendicular to z-axis and contains mixed dislocations of Burgers vector parallel to [101] and line direction parallel to [110], equidistantly distributed in the plane.

The obtained surface Nye's tensor $\underset{\sim}{\boldsymbol{\alpha}}^{\boldsymbol{s}}$ is:

$$\underset{\sim}{\boldsymbol{\alpha}}^{\boldsymbol{s}} = \begin{pmatrix} \alpha^s_{xx} & \alpha^s_{xy} & 0 \\ 0 & 0 & 0 \\ \alpha^s_{zx} & \alpha^s_{zy} & 0 \end{pmatrix} = \delta(\mathrm{z}) \begin{pmatrix} 6.3 & 6.3 & 0 \\ 0 & 0 & 0 \\ 6.3 & 6.3 & 0 \end{pmatrix} \tag{3.47}$$

where $\delta(\mathrm{z})$ is the Dirac distribution function. Here it must be noted that in the expression of $\underset{\sim}{\boldsymbol{\alpha}}$, there is no component in the third column because there is no component of the dislocation line out of facet. See Figure 3.10a, the plane normal $\underline{\boldsymbol{n}}$ is parallel to z-axis in the [001] direction. Following our cubic simple decomposition, this GB facet made of mixed FCC dislocations can be decomposed as follows. The component α^s_{xx} can be attributed to dislocations with $\underline{\boldsymbol{b_s}} = [100]$ and $\underline{\boldsymbol{l_s}} = [100]$, which corresponds to screw dislocations forming a twist facet. The component α^s_{xy} can be attributed to dislocations with $\underline{\boldsymbol{b_s}} = [100]$ and $\underline{\boldsymbol{l_s}} = [010]$, which correspond to edge dislocations forming an epitaxial facet. Lastly, the two component α^s_{zx} and α^s_{zy} correspond to dislocations with $\underline{\boldsymbol{b_s}} = [001]$ and $\underline{\boldsymbol{l_s}} = [100]$) and also $\underline{\boldsymbol{b_s}} = [001]$ and $\underline{\boldsymbol{l_s}} = [010]$, respectively, forming two edge dislocation sets in tilt facet configurations.

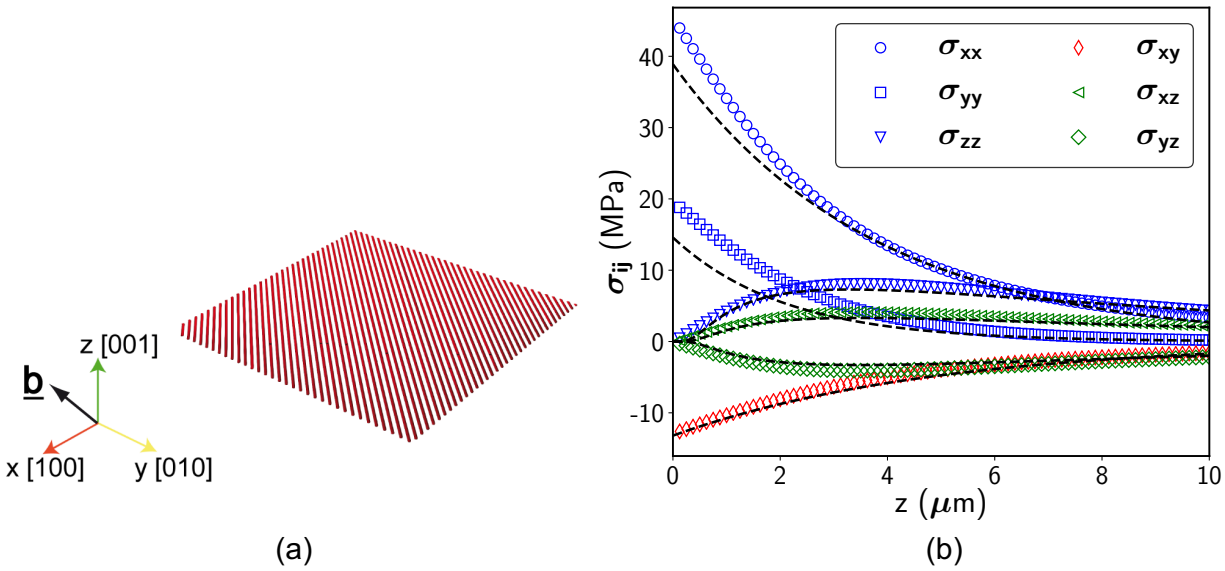

FIGURE 3.10: Example of stress calculation for a facet including dislocation of one FCC slip system. The size of the present facet is $10 \times 10\ \mu m$ and the surface dislocation density is $\rho^s_{GND} = 4.94 \times 10^6 m^{-1}$. (a) The [001] facet with mixed FCC dislocations ($\underline{\boldsymbol{b}}$ parallel to [101] and line direction $\underline{\boldsymbol{l}}$ parallel to [110]), (b) the full stress tensor as a function of the distance z to the interface. Open symbols refer to the stress computed with DD simulations and the dashed lines correspond to the predictions made with the simple cubic symmetry decomposition.

In Figure 3.10b, we show with dashed lines the results of the model decomposition

using the simple cubic geometry. The total stress tensor associated to the mixed dislocation facet is decomposed into four elementary facets. More precisely, the component α^s_{xx} induces the stress stress σ_{xy}, the component α^s_{xy} is at the origin of the three normal stress σ_{xx}, σ_{yy} and σ_{zz} and the components α^s_{zx} and α^s_{zy} induce the shear stress σ_{yz} and σ_{xz}, respectively. When comparing with the stress solution computed with the DD simulation (shown in open samples), an excellent agreement is found for the 6 stress components. For only two stress components of the elementary epitaxial facet (σ_{xx} and σ_{yy}), the agreement is less good at distance smaller than 3 μm from the 10 μm high facet. Close to the dislocation facet, the maximum error with the use of the model is about 25%. We verified that such discrepancy was not related to the decomposition procedure. It was mainly caused by the fact that dislocation lines in Figure 3.10a are different in length.

3.3.2 Systematic validation tests

To extend the validation of our empirical model, we checked the simulation configurations with increasing complexity. DD simulations were carried out on three sets of configurations based on cubic grains of dimensions 10 μm (see Figure 3.11):

Set 1

This type of configuration is made of a fixed number of dislocation loops expanded to the GBs of a cubic grain. Such distribution of dislocations at the GBs is made artificially by expending tiny dislocation glissile loops distributed along the [111] diagonal axis of the cubic grains. A high stress is then applied to force the extension of the loops until they are stopped at GBs. The final states of the simulations used for the back-stress calculations are illustrated in Figure 3.11. Three loops distributions were considered: (a) the loops are uniformly distributed and belong to one slip system, (b) the loops are uniformly distributed and belong to three slip systems gliding in different plane directions, (c) the loops are randomly distributed and belong to one slip system.

Set 2

Frank-Read (FR) sources are now initially inserted in the grains and the latter is deformed to expand dislocation lines to the GBs. The distribution of the FR source is random and the length of the sources is 3 μm. The initial dislocation density is 2×10^{12} m^{-2} in these simulations. In Figure 3.11 (d) only one active slip system (loading conditions is tension along the [135] axis); (e) four active systems (loaded along the [101] tensile axis) and (f) eight active slip systems (loaded along the [100] tensile axis).

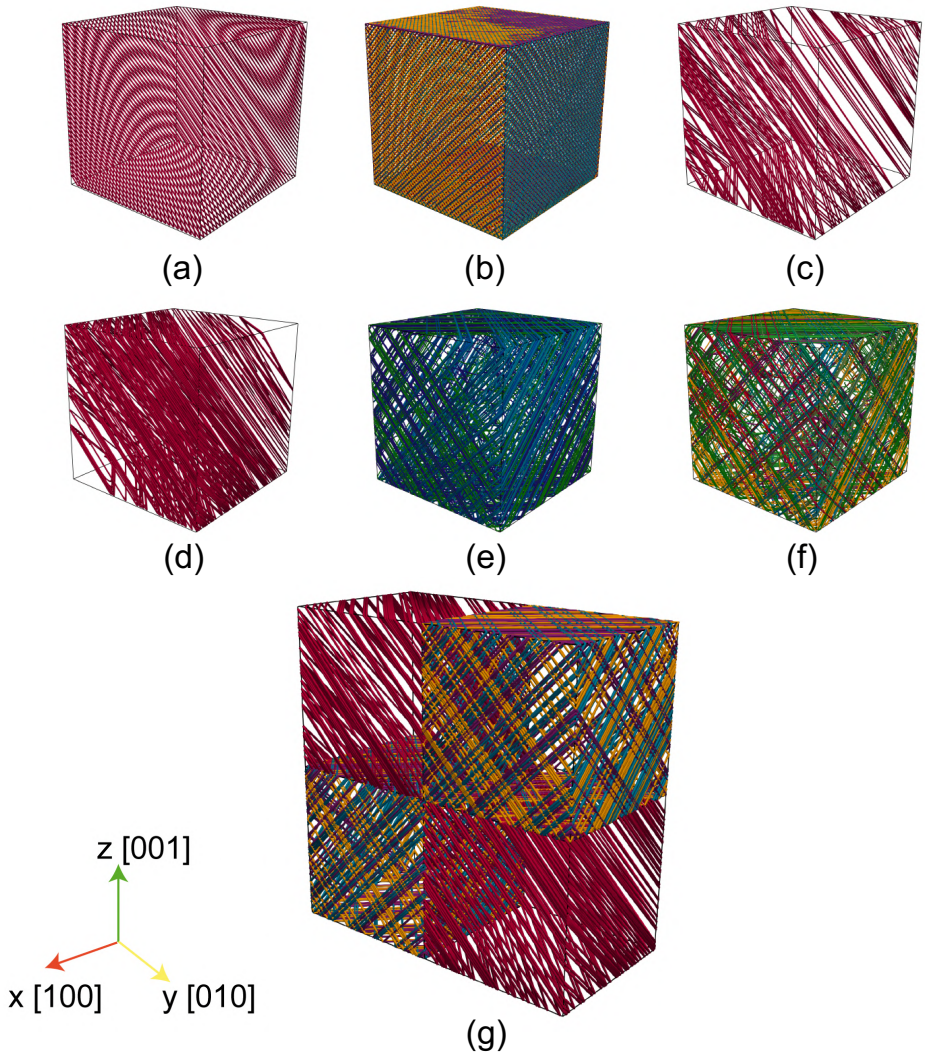

FIGURE 3.11: A series of DD simulations are carried out in order to test the validity of the improved model. (a) - (f) Final states of grains embedded in an elastic matrix with different initial simulation configurations. (a) Glissile loops belonging to (a) uniform distribution of loops on one slip system, (b) uniform distribution of loops on three slip systems, (c) random distribution of loops of one slip system, (d) random distribution of FR sources loaded to activate one slip system, (d) random distribution of FR sources loaded to activate four slip systems, (d) random distribution of FR sources loaded to activate eight slip systems, (g) periodic aggregate of four grains loaded in two different orientations with randomly distributed glissile loops belonging to one or three slip systems.

Set 3

The dislocation microstructure used in this configuration is similar to the one considered in Chapter 2. Only one simulation was carried out here with an aggregate of four cubic grains (see Figure 3.11g) The simulation conditions was made such that two grains are in single slip conditions and two grains are deformed with three active slip systems

having the same Schmid factor. The grains in single slip are made from 101 randomly distributed glissile loops. The grains in multiple slip are made from 51 randomly distributed glissile loops per slip system. A high stress is applied to extend such loops to the GBs.

Prediction of back stress

In Set 1, the loading procedure we impose leads to plastic strain exhaustion at the end of simulation when all the dislocation segments are deposed at GBs. The inner area of the grain is then empty and the internal stress inside the grain is uniquely induced by the GB dislocations. Since the tested grains in Set 1 are inserted in an elastic medium, the dislocations at the GBs are fully polarized, acting as surface GNDs. Then it is straightforward to use the model presented above to calculate the back shear stress (τ_{back}^{pred}) on the slip systems and to compare this calculation with the shear stress computed directly from DD simulations (τ_{back}^{DD}). Such comparison is made by considering the stress at the center of the grain.

The dislocation microstructure tested in Set 2 present different characteristics. During loading, the FR sources continuously emit dislocation loops. The dislocation microstructure must then be divided into two populations: bulk dislocations can be assumed to be SSDs and dislocations stopped at the GBs are polarized and therefore must be defined as GNDs. This particular dislocation microstructure is illustrated in Figure 3.2a, which corresponds to the grain (d) in Figure 3.11. As can be seen from the dislocation density distribution in Figure 3.2b, the frontier between the two dislocation populations is not obvious. This is why we made a somehow arbitrary truncation at 0.4 μm from the GBs. The surface Nye's tensor is computed from all segments included to this layer. Outside this layer, dislocations are considered as SSDs. This hypothesis was tested by computing with the DD the stress associated to the dislocation density not considered in the surface density calculation. As expected such stress was found to be quite low at the grain center. Once the surface dislocations are identified, τ_{back}^{pred} and τ_{back}^{DD} are determined following the same procedure as in Set 1 simulations.

Lastly, it must be noted that in the simulation of the four-grain aggregate, the dislocations belonging to the different slip systems are deposed at GBs on both sides of the interface, hence in this calculation, the dislocation density at the GBs is a mix of several GND walls superposed. This last calculation is essential to validate elastic screening of the dislocations accumulated on both side of the grains and to see the validity of our model which is considering only the surface Nye's tensor.

As a general remark, the internal stress calculated in all the DD simulations was found almost uniform inside the grains (see Figure 3.3). This is why, for a simple comparison between the predicted and computed stresses we considered the stress associated to the GB facets only at the center of the grains. For the simplicity in what follows, instead of comparing all the computed and predicted stress components, we compare the resolved shear stress on the active slip system(s). This solution allows a direct comparison with the scalar number. When more than one slip system is activated, all active systems are submitted to the same internal shear stress, owing to the crystal symmetry.

The difference between the predicted (τ_{back}^{pred}) and the computed (τ_{back}^{DD}) back shear stress in the center of the grain is characterized using the relative error:

$$E = |\frac{\tau_{back}^{pred} - \tau_{back}^{DD}}{\tau_{back}^{DD}}| \tag{3.48}$$

When several slip systems are activated inside a grain, the prediction error E is taken as the average of the different errors.

Results of all the simulation we made are reported in Table 3.6. The calculated errors are listed for each dislocation microstructures accumulated at the GBs for the different simulations listed with the same notation as in Figure 3.11 (a to g).

	(a)	(b)	(c)	(d)	(e)	(f)	(g)
E	3%	5%	8%	20%	25%	35%	15%

TABLE 3.6: Relative error between the predicted and computed internal shear stress in the simulation sets of Figure 3.11.

The model predictions are in very good agreement with DD simulation results for the 3 calculations of Set 1, with an error less than 10%. Hence, we can conclude that the model we developed in this chapter is quite efficient in predicting the back stress induced by a uniform and random distributions of surface dislocations. This result is a key result as it confirms that the virtual simple cubic decomposition method we proposed when applied to surface dislocations with the same character (one slip system) and with multiple dislocation characters (different slip systems) is working well. However, when the distribution of dislocations changes from uniform to random, the calculated error increases from 3 to 8%.

This tendency is confirmed with the random distribution of FR sources (Set 2) which promotes heterogeneous distribution of surface dislocations. This heterogeneity is controlled by two factors. The first factor is related to the size of the FR sources. As pointed out by Ohashi *et al.* (Ohashi, Kawamukai, and Zbib, 2007), the first sources

to be activated are those whose length if approximately 1/3 of the grain size, this is why we selected this ratio to define the length of the FR sources used in the present simulations. However, this criteria does not apply on the cube corners, because FR sources in these regions cannot extend to the same area as those located in the middle of the grain. Plastic strain is not easily activated in the grain corners, which prevent dislocation accumulation on the GBs in this regions. This heterogeneity is smoothed up in the model calculations since the surface dislocation density we consider is an average over the total surface of each GB facet. Since, the back stress is computed at the grain center, heterogeneity at the grain corners is expected to make the model prediction of the stress lower than the real value calculated in the DD simulations. The second factor is related to the presence of possible dislocation pile-ups. The use of FR sources in the simulations is known to promote the formation of dislocation pile-ups at the GB. As seen in Figure 3.2b, the distribution of the dislocation density at the GBs is actually not a Dirac function; a fast but smooth decrease is systematically observed in such simulations. An intermediate region between the GB surface and the bulk dislocations can be distinguished. It is precisely the region of dislocation pile-ups shown in Figure 3.12. According to the assumption we made in this section, dislocations in this intermediate region are considered as surface dislocations in the model calculations. Again, this feature is expected to underestimate the stress calculated in the model. This is because the smoothing (coarse-graining) procedure used to define the surface singular density tend to lower the dislocation density. Thus, both effects lead to an underestimation of the back stress.

FIGURE 3.12: Simulated thin foil surrounding the GBs, showing dislocation pile-ups against the GBs.

However, it must be noted that the heterogeneity of dislocation distribution is amplified in our simulations. Sine real grains grains are polyhedral, with no sharp corners as those encountered in our cubic grains. On the other hand, the formation of dislocation pile-ups will be inhibited once the Cross-Slip mechanism is activated (Stricker et al., 2016; Rafael Velayarce et al., 2018).

The Set 3 is carried out on simple four-grain aggregate. The dislocations belonging to different slip systems are accumulated on both sides of the GBs between the adjacent grains. The prediction error of the back stress in grains is round 15% (see Table 3.6), which is mostly induced by the heterogeneous distribution of dislocations accumulated at GBs facets. Our model gives a satisfactory prediction of the back stress by taking into account the elastic screening of the GNDs stored at the GBs of aggregates.

3.4 Conclusion

The accumulation of GNDs is localized in the close vicinity of GBs, which can be approximated as a surface singularity of dislocation concentration. To calculate the long-range stress field associated with the surface GNDs, two types of text book analytical solutions are presented. The first is a continuum approach derived from the theory of Field Dislocations Mechanics (FDM). It calculates the stress field associated with infinite walls of dislocations by considering that the curl of elastic distortion field is equal to the surface Nye's tensor. The second is a discrete approach that deals with infinite and finite walls of dislocations. It is mainly based on the analytical solution of the elastic field of infinite straight dislocation. By comparing these analytical solutions, we found that the finite size of the dislocation wall always leads to vanishing stress at long distance from the wall. The walls of screw dislocations generate only an incompatible elastic distortion field and can be fully recovered by integrating the surface Nye's tensor. On the other hand, the compatible elastic distortion field arising from walls of edge dislocations is not taken into account by the existing FDM model.

The two theoretical solutions above are limited to the case of ideal dislocation walls. In order to address the variation of back stress induced by the finite size of dislocation walls (named as facets), we first used DD simulations to model the facets with different characters of dislocations, dimensions and dislocation densities. We showed that the combination of the stress solutions of three basic characters of facets (twist, tilt and epitaxial) allowed the restoration of the long-range stress field associated with any type of GNDs network covering a GB surface. This calculation is based on an empirical approach derived from the theoretical solution of FDM models. In practice, it involved

determining two parameters fitted from the results of DD simulations. The first is an intensity factor F necessary for adjusting the difference of stress amplitude between the FDM solution and the DD results. The second is a shape function $\xi(\hat{x})$ capturing the stress variation profile with the distance from the facet. With such result, a model was proposed to calculate the back stress inside grains as the sum of the contributions of surface GNDs associated with the bounding GB facets.

The model we proposed was tested on several sets of DD simulations made with simple FCC grains. The cases of uniform, random and heterogeneous GNDs distribution in single and multiple slip conditions in periodic grains and aggregates are all considered. The comparison between the back stress computed by DD simulations and the one predicted from our model showed that the accuracy of the model prediction is about 80 % of the computed value. Heterogeneous distribution of GNDs and dislocation pile-ups seem to be the cause of the discrepancy.

The calculation of back stress with our model is validated by DD simulations. Such result implies the possibility to develop a new approach to calculate the long-range stress field in crystal plasticity modeling. It will be much simpler than the alternative strain gradient approaches, as it only requires the calculation of the GND density covering GBs. The latter is obtained from the computation of Nye's tensor at GB region or more simply from a geometrical analysis assuming that the plastic slip activity inside the grains is homogeneous at low strain. This analysis will be developed in the next chapter.

Chapter 4

On the physical origins of the Hall-Petch effect

In the present study which is mostly based on DD simulation investigations, the Hall-Petch size effect we can simulate is restricted to relatively small plastic deformation. In Chapter 2, we have shown that a size effect is reproduced with basic DD simulations using one- and four-grain periodic aggregates. The HP relationship we reproduced was found proportional to $1/\sqrt{d}$. In Chapter 3, an original model was proposed to calculate the back stress associated with GNDs accumulated at the facets of GBs. Based on these results, we can now deepen our understanding of the HP effect by quantifying the internal stress within the grains.

The engineering yield stress is a stress amplitude usually and arbitrarily calculated at 0.2% of strain. At such strain offset, we know that irreversible plastic deformation already occurs and the yield stress is a combination of elastic stress and plastic strengthening. With the help of DD simulations, this complex feature can be quantitatively analyzed in order to model the elementary mechanisms controlling the HP size effect. In particular in this chapter, the long-range stress field induced by the GNDs accumulated at GBs will be studied separately from the short-range stress field associated with the SSDs. Such decomposition between long-range versus short-range stress is, of course, a matter of many debates. Here, in other words, we want to separate internal stress (back stress) effects, from line tension (forest) effects. We will also discuss the influence of dislocation transmission across GBs and of strain localization on the HP effect in coarse-grained industrial materials.

As mentioned in Chapter 1, there are in the literature many debates about the HP effect. For instance, how does the HP constant vary with the plastic strain? Does the HP effect obey to the linear relationship with the square root of the grain size and why? What is the dominant mechanism of the HP effect? The aim of this chapter is to give physically justified responses to answer these questions.

4.1 Introduction

Long time ago, the seminal work of Hall and Petch (Hall, 1951; Petch, 1953) first demonstrated the effect of grain size on mechanical properties in mild steels. An empirical relationship was established between yield stress σ_y and grain size d, which is later known as the Hall-Petch law:

$$\sigma_y = \sigma_0 + K\frac{1}{\sqrt{d}} \tag{4.1}$$

where σ_0 is a reference stress generally called friction stress and K is often named as the HP constant. Since then, a lot of experimental work has been made to investigate the grain size effect in a great span of metals and alloys. Armstrong *et al.* (Armstrong et al., 1962) provides evidence that the HP law is applicable to the entire stress-strain curve for most polycrystalline metals and alloys. However, in some of the reported work, the validity of the HP law in Eq. 4.1 is questioned. For instance, whether the HP constant K varies with the plastic strain. The latter point is a matter of many debates in the literature, some authors claim that K increases (Cordero, Knight, and Schuh, 2016) while the others suggest that K is invariant or slightly decreases with plastic strain (Haddou, 2003; Tsuchida et al., 2008). Another point discussed in many recent paper concerns the dependence of flow stress on the inverse of the square root of the grain size as depicted in Eq. 4.1. Alternative forms have been proposed to provide a better fit of the HP size effects (Bragg, 1942; Baldwin, 1958; Conrad, 1963; Kocks, 1970; Christman, 1993). Also, though discussions are made from time to time on the validity of the HP law, the phenomenon of "*smaller is stronger*" is generally observed in all the polycrystals with grain size at submicron or at the micron scale. Such grain size effect is commonly formulated by a power law equation relating the flow stress to the grain size. Nevertheless, the elementary mechanisms at the origin of such grain size effect are not fully understood so far.

In a recent review (Cordero, Knight, and Schuh, 2016), studies made in the last six decades on the grain size effect in pure metals was rexamined in a systematic manner. From this work, rich experimental data is gathered in order to estimate the unicity of HP parameters. Then, the existing models predicting the empirical HP law was tested. The pile-up model is found to predict successfully the relationship of Eq. 4.1 but it suffers from lack of experimental evidence to support the relation between dislocation pile-up length and grain size. In addition, the sensitivity of the HP constant K to GB structure and chemistry is not accounted for in the pile-up model. According to Cordero *et al.*, the work hardening model based on the Ashyby's theory of grain size strengthening is the most consistent model since it predicts the increase of HP constant K with plastic strain. However, the authors mentioned that the increasing rate of K measured

experimentally did not follow the model's prediction.

Recently, the validity of the HP law in Eq. 4.1 has been challenged in the following works (Dunstan and Bushby, 2014; Li, Bushby, and Dunstan, 2016; Li, Bushby, and Dunstan, 2018). The authors assembled a wide range of experimental data to revise the Hall-Petch relationship in metals and alloys. In order to avoid the risk of selection bias, the search for experimental data was carried out without preference. Statistic methods were applied to analyze the dependence of mechanical strength on grain size. The authors point out that Eq. 4.1 is not supported by experimental data and they state: "*the long-held HP relationship is not the correct description of grain size strengthening in metals*". On the contrary, the grain size strengthening is in better agreement with $1/d$ or $\ln(d)/d$. According to the authors, such result implies grain size effect is dominated by the length of the Frank-Read sources. The critical stress is inversely proportional to dislocation curvature and the latter is limited by grain size. In addition, in a very recent paper (Li, Bushby, and Dunstan, 2018), the HP constant K shows no sensitivity to plastic strain but only strongly depends on grain size.

Besides experimental means, numerical simulations are often used to investigate the physical origin of grain size strengthening. The 3D-DD simulations provide a detailed description of dislocation arrangement and interactions in the vicinity of the GBs of small grains. The collective behavior of dislocations in bulk materials is well taken into account to reproduce physically justified mechanical properties. An important strength of such simulations is the possibility to investigate the sensitivity of the model results to different parameters. Here, we mainly comment on the work of El-Awady (El-Awady, 2015), in which the size effect measured on micropillars is reproduced with DD simulations on submicron and micron crystals. These results have been extrapolated, using questionable assumptions, to explain the HP effect. Here, a large set of DD simulations was performed by spanning 5 orders of magnitude of dislocation density. The initial dislocation network was introduced as a random distribution of single-end, double-end, surface-surface dislocations, or pinning-free circular and dipolar loops. The results of the simulations exhibit a strong correlation between the micropillar strength and dislocation density. Moreover, for a given crystal size, a critical strength is identified. This stress defines a transition between two strengthening regimes controlled by either the dislocation density or the length of dislocation sources. In addition, both critical strength and its corresponding critical dislocation density are found size dependent. Based on such results, a generalized Taylor strengthening model for small micropillars was established:

$$\tau = \mu \left(\frac{\beta}{d\sqrt{\rho}} + \alpha b \sqrt{\rho} \right) \tag{4.2}$$

where β and α are dimensionless constants. Predictions of this model are in good agreement with some experimental data reported on micropillars. The success of this model when applied to crystals with small dimensions suggests that the grain size effect is dominated by a characteristic length. This characteristic length is the shorter one between the source length (which is proportional to the crystal size) and the mean slip distance of dislocations (which is proportional to the inverse of the square of dislocation density). However, two main drawbacks arise when we try to extend Eq. 4.2 to predict the grain size effect in polycrystals. A first drawback is that considering the initial dislocation density to be proportional to the inverse of grain size $\rho \sim d^{-1}$ is a very strong assumption, especially for industrial alloys. For example, the correlation between initial dislocation density and lath thickness could be measured recently by X-ray diffraction in bainitic steels (He et al., 2017). The initial dislocation density is found to be inversely proportional to the square root of lath thickness in both low-carbon and high-carbon bainitic steels. Such relationship of grain size dependence also holds true in ferritic steels having equiaxed morphology (He et al., 2018). In another work, a relationship between dislocation density and grain size as $\rho \sim d^{-0.6}$ was measured in austenitic stainless steels processed by warm rolling (Yanushkevich et al., 2017). A second drawback of the model is that the enhanced accumulation of dislocations due to the presence of GBs in polycrystals is not taken into account. A significant concentration of dislocations close to GBs leads to a heterogeneous arrangement of dislocations inside grains (He, Ma, and Pantleon, 2008; Ohashi et al., 2009; Caballero et al., 2011; Wang et al., 2011; He et al., 2018). The majority of the dislocations accumulated at GB are polarized (GNDs) and must give rise to long-range stress that strengthens the materials (Daveau, 2012). The effect of such GB strengthening induced by GNDs is not incorporated in Eq. 4.2.

The rest of this chapter is organized as follows. First, we will show in Section 4.2, the prediction of stress-strain curve for a model simulation by considering the full internal stress field. Next, in Section 4.3, we will present two sets of DD simulations that allows us to quantitatively study the HP effect. Then, discussions will be made on the results of DD simulations to progressively unravel the physical origins of the HP effect. The main results of this chapter will be summarized in Section 4.4.

4.2 About plastic strain hardening

In the previous chapter, DD simulations were performed with a grain embedded in an infinite elastic matrix. Tensile loading was applied to deform this grain up to 0.2% of plastic strain and we analyzed the mechanical state of the grain at this deformation. The average distribution of the dislocation density (at 0.2%) calculated from the GBs

to the center area of the grain is plotted in Figure 3.2b. This plot highlights that the majority of the stored dislocations during deformation is accumulated in the close vicinity of the GBs. In addition, the evolution of the Nye tensor $\underset{\sim}{\boldsymbol{\alpha}}$ within the grain was calculated at 0.2% from data post-processing. The result of this calculation is given in Figure 4.1. The average distribution of the Nye tensor component α_{xx} calculated within slices of 50 nm thick normal to the GBs is plotted using the same geometry as in Figure 3.2b, i.e. from the GBs to the grain center. From this curve we see that the variation of the Nye tensor present strong similitudes with the profile of the dislocation density. The magnitude of α_{xx} (like other Nye tensor components) abruptly decreases and goes to zero once getting away from the GB. This profile shows that the concentration of dislocation density accumulated close to the GBs is mostly composed of GNDs while the much lower density of dislocations found in the grain bulk is made of SSDs. The magnitude of α_{xx} goes to zero at a distance around 0.2 μm from the GBs. From this result and other analysis we made for different simulation geometry, we concluded that, at strain lower or equal to 0.2%, the GND density, which is accumulated within the grains, is most exclusively stored in a region of 0.2 μm thick close to the GBs. Here it must be noted that the thickness of this GNDs region we found with the DD simulations is in good agreement with some experimental results. For instance, highly polarized dislocation density was recently observed by TEM in a 0.18 μm thick area close to the lath boundaries in bainitic steels at yield (He et al., 2018).

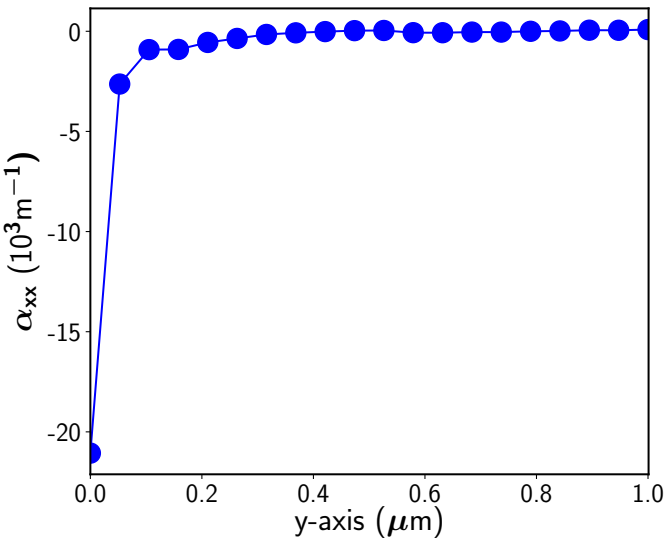

FIGURE 4.1: Calculation of the average distribution of the Nye's tensor component α_{xx} as a function of the distance to the GBs. This calculation is made starting from the GBs and in a direction normal to the GBs surface. The Nye's tensor is calculated within slices 0.05 μm thick.

At this point, we see that two regions inside the grains must be differentiated. One, close to the GBs contains a large density of dislocation most exclusively made of GNDs. The rest of the grain contains a much lower dislocation density essentially made of SSDs. Hence, during DD simulations, we can easily calculate the evolution of both SSDs and GNDs densities by monitoring two different regions. Such information can then be used to make a prediction of the internal stress evolution inside the grain. First, the short-range stress τ_{SSD} associated with forest dislocations can be calculated with the Taylor equation. Second, the long-range back stress τ_{GND} can be calculated inside the grain from the surface density of GNDs accumulated at the GBs and using the model developed in the previous chapter. At last, the flow stress inside the grain is possibly defined by assuming that the contributions of τ_{SSD} and τ_{GND} are simply superposed. The validation of this last proposition is required and can be made by comparing $(\tau_{SSD} + \tau_{GND})$ with the stress-strain curve we compute directly from DD simulation.

The latter stress-strain curve is plotted with a blue solid line in Figure 4.2. The green area corresponds to the short-range stress τ_{SSD} calculated from the SSD density measured at the center of the grain. τ_{SSD} is almost constant with strain because the SSD density did not evolve significantly during 0.2% of plastic strain. Following the same procedure as the one used in the previous chapter to calculate τ_{GND} at 0.2%, the evolution of τ_{GND} at the grain center was calculated at increasing plastic strain offsets, i.e. 0.05%, 0.1% and 0.15%. This evolution of τ_{GND} with strain is plotted with a yellow area in Figure 4.2. The rapid increase of τ_{GND} we observe is directly associated to the rapid accumulation of GNDs at GBs with plastic strain. The calculations we made to draw the Figure 4.2 clearly show that the addition of τ_{SSD} and τ_{GND} gives a good prediction of the stress-strain curve. Indeed, our prediction that correspond to the superposition of the green and the yellow areas is only a few percents smaller than the stress-strain curve calculated with the DD simulations. The discrepancy observed here for the back stress calculation is mostly due to the artifacts we discussed in Chapter 3. It must be noted also that the contribution of τ_{GND} to the flow stress of a plastic grain embedded in an elastic continuum is about 80% and is responsible for most of the strain hardening. In other words, our calculations show that at low plastic strain, the strengthening effect in a confined grain mainly arises from the back stress generated by the GND density accumulated at GBs.

The major contribution of τ_{GND} to the strain hardening we show with the Figure 4.2 proves that strain hardening models used for polycrystalline materials should consider the contribution of the GND density separately from the forest hardening mechanisms. This important point is in contradiction with many existing crystal plasticity models like (Cheong and Busso, 2004; Cheong, Busso, and Arsenlis, 2005; Pipard et al., 2009),

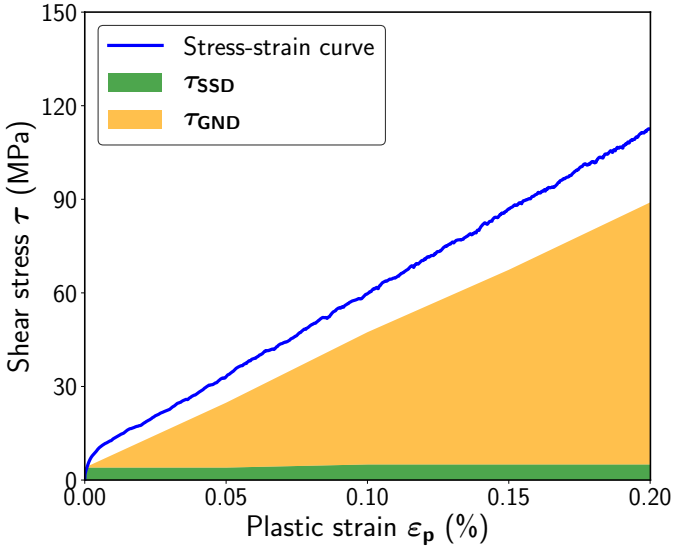

FIGURE 4.2: Prediction of stress-strain curve calculated by adding the stress contributions of SSDs and GNDs. The stress-strain curve in blue is the direct outcome of the DD simulation. τ_{SSD} in green is the short-range internal stress associated with SSD density calculated in central area of grain from the Taylor equation. τ_{GND} in orange is the back stress calculated using the calculation of the average GND density accumulated in the close vicinity of GBs (dislocation lines at distance smaller than 0.4 μm from a GB).

where the SSDs and GNDs densities are defined separately, but their contribution to strain hardening is accounted by adding both density into the Kocks-Mecking and the Taylor equations. This type of solution underestimates the flow stress because the back stress associated with the presence of GNDs at the GBs is not explicitly taken into account. Providing a better and numerically efficient solution for the modeling of strain hardening in polycrystals is the main goal of the coming sections.

The test case of a grain embedded inside an elastic matrix we analyzed in this section is far from the real polycrystals case, but still it reveals an essential feature of the strengthening of polycrystalline materials. The stress-strain curve of each grain can be predicted with dislocation density based models. In addition, we realize that the flow stress prediction requires independent calculations of short- and long-range stress contributions. In the next section, the same type of test case is carried out with different grain sizes in order to better understand the HP effect.

4.3 Modeling the Hall-Petch size effect

4.3.1 DD Simulations

In Chapter 2, we have shown that the HP effect can be reproduced from DD simulations with periodic aggregates made of one or four grains. In this chapter, even simpler configurations made of one cubic grain embedded in an elastic matrix is used to identify the details of the mechanisms controlling the HP effect. Although such simple simulations are not representative of the plasticity of real polycrystalline aggregate, they bring out the most important features controlling the strengthening effect associated with the grain size reduction.

Two different sets of DD simulations have been carried out. We first present the elements common to all the simulations. Four different sizes of grains have been tested between 1.25 μm and 10 μm. The GBs are considered as impenetrable interfaces to the motion of dislocations. A tensile stress is applied along the [100] direction of the simulated grain. Whatever the grain size, the initial dislocation microstructure is made of a random distribution of screw FR sources belonging to the eight active slip systems. The source length L is a third of the grain size d. For all the simulated grains, the number of initial FR sources per slip system is constant and equals 168 (21 on each slip system). Thus, the initial dislocation density varies with the simulated grain sizes. The initial dislocation density used for each grain size is summarized in Table 4.1. Finally, the cross-slip mechanism is activated during the simulations and the grains are deformed within quasi-static regime using constante strain rate identical to the one used in the simulations of Chapter 2.

Grain size d(μm)	1.25	2.5	5	10
FR source length L(μm)	0.375	0.75	1.5	3
Initial dislocation density $\rho_{ini}(10^{12}m^{-2})$	32	8	2	0.5

TABLE 4.1: Parameters defining the initial dislocation microstructure used in the simulations with different grain sizes.

The difference between the two sets of simulations analyzed in this section is related to the boundary conditions we applied to the simulations. The first set corresponds to simulations with one grain embedded in an infinite elastic matrix. The second set corresponds to simulations with periodic boundary conditions (PBC) applied to the limits of the simulated grain. The latter solution is equivalent to simulate an infinite periodic aggregate made with one cubic grain. In Figure 4.3, the evolution of the flow stress (a) and the dislocation density (b) as a function of the plastic strain is reproduced for the two sets of simulations. Solid lines are used for the grain embedded in an elastic

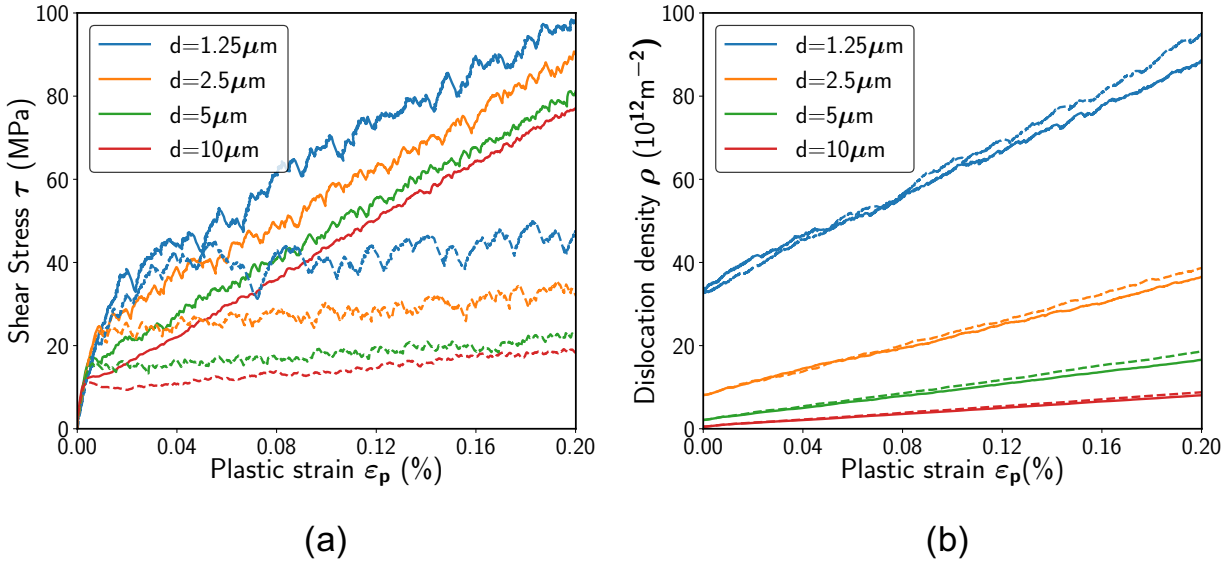

FIGURE 4.3: (a) Stress-strain curves and (b) evolution of the dislocation density with plastic strain. Solid lines are used for the simulation with a grain embedded in an elastic matrix and dashed lines are used for the periodic grain simulations (see the text for more details regarding the simulation conditions). Different colors are used for the different grain sizes tested.

matrix and dashed lines are used for the periodic grain. As expected, we see that the flow stress increased when the grain size decreased for both sets of simulations. A grain size effect is then successfully reproduced with both types of simulations.

4.3.2 Independence of the back stress with grain size

Looking at Figure 4.3a, we see that for the two sets of simulations carried out in this section, a grain size effect is found, i.e. the flow stress increases when the grain size decreases. Another important point to notice is that the strain-stress curves are parallel when changing the grain size for each set of simulations. This behavior looks surprising, but is quite similar to experimental stress-strain curves found in 316L steels (Haddou, 2003) and bainitic steels (He et al., 2018) at low strain. It means that a constant strain hardening rate is observed after the yield point whatever the grain size. In addition, the work hardening rate calculated with the two different sets of simulation is found to be very different. A much larger hardening rate is found in the simulations with an embedded grain.

Surprisingly, these results cannot be simply linked to the variation of the dislocation density inside the grains. As shown in Figure 4.3b, for the two sets of simulations, the dislocation density is found to increase faster when the size of the grain is reduced. Here, we must also notice that the dislocation density rate of accumulation with plastic strain

is very poorly dependent on the boundary conditions, i.e. same results are found for the two sets of simulations. Then, comparison of Figure 4.3a and Figure 4.3b confirms that it is not possible to predict plastic strain hardening in a grain with only the Taylor equation since the latter directly links strengthening to the total dislocation density. Rather we observe here that the strain hardening rate is independent of grain size and the storage rate of dislocation density varies significantly with grain size. Giving an explanation to this behavior is the key point of this chapter.

To elucidate this point, we recall the main steps in calculating back stress from the surface GND density developed in the previous chapter. First, a surface Nye's tensor $\underset{\sim}{\boldsymbol{\alpha}}_{\boldsymbol{s}}$ was defined as:

$$\underset{\sim}{\boldsymbol{\alpha}}_{\boldsymbol{s}} = \frac{1}{S}\sum_{j}^{n} \underline{\boldsymbol{b_i}} \bigotimes \underline{\boldsymbol{L_j}} = \frac{\sum_j^n L_j}{S} \underline{\boldsymbol{b_i}} \bigotimes \underline{\boldsymbol{l_j}} \tag{4.3}$$

where $\underline{\boldsymbol{b_i}} \bigotimes \underline{\boldsymbol{l_j}}$ is a tensor defined for each slip system and S is the surface area of a GB facet. Then, the surface GND density ρ_s is a scalar and is calculated as the total length of dislocation line divided by the surface area of the GB facet:

$$\rho_s = \frac{\sum_j^n L_j}{S} \tag{4.4}$$

Once $\underset{\sim}{\boldsymbol{\alpha}}_{\boldsymbol{s}}$ is calculated, the expression of the elastic distortion tensor $\underset{\sim}{\boldsymbol{U}}_{\boldsymbol{e}}$ can be obtained by integrating equation $\underset{\sim}{\boldsymbol{\alpha}} \simeq curl \underset{\sim}{\boldsymbol{U}}_{\boldsymbol{e}}$ with the hypothesis of Dirac delta distribution of the surface density of GNDs across the GB facet. At this step, no characteristic dimension of the grain size is considered, therefore $\underset{\sim}{\boldsymbol{U}}_{\boldsymbol{e}}$ is proportional to $\underset{\sim}{\boldsymbol{\alpha}}_{\boldsymbol{s}}$ and further to ρ_s. The following step is to calculate the FDM theoretical stress tensor $\underset{\sim}{\boldsymbol{\sigma}}_{FDM}$ with the Hooke law assuming isotropic elasticity for simplicity, no characteristic dimension of the grain size is involved neither. Finally, associating the stress intensity factor F and the shape function $\xi(\hat{x})$ with the theoretical stress tensor allows to determine the variation of the stress tensor $\underset{\sim}{\boldsymbol{\sigma}}_{GND}$ associated to the GNDs stored at GB facet. The back stress τ_{GND} is simply the projection of $\underset{\sim}{\boldsymbol{\sigma}}_{GND}$ onto the glide plane of a considered slip system. It must be noted here again that the pre-factor F is a simple coefficient and the shape function $\xi(\hat{x})$ is a normalized distribution curve, both of them are dimensionless. In summary, the outline of the back stress calculation is:

$$\rho_s \Rightarrow \underset{\sim}{\boldsymbol{\alpha}}_{\boldsymbol{s}} \Rightarrow \underset{\sim}{\boldsymbol{U}}_{\boldsymbol{e}} \Rightarrow \underset{\sim}{\boldsymbol{\sigma}}_{FDM} \Rightarrow \underset{\sim}{\boldsymbol{\sigma}}_{GND} \Rightarrow \tau_{GND} \tag{4.5}$$

From this we can deduce that:

$$\tau_{GND} \propto \rho_s \tag{4.6}$$

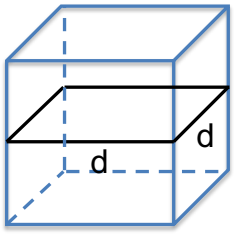

FIGURE 4.4: A dislocation loop is deposited at the GBs of a cubic grain of size d.

From a qualitative point of view, Eq. 4.6 indicates that the back stress τ_{GND} inside a grain is simply proportional to the surface GND density ρ_s. Here, one needs to pay attention that in Eq. 4.6 the surface GND density ρ_s is of dimension m^{-1} that differs from the conventional dislocation density ρ of dimension m^{-2} defined in a volume.

In order to validate Eq. 4.6 from the DD simulation results, the surface GND density ρ_s must be defined and its evolution with plastic strain needs to be clarified. The latter point is explained with a simple geometrical model.

Imagine a cubic grain of linear size d with a dislocation loop accumulated at its GBs (see Figure 4.4). The augmentation of surface dislocation density is by definition:

$$\mathrm{d}\rho_s = \frac{4d}{d^2} \tag{4.7}$$

and the shear strain made by the expansion of the dislocation loop is:

$$\mathrm{d}\gamma = \frac{bd^2}{d^3} \tag{4.8}$$

So the storage rate of surface dislocation density is:

$$\frac{\mathrm{d}\rho_s}{\mathrm{d}\gamma} = \frac{4}{b} \tag{4.9}$$

From this simple geometrical analysis, we see that the storage rate of surface dislocation density is a constant. Unlike the conventional storage rate of dislocation density in a volume $\mathrm{d}\rho/\mathrm{d}\gamma = 4/bd$ that is inversely proportional to the grain size d, the storage rate of surface dislocations density $\mathrm{d}\rho_s/\mathrm{d}\gamma = 4/b$ is found to be independent of the grain size d.

Now we want to validate the relationship given in Eq. 4.9. The term $d\rho/d\gamma$ in Eq. 4.10 is recorded in DD simulations and the grain size d is known as well, so $d\rho_s/d\gamma$ can be deduced from $d\rho/d\gamma$ with a simple geometrical relationship:

$$\frac{\mathrm{d}\rho_s}{\mathrm{d}\gamma} = \frac{\mathrm{d}\rho}{\mathrm{d}\gamma} \times d \tag{4.10}$$

In the DD simulations, the recorded dislocation density is computed from the sum of the dislocation lines accumulated within a given volume during the deformation. Previously, we pointed out two important remarks on the organization of dislocations inside the grains. First, at low strain, the dislocation density distributed in the central volume of a grain is made of SSDs and the latter density hardly increases before 0.2%. Hence the SSD density is close to the initial dislocation density ρ_{ini} given in Table 4.1. Second, most of the dislocations multiplied during the deformation are accumulated in the close vicinity of GBs and those dislocations are only GNDs in the case of an embedded grain. From these two remarks, we can calculate the evolution of surface dislocation density from the total dislocation density variations reported in Figure 4.3b. First, we subtract the initial dislocation density to define the GND dislocation density produced during the deformation. Then, with the help of Eq. 4.10, the storage rate of dislocations defined within a fixed volume can be converted into a storage rate of surface dislocations defined within a surface area. In the case of the embedded grain simulations, the obtained surface dislocation density is plotted as a function of the plastic strain and for different grain size in Figure 4.5. From this figure, it is clear that the previous curves drawn in Figure 4.3b collapse now into a single straight line. Hence, in agreement with Eq. 4.9, we confirm that the storage rate of surface dislocation density is a constant value, independent of the grain size and its exact value accounting for the geometry of grains can be measured from DD simulations. In the case of cubic grain, the solution we identified with Figure 4.5 is:

$$\frac{\mathrm{d}\rho_s^{\mathrm{DD}}}{\mathrm{d}\varepsilon_p} = \frac{9.3}{b} \tag{4.11}$$

In the set of simulation we analyze, the Schmid factor is $m = 0.408$ since the grain is loaded in the [100] direction, the measured storage rate of surface dislocation in Eq. 4.11 can then be expressed as:

$$\frac{\mathrm{d}\rho_s^{\mathrm{DD}}}{\mathrm{d}(\varepsilon_p/m)} = \frac{\mathrm{d}\rho_s^{\mathrm{DD}}}{\mathrm{d}\gamma} = \frac{3.8}{b} \tag{4.12}$$

The solution, Eq. 4.12, we calculated with the DD simulations is consistent with the theoretical value given in Eq. 4.9. The latter geometrical analysis works well and it confirms again that most of the dislocations multiplied during the plastic deformation are accumulated in the close vicinity of GBs.

Now from the above analysis, the puzzling phenomenon of the insensitivity of the

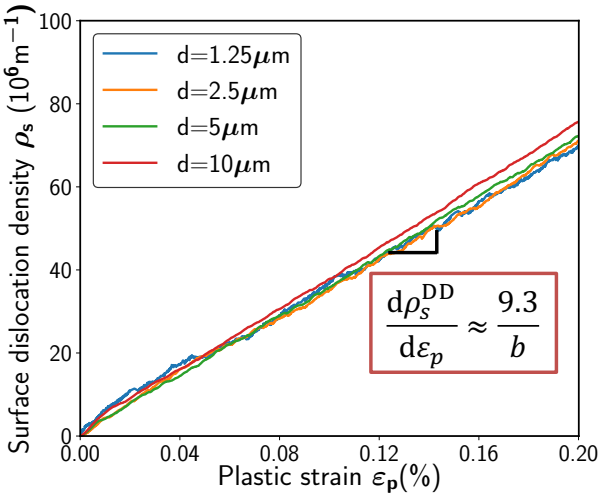

FIGURE 4.5: The increase of surface dislocation density ρ_s is illustrated as a function of the plastic strain ε_p. In the simulated grains of different sizes, the storage rate of surface dislocation density is a constant and its value is directly measured.

back stress on the grain size is readily explained. The back stress is generated by GNDs accumulated on the surfaces of GBs. When modeling the back stress from GND density, the true dependence is found between the back stress and a specific quantity, the surface GND density. The latter quantity increases linearly with plastic strain at a constant rate regardless of the grain size. Therefore, the increase of back stress is not dependent on grain size. Whatever the grain region we monitor τ_{GND}, the latter quantity evolution with plastic strain is independent of the grain size. Finally, an ultimate linear relationship can be proposed between the back stress and the plastic strain:

$$\tau_{GND} \propto \varepsilon_p \tag{4.13}$$

The above relation is general and is verified in all the simulations we proceeded. For instance, in Figure 4.3a, all the stress-strain curves we simulated with two different sets of boundary conditions confirm a linear increase of τ_{GND} with ε_p. Thanks to these DD simulations, the quantification of the back stress inside aggregates with few grains was successfully achieved. The linear relationship found between the back stress and the plastic strain in Eq. 4.13 allows proposing new constitutive equations to model grain size effect in crystal plasticity simulations. Due to lack of time, such work could not be made during this PhD. Nevertheless, an attempt of such effort based on the classic Kocks-Mecking formulation is presented in Appendix B. This modified Kocks-Mecking model accounts for most of the results obtained during the PhD. Unfortunately, it was not possible to test numerically the validity of this model with FEM calculations before the end of my PhD.

A last point to discuss in this section is the origin of the different strain hardening rate we calculated when passing from the simulations of an embedded grain to a periodic grain. In Figure 4.3a, the beginning of the stress-strain curves looks very similar when we compare the simulations with the same grain size, but different boundary conditions. After yield, changing the type of boundary conditions change a lot the strain hardening rates. The strain hardening rate of the simulations with PBC is found much lower, suggesting the absence of a back stress effect. This change of mechanical behavior can be explain by a decrease of the surface GND density. Indeed, due to the use of PBC, GND density with opposite signs are now accumulated on both sides of the GBs. As a result, the surface GND density is significantly reduced (ideally should be zero in the case of homogeneous distribution) and the stress field τ_{GND} is mostly annihilated. Thus, the density of dislocations accumulated in the vicinity of the grain gives almost no strengthening effect in the periodic grain case. On the other hand, it is interesting to note that the quantity of dislocation accumulated at GBs and inside the grain is not modified when we change the boundary conditions, see Figure 4.3b. This justifies that, the multiplication of dislocations is controlled by the strain rate we imposed and is very weakly affected by the existence of a back stress. A more detailed analysis of the strain hardening behavior in the grain simulated with PBC is presented in Appendix C.

So far, we demonstrated that in DD simulations, the evolution of the back stress is independent of the grain size and therefore the existence and the amplitude of a back stress cannot contribute to the HP size effect. Thus, one can assume that the manifestation of a grain size effect in the DD simulations is associated to an additional mechanism controlling the plastic properties of the simulated grain in the early stage of the deformation. In order to investigate this point, the influence of the initial dislocation microstructure is analyzed in the next section.

4.3.3 Influence of the initial dislocation microstructure

When examining the stress-strain curves at low strain in Figure 4.3, the flow stress appears to be different at the beginning of the plastic stage each time we change the grain size. This implies that the initial dislocation microstructure, which controls the flow stress before the apparition of a back stress, could be the key point giving rise to the simulated size effect. We now focus on studying the influence of the initial simulation conditions on the CRSS at yield.

Based on the results of previous DD simulations (see for instance (Ohashi, Kawamukai, and Zbib, 2007)), we know that the lowest critical stress for the activation of Frank-Read sources of different lengths corresponds to the sources of length close to

one third of the grain size. Previous studies have shown that such solution eliminates important simulation artifacts. Example of such artifact is an artificial increase of the CRSS amplitude when too small FR sources are used. This is why in the present study, the initial length of FR sources was fixed to 1/3 of grain size. On the other hand, being limited by computing time, it was not possible to investigate a wide range of grain sizes starting with the same dislocation density. This is why we decided to insert the same number of FR sources independently of the grain size. As a result, the initial dislocation density evolves with the grain size (see Table 4.1).

Pure copper was used as test case material with a dry lattice friction τ_0 fixed to 2.5 MPa. Such small lattice friction is expected in the case of relatively pure copper. The initial dislocation density considered inside the grains is included between the order from 10^{11} to $10^{13} m^{-2}$. Two different strengthening mechanisms can possibly control the slip system CRSS (El-Awady, 2015).

The first is commonly called the source control mechanism. A critical stress is required to bow out dislocation sources to a critical state where the multiplication of dislocation lines and irreversible plastic deformation is triggered. Such critical stress is determined by the length of the dislocation sources. In the case of FR sources, this critical stress can be calculated with the help of the Foreman equation (Foreman, 1967):

$$\tau_F = A \frac{\mu b}{2\pi} \frac{1}{L} \left[\ln \left(\frac{L}{r_0} \right) + B \right] \tag{4.14}$$

For screw dislocations $A = 1.5$; for edge dislocations $A = 1$. In the case of FR sources with finite pinning points, B is commonly considered as 0. The core radius of dislocation r_0 is considered as the same order of b. The length of FR source is assigned by L.

The second mechanism is the well-known forest mechanism which is related to the line tension restricting the mobility of dislocation pinned by junctions in a dislocations network. The strength of the dislocation network is mainly controlled by the dislocation density and can be calculated with the help of the Taylor or forest equation (Saada, 1960; Devincre, Kubin, and Hoc, 2006):

$$\tau_T = \alpha\mu b\sqrt{\rho_{ini}}$$
$$\text{with} \qquad \alpha = \frac{\ln\left(\frac{1}{\alpha_{ref} b\sqrt{\rho_{ini}}}\right)}{\ln\left(\frac{1}{\alpha_{ref} b\sqrt{\rho_{ref}}}\right)}\alpha_{ref} \tag{4.15}$$

In Taylor equation, the reference interaction strength coefficient is $\alpha_{ref} = 0.4$ and the reference dislocation density is $\rho_{ref} = 10^{12} m^{-2}$. The initial dislocation density is assigned by ρ_{ini}.

In our simulations, we fixed the proportionality between the grain size d and the FR source length L as:

$$d \simeq 3L \tag{4.16}$$

The number of initial FR sources is the same in all the simulated grain size and $n = 168$. Then, the initial dislocation density ρ_{ini} takes the form:

$$\rho_{ini} = \frac{nL}{d^3} = \frac{n}{27L^2} \tag{4.17}$$

The analytical solutions given by equations 4.14 and 4.15 can be both written as a function of the FR source length L. In Figure 4.6, the analytical solutions calculated from the Foreman equation 4.14 and from the Taylor equation 4.15 are displayed as functions of L with a green curve and a red curve, respectively. In addition, the computed CRSS τ^{DD}_{CRSS} taken from Figure 4.3 are also reported in Figure 4.6 with blue symbols. It can be seen that the amplitude of the simulated τ^{DD}_{CRSS} (blue dots) are systematically found higher than the Taylor equation predictions. Rather the simulation results are in better agreement with the prediction of the Foreman equation (green curve). Hence, we can conclude that the mechanism controlling the CRSS in our simulations is mainly the source multiplication process rather than the forest mechanism. However, we note that the simulation results are less and less in agreement with the Foreman equation and are in better agreement with the prediction of the forest equation when the source length is reduced, i.e. the grain size is decreased.

How can we explain that the CRSS at the beginning of the simulation is controlled by the multiplication process rather than the forest interaction? A simple explanation comes from the rule we adopted to build the initial dislocation microstructure in the simulated grains. Indeed, for each grain size we considered, the dislocation density we simulate is essentially the lowest dislocation density that can be incorporated in the grain when using FR sources. Then, at the very beginning of the plastic deformation, a

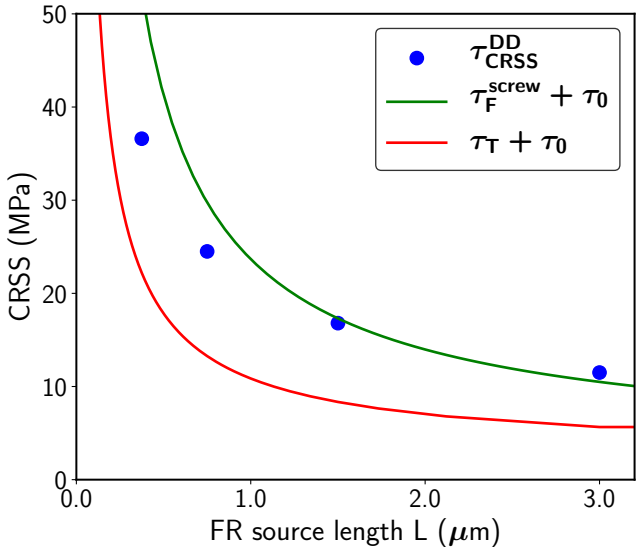

FIGURE 4.6: Variation of the CRSS as a function of FR source length L. The simulated CRSS τ_{CRSS}^{DD} are marked with blue symbols. The analytical solutions calculated from the Foreman equation and the Taylor equation are shown with green and red lines, respectively. A dry friction τ_0 of 2.5 MPa is taken into account.

network of tangled dislocations is not formed. Therefore, the plastic yield is controlled by the first dislocation loop emitted from a FR source. Looking at the simulation films, it is clear that the first dislocation loops are expanded and reach the GBs without being entangled by many forest dislocation segments. In order to build up a 3D dislocation microstructure controlled by the forest mechanism, the initial dislocation density must be increased and the source length L should be about three times longer than $1/\sqrt{\rho_{ini}}$ (Devincre, Kubin, and Hoc, 2006). In our simulations, the length of the FR sources L is initially about twice $1/\sqrt{\rho_{ini}}$, this is why the CRSS at yield is controlled by the source multiplication. In Appendix D, we give an example of a simulation made with a much larger initial dislocation density to prove the latter conclusion.

From the above analysis, we conclude that the CRSS at yield is controlled by the dislocation source length and therefore is grain size dependent. Rapidly, after yield, many dislocation loops are produced by the sources and are accumulated at the GBs to generate a back stress. The latter increases linearly with plastic strain. The evolution of the back stress is then independent of the grain size and does not control the size effect. This is why we conclude that the properties of the initial dislocation microstructure control the CRSSs at the beginning of the plastic deformation and therefore is the material feature we must consider to deeply investigate the HP effect.

There is still a lot of debate in the literature about the dependence form of the

strength of polycrystals with the grain size. Overall, three main relationships are reported; flow stress is proportional to $1/\sqrt{d}$, $1/d$ or $\ln(d/b)/d$. In what follows, the results of our simulation are tested to find the best relation between flow stress and grain size. This test is reproduced in Figure 4.7 at (a) 0.1% and (b) 0.2% of plastic strain. As expected, the two tests give the same results, since the plastic strain hardening does not affect the size effect. The flow stress $\tau_{0.1}$ and $\tau_{0.2}$ of embedded grains of different sizes are taken from the stress-strain curves in Figure 4.3. Those quantities are plotted in Figure 4.7 as a function of $1/\sqrt{d}$, $1/d$ and $\ln(d/b)/d$ respectively. The best fit is obtained with the $1/\sqrt{d}$ formulation, which is in agreement with the most classical forms of the HP law. Here, it must be mentioned that the range of grain size we explore with the simulation (one to ten micrometers), may be too small to make a definitive conclusion regarding this point.

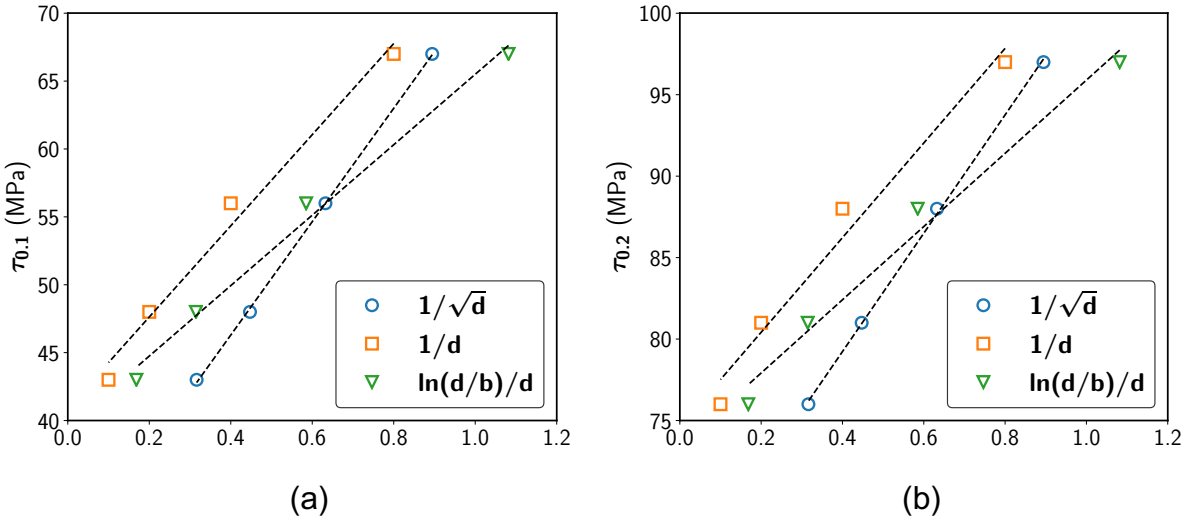

FIGURE 4.7: The flow stress (a) $\tau_{0.1}$ and (b) $\tau_{0.2}$ measured at 0.1% and 0.2% of plastic strain is plotted as a function of $1/\sqrt{d}$, $1/d$ and $\ln(d/b)/d$, respectively.

The flow stress on the stress-strain curve is made of a fixed CRSS τ_{CRSS} defined by the initial dislocation microstructure and a back stress τ_{GND} whose amplitude increases with plastic strain. We argued that τ_{GND} increases with the plastic strain and is strain rate and grain size independent, so a dependency of $1/\sqrt{d}$ type should also be observed on τ_{CRSS}. Earlier in this section, we showed that τ_{CRSS} is controlled by the initial dislocation microstructure. Two mechanisms, the source multiplication mechanism and the forest mechanism have been compared with the simulation results. We now expand this analysis to see if those mechanisms are compatible with a $1/\sqrt{d}$ dependency.

If τ_{CRSS} is controlled by the source multiplication and follows the Foreman equation 4.14, then:

$$\tau_{CRSS} \propto \ln\left(\frac{L}{b}\right)\frac{1}{L} \propto \ln\left(\frac{d}{b}\right)\frac{1}{d} \tag{4.18}$$

If τ_{CRSS} is controlled by the forest mechanism and follows the Taylor equation 4.15, then:

$$\begin{aligned} \rho_{ini} &= \frac{nL}{d^3} \propto \frac{1}{d^2} \\ \alpha &\propto \ln\left(\frac{d}{b}\right) \\ \tau_{CRSS} &\propto \ln\left(\frac{d}{b}\right)\frac{1}{d} \end{aligned} \tag{4.19}$$

Both simple analysis show that if the CRSS is dominated by either the source multiplications or the forest interactions, a linear relationship should always be observed between τ_{CRSS} and $\ln(d/b)(1/d)$. However, we see that the computed CRSS plotted in Figure 4.7 is more likely to be proportional to $1/\sqrt{d}$. In order to understand the origin of such contradiction, a detail analysis of the dislocation dynamics was made at different grain size. Essentially, this analysis explains why τ_{CRSS} is progressively smaller than the Foreman equation when the grain size is reduced.

After analyzing the dynamics of dislocations inside the grain and more specifically the dynamics of the FR sources at very low strain, we found an explanation for this discrepancy between the theoretical prediction and the simulation results. As an effect of the FR source length reduction in the smaller grains, the applied stress must be increased to bow out the dislocation lines. At the same time, more and more relaxation mechanisms are observed inside the grains. Cross-slip, collinear annihilation and line tension effects facilitate the re-arrangement of the dislocation microstructure in the smaller grains. Those rearrangements promote the apparition of longer dislocation line acting as FR sources with a lower critical stress. This is the main cause that gives rise to a lower CRSS computed from simulations than the prediction of the Foreman equation shown in Figure 4.6. An example of this rearrangement of dislocations is illustrated with some details in Appendix E.

Finally, if the CRSS was controlled only by the multiplication of the initial FR sources in the simulation, the size dependent relationship should be proportional to $\ln(d/b)(1/d)$. However, the interference of the stress relaxation effect makes the final size dependent relationship more likely to be proportional to $1/\sqrt{d}$. Here it must be

noted that a similar effect has been reported by El-Awady (El-Awady, 2015) regarding the size effect observed in micro-pillars. The CRSSs calculated in micropillars of decreasing sizes is also found to linearly increase like $1/\sqrt{d}$. In our simulations like in micropillars, the measured CRSS are actually located in a transition stage between the single source strengthening and the forest strengthening regimes. Therefore, the grain size effect should not be regarded as an outcome of one single strengthening mechanism. It is rather the result from a combined effect of multiple mechanisms including relaxation processes in the smaller grains, which, in a coincident way, gives rise to an HP law with a dependence following a relation of type $1/\sqrt{d}$.

We demonstrated, at low strain, that the back stress generated by GNDs accumulated at GBs is independent of the grain size and that the HP effect is controlled by the CRSS associated with the initial microstructure of dislocations. Such results must be reconsidered in the case of coarse-grained industrial materials with a relatively high dislocation density. Indeed, in the latter case, the HP effect might disappear if the initial dislocation microstructure found in the grains becomes independent of the grain size. Often, industrial alloys are elaborated with the same heat treatment and therefore the initial dislocation density is not expected to evolve significantly when changing the grain size. Still, a HP effect is observed in those industrial materials with different grain sizes. Then, we suggest that one additional feature may be missing in our simulations made with relatively small grains. This feature could be the last missing process needed to reproduce the HP effect observed in coarse-grained materials.

4.3.4 Strain localization and dislocation pile-ups effects

The initial dislocation microstructure observed in "real" materials like industrial alloys is much more complex than the random distribution of FR sources we used in the present DD simulation investigation. It is reasonable to expect that the effect of single source strengthening becomes secondary in comparison with forest strengthening and other additional strengthening mechanisms, particularly in coarse-grained materials with high dislocation density. The model we proposed so far is deduced from model DD simulations in the context of pure metals with small grains. Also, some modeling hypothesis has been made for reason of simplicity. For instance, as we restrict the simulations to relatively small strain, GBs are considered as impenetrable obstacles for dislocations and the plastic deformation is assumed homogeneous within the grains. In experiments, coarse-grained materials are usually deformed at low strain with single or two active slip systems and softening effects can promote a rapid localization of plastic strain. Under this circumstance, the formation of dislocation pile-ups in localized regions of the GBs is expected. In addition, we know from many *in situ* observations (see for instance Kacher

et al., 2014) that once the stress concentration at the tip of a dislocation pile-up exceeds a critical value, direct or non-direct transmission of plastic strain at the GB will take place.

If plastic strain transmission at GBs is automatically reproduced in DD simulations with the activation of dislocation sources on both sides of GBs, the property of dislocation transmission from one grain to the next grain is not yet programmed in the *mM* code. The reason is that the detail mechanism of GB transmission observed for instance in atomistic simulations (Spearot and Sangid, 2014) has not yet been generalized into a physically-justified formula accounting at least for the misorientation angle of the GBs. However, as an effect of strain localization and pile-up formation there is little doubt that the influence of dislocation transmission at GBs should not be ignored when modeling the size effect in industrial alloys. Including such property in the model developed in this work can be made with the help of the well-known pile-up model discussed in Chapter 1. In this model, transmission of dislocation at the GBs is assumed to take place when the local stress at the tip of a dislocation pile-up reaches a critical value of GB resistance. In what follows, an analytical study on the combined effect of the initial dislocation microstructure effect and the possible transmission of dislocations at the tip of pile-ups is conducted to propose a more general HP effect model which can be applied to a wide range of materials and grain sizes.

The sizes of the grain, d, we want to explore in the following are in the range:

$$d \in [1, 2, 4, 6, 8, 10, 14, 20, 30, 40, 50, 65, 80, 100](\mu m)$$

For simplicity and to connect with the DD simulations, the initial microstructure of dislocations is considered made of FR sources with an average length $L = d/3$:

$$L \in \frac{1}{3} * [1, 2, 4, 6, 8, 10, 14, 20, 30, 40, 50, 65, 80, 100](\mu m)$$

In order to explore a large range of materials, different amplitudes of initial dislocation density are also explored:

$$\rho_{ini} \in [10^{10}, 10^{11}, 10^{12}, 10^{13}](m^{-2})$$

Following the same analysis that we made when we discussed the DD simulation results, the CRSS on active slip systems is at yield a function of a well defined characteristic length scale. The latter is either the length of the dislocation sources L or the mean distance between forest dislocations that is inversely proportional to $\sqrt{\rho_{ini}}$. Based on those two characteristic lengths, the CRSS is defined either with τ_F given by Eq.

4.14 or τ_T given by Eq. 4.15. The higher solution between τ_F and τ_T defines τ_{CRSS}.

Solution of the τ_{CRSS} calculation following this rule is plotted as a function of the grain size d in Figure 4.8a. The symbols with different colors correspond to different initial dislocation density. As expected, when the dislocation density ρ_{ini} is high, τ_{CRSS} is found to be constant in a wide range of grain sizes. This phenomenon is easy to understand. When the magnitude τ_{CRSS} is controlled by the dislocation density, i.e. in the forest strengthening regime, τ_{CRSS} becomes independent of the size of the grains. Then, the model we proposed in the previous section predicts an absence of HP size effect. From figure 4.8a, it becomes clear also that when reducing the grain size, the length of the dislocation sources L becomes shorter and it controls the early stage of plastic deformation whatever the dislocation density. After entering this regime, τ_{CRSS} starts to increases when decreasing the grain size d.

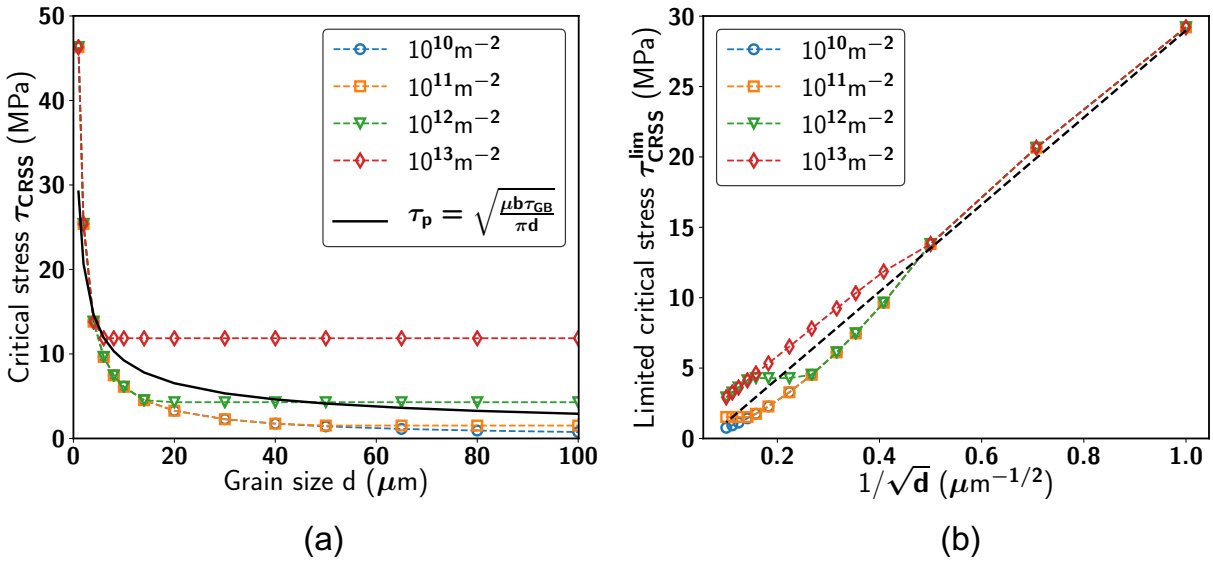

FIGURE 4.8: (a) Analytical solutions of τ_{CRSS} of different initial dislocation density is plotted as a function of grain size d with symbols in color. The length of dislocation source is considered as $L = \frac{1}{3}d$. The amplitude of τ_{CRSS} is defined by the higher stress between τ_F and τ_T. The black curve is the analytical solution of back stress τ_p generated by the dislocations in pile-up as a function of grain size d. The critical stress of the GB transmission is considered as $\tau_{GB} = 250$ MPa. (b) Limited critical stress τ^{lim}_{CRSS} is deduced from solutions of τ_{CRSS} for different initial dislocation density shown in (a) with one condition: if the value of τ_{CRSS} is greater than τ_p, we keep the latter as τ^{lim}_{CRSS}. Limited critical stress τ^{lim}_{CRSS} is plotted as a function of $1/\sqrt{d}$. A linear fitting between τ^{lim}_{CRSS} and $1/\sqrt{d}$ is shown in black dashed line.

The curves plotted in Figure 4.8 predict the absence of a grain size effect in large

grains with a high dislocation density. Such prediction is consistent with our DD simulation results, but is contradictory with experimental investigations made with coarse-grained metals and alloys (Shan Le Wang and Murr, 1980; Meyers, Andrade, and Chokshi, 1995; Armstrong, 2014). For this reason, the predictions of those calculations are now compared with the prediction of the pile-up model. Indeed, this model, which is based on the mechanism of dislocation transmission at GBs, looks pertinent in the case of coarse grains with a localized plastic deformation.

According to the dislocation elastic theory, the back stress generated by n_p dislocations in a pile-up at the grain center is:

$$\tau_p = \frac{n_p \mu b}{\pi d} \tag{4.20}$$

and the shear stress at the tip of the dislocation pile-up is:

$$\tau_{tip} = n_p \tau_p \tag{4.21}$$

The essential idea of the pile-up model is that τ_{tip}, the stress at the tip of the pile-up cannot exceed a critical stress τ_{GB}. Such stress is essentially the GB resistance. When the stress at the pile-up tip surpass τ_{GB}, dislocation transmission at GBs occurs and the number of dislocation stacks in a pile-up cannot increase any more. The maximum number of dislocations in the pile-up is then:

$$n_p = \sqrt{\frac{\pi d \tau_{GB}}{\mu b}} \tag{4.22}$$

Under such condition, the maximum back stress in the grain is expected to be:

$$\tau_p = \frac{\left(\sqrt{\frac{\pi d \tau_{GB}}{\mu b}}\right) \mu b}{\pi d} = \sqrt{\frac{\mu b \tau_{GB}}{\pi d}} \tag{4.23}$$

From Eq. 4.23, the empirical relationship of the HP law is derived. Experimental results show that the critical stress of GB τ_{GB} in metals is about several times the yield stress (Shen, Wagoner, and Clark, 1986). In (Ovid'ko, Sheinerman, and Valiev, 2014), a governing equation to calculate the critical stress τ_{GB} depending on the GB structure is proposed. Here, we use an average value of $\tau_{GB} = 250$ MPa for a qualitative calculation. Based on this value, the prediction of the pile-up model is plotted as a function of grain size d in Figure 4.8. The analytical solution of τ_p shown with a black curve defines the maximal shear stress we can applied to the grains before dislocation transmission takes place. In the case of localized plastic deformation in a grain such value correspond to the

maxi CRSS on active slip systems. When we reach this value, the plastic deformation is propagated into the adjacent grains. In summary, we propose that, whatever the grain size, it is impossible for τ_{CRSS} to exceed τ_p.

A detail analysis of Figure 4.8 showed that most of the calculations we made based on the DD simulation results give a prediction of τ_{CRSS} lower than τ_p. This implies that our simple model based on the influence of the initial dislocation microstructure is expected to be the dominating mechanism explaining a HP grain size effect. Only plastic deformation within grains of few tens of microns and with an initial dislocation density larger than 10^{12} m^{-2} impose the existence of dislocation transmission at GBs to reproduce a size effect. Here, it must be noted that the value of $\tau_{GB} = 250$ MPa we used for this test is conservative.

Now, for a given grain size, we calculate the limited critical resolved stress τ_{CRSS}^{lim} using solutions of τ_{CRSS} obtained from different initial dislocation density. There is one additional condition, if the value of τ_{CRSS} is greater than τ_p, we keep the latter as the τ_{CRSS}^{lim}. This calculation is to verify the dependence between τ_{CRSS}^{lim} and grain size d. In Figure 4.8b, τ_{CRSS}^{lim} is plotted as a function of $1/\sqrt{d}$ and a linear fitting is proposed between τ_{CRSS}^{lim} and $1/\sqrt{d}$ based on this modified model. In general, a linear dependence between τ_{CRSS}^{lim} and $1/\sqrt{d}$ is now predicted across a wide range of grain sizes. We can see that the size effect is predicted even for the coarse grain and the solutions of τ_{CRSS}^{lim} show a good agreement with the empirical HP law. This result suggests that when modeling the τ_{CRSS} as a function of initial dislocation density ρ_{ini}, our model can easily be improved to account for τ_p which physically account for the phenomena of plastic strain localization in coarse-grained materials. By doing so, the prediction of the HP effect can be successfully achieved with the new model we proposed whatever the initial dislocation density and the grain size.

Finally, it can be noted that due to the limitation of DD simulations on grain size, strain localization process could not be observed in the DD simulations and the relatively homogeneous plastic deformation we simulate allows for the formation of very few short dislocation pile-ups at low strain. Fortunately, the comparison made with the pile-up model in this section point out a relevant direction for improving our analysis in the case of coarse-grained materials. We did not push further this part of our work due to the lack of precise inputs regarding the GB resistance to dislocation transmission. Obviously, additional work on this question including atomistic simulation investigations is needed if we want to develop a more quantitative model of the HP effect.

4.4 Conclusion

DD model simulations based on the configuration of a plastically deformed grain within an elastic matrix were performed to study the physical origins of the HP effect. We show that, at low strain, the density of SSDs in the interior of grains does not change much. Strengthening and strain hardening are therefore mainly controlled by the back stress associated with the GNDs accumulated in a very thin slice close to GBs. At any plastic strain offset, the internal stress is found to be associated with two populations of dislocations: SSDs and GNDs. It's well known that the strengthening associated with SSDs is relatively low and can be readily calculated with the forest model. On the other hand, the back stress having a long-range effect associated with the GNDs was the subject of a lot of investigations. In this work, we propose an original model based on the surface density of GNDs to calculate the back stress. This model is derived from Nye's tensor calculations made in the close vicinity of GBs. Thanks to this model, the back stress at the grain center can be calculated with a linear function of the GND surface density. Furthermore, from simple geometrical analysis, we show that the storage rate of GNDs surface density is constant and independent of grain size. This theoretical prediction is confirmed by DD simulations. The increase of GNDs surface density is also found insensible to the grain size with the DD simulations. As a consequence, the strain hardening rate is dominated by the increase of back stress and is found to be identical in all the simulated grains with the same orientation independently of the grain size. This is a remarkable result because it reveals that the back stress associated with the accumulation of GNDs at GBs can be modeled with a linear relationship function of the plastic strain. Also, this result provides a physically-justified argument to explain the relative independence of the HP constant K with plastic strain.

As the back stress and the plastic strain hardening evolution are both found to be insensitive to grain size, the size effect reproduced with DD simulations can only be attributed to a difference of CRSS at yield, i.e., at the very beginning of plastic deformation. Additional investigations were then made to quantify the influence of the initial dislocation microstructure on the CRSS. Particularly, two strengthening mechanisms existing at the initiation of plastic deformation were studied, first the strengthening process related to the length of the FR source L; second the forest strengthening controlled by the dislocation-dislocation mean spacing and junction length in the initial dislocation microstructure of density ρ_{ini}. No matter the strengthening mechanism controlling the grain plasticity, the variation of the CRSS with grain size should be linearly proportional to $1/d$ or more precisely to $\ln(d/b)(1/d)$. The latter ln-term comes from the dislocation line tension property. However, the HP relationship calculated with the DD simulations is in better agreement with a $1/\sqrt{d}$ dependency. The deviation from

$\ln(d/b)(1/d)$ to $1/\sqrt{d}$ could be explained. This deviation comes from the rearrangement of the dislocation microstructure at the early stage of the dislocation dynamics. Such rearrangement is mainly driven by collinear annihilation. Such reaction modifies the characteristic length of the dislocation sources in the microstructure and tends to increase the length of some dislocation sources. This process is more effective in the small grains because the applied stress is higher. Our study indicates that the HP effect predicted from DD simulations is influenced by the detail organization of the dislocation microstructure. Under the combined effect of multiple strengthening and relaxation mechanisms, the grain size effect we simulated follows the empirical relationship of the HP law with a $1/\sqrt{d}$ dependency.

Finally, when extending our discussion to the case of coarse-grained alloys, the analysis we made of the DD simulations is found deficient. In industrial alloys where the dislocation microstructure is supposed independent of the grain size, a size effect is observed. This fact is *a priori* contradictory with our argument that the CRSS becomes constant in coarse grains with a relatively high initial dislocation density. For this reason, we investigated the possible issue of the localization of the plastic deformation and the formation of dislocation pile-ups at GBs. Those phenomena are connected to the question of dislocation transmission at GBs. The classical dislocation pile-up model provides a robust framework to define a criterion for plastic slip transmission at the GBs. The transmission is dependent on grain size and allows defining a pertinent upper bound for the CRSS. The definition of CRSS upper bound improves the model we first proposed, which allows now a good prediction of the HP effect across a wide range of grains sizes with a realistic initial dislocation density.

Conclusion and perspectives

The goal of my PhD was to address the size effect and the back stress induced by strain heterogeneities in polycrystalline materials. Two major challenges have been addressed: the physical mechanisms at the origin of the Hall-Petch effect and the quantification of back stresses induced by strain confinement. To accomplish this purpose, we used Dislocation Dynamics (DD) simulation, which is considered the most adapted technique for the investigation of dislocation collective properties.

To address the grain size effect, DD simulations were made on simple periodic polycrystalline aggregates composed of one or four grains. In addition, the influence of grain shape was explored by simulating grains with different aspect ratios: cube, plate or needle. Three crystal orientations [001], [111] and [135] were considered. Remarkably, the HP effect is successfully reproduced with these simple model simulations. Globally, the flow stress computed at low strain varies linearly with the inverse of the square root of the grain size, defined as the cube root of the grain volume. The HP constant K is found to be a function of the grain orientation and shape. A generalized HP law is proposed to quantify the influence of the grain morphology by defining an effective grain size. The average value of the HP constant K calculated at 0.2% of plastic deformation is close to the experimental values of copper. Another interesting feature is that dislocation storage rate recorded in DD simulations is proportional to the inverse of grain size $1/d$. Such result implies that SSDs density is hardly increased during the deformation and that dislocation storage occurs mostly at GBs. The part of GNDs stored at GBs generates long-range stresses that might be at the origin of size effect.

In order to quantify these size effects, the internal stress field inside grains, it is necessary to separate SSDs from GNDs in the dislocation population. DD simulations of a grain embedded by an elastic matrix, show that GNDs are localized in a thin layer close to GBs, that can be assimilated to a surface distribution of GNDs. In order to investigate the stress field induced by these dislocations, we first used DD simulations to compute the stresses induced by finite size dislocation walls of different height, length and characters: twist, tilt and epitaxial. In all cases, the stress is found proportional to the surface dislocation density, i.e. the same property as in the case of infinite dislocation walls. It is also found that the wall dimension effects can be captured with a

set of simple empirical equations involving the aspect ratio of the wall, the dislocation character and density. Using these equations it is possible to determine the stress field induced by dislocation walls of any size, character and average surface density, by summing the contribution of every surface Nye's tensor component on the wall. In a closed grain, the internal stress field can then be computed by adding the contribution of GNDs accumulating on every grain facets. The prediction of our model is tested and validated by a series of DD simulations with increasing complexity of the GND microstructure: pure / mixed character, uniform / random / heterogeneous distribution, single / double / multislip loading condition, embedded (in elastic medium) / periodic boundaries, one grain aggregate / four grain aggregates. In all the configurations, the stress predicted by the empirical equation is compared with that determined by DD simulations at the grain center. It was found that the accuracy of the predictions is degraded with the heterogeneousness of the GND distribution. The comparison shows that predictions are within 20% of the computed internal stresses.

The main conclusion obtained from the analysis of simulation results is that the calculated and predicted internal stresses increase linearly with strain but they are independent of the grain size. The implication of the back stresses induced by GNDs in the HP effect is therefore excluded. The observed size effect in the DD simulations is attributed to the threshold of plastic deformation, controlled by two competing mechanisms: the forest mechanism related to the initial dislocation density vs the Frank-Read source size affecting the critical stress of the activation of dislocation sources. DD simulations made with different grain sizes and initial dislocation microstructures making a constant number of sources per slip systems successfully predicted the HP effect. In such simulations, the yield stress is determined by the strength of source multiplication. This elementary mechanism justifies the existence of a HP effect in polycrystals with a low dislocation density, since in the latter cases the source length is necessarily proportional to the grain size. Similar DD simulations made with larger dislocation density like those expected in coarse-grained industrial materials could not reproduce a size effect. Indeed, the yield stress is then controlled by the forest mechanism that is not dependent on the grain size. However, from analytical calculations we showed that considering the existence of a strain localization inside the grains leads to the existence of a critical stress as predicted by the pile-up model. This proposition can be used in addition to the model we developed based on the DD simulation results and hence justifies the existence of a size effect regardless of the grain size or the dislocation density.

Several short- and long-term perspectives can be identified from this study. As suggested in Appendix B where a modified Kocks-Mecking model is proposed, the first thing to do is certainly to run crystal plasticity FEM computations. Such CPFEM

simulations should include the physical properties we identified from the DD simulations. For simple comparison with our results, an aggregate composed of cubic grains with random crystal orientations could be considered. These CPFEM simulations will provide answers on the capability of our model to quantitatively reproduce stress-strain curves for polycrystals with different textures. In addition, the same CPFEM simulations could be used to test its ability to reproduce a HP size effect with the condition of a homogeneous deformation inside the grains. Moreover, these CPFEM results could be compared with other constitutive forms of different levels of complexity, i.e. phenomenological approach, strain gradient approach, Cosserat formulation, etc. Once the validity of our model is confirmed under monotonous loading condition, cyclic loading conditions which are of great industrial interest could be further investigated. Hopefully, those efforts could be concluded by the formulation of a kinematic strain hardening model more physically justified and with a large domain of validity.

A second point of interest is related to the question of strain localization in the polycrystal grains and the way slip bands can progress from grain to grain at larger plastic deformation. The assumption of homogeneous deformation in the grain in our model was suggested by DD simulations made with relatively low dislocation density and at small strain. However, when extending to larger density and larger strain, some heterogeneities are known to take place. This is for instance the existence of strain localization and the formation of slip bands, or the formation of geometrically necessary boundaries inside the grains at the origin of extra GNDs density accumulation. Accounting for these plastic heterogeneities in a polycrystalline material to calculate the mechanical properties is a great challenge. New inputs on such issues will certainly come in next years from the progress of sub-micron experimental and simulation methods. The ongoing development of the Discrete-Continuous Model (DCM) developed at the LEM and recently coupled with spectral solvers will probably provide a robust approach to investigate such questions. The first simulations of slip bands inside one or a few grains part of polycrystal aggregate which is a “numerical clone” of real Diffraction Contrast Tomography experiments is now at our hand. Then, the effect of heterogeneous plastic deformation will become a problem that can be quantitatively addressed. Such type of simulations, when validated from experiments made at the same scale should allow us to broaden the scope of the existing physically justified CPL to the much larger strain.

Appendix A

Regular epitaxial dislocation facets

In simple cubic symmetry lattice, the geometry and dimension of the epitaxial facets considered in our simulations are reported in Table 3.1 and Table 3.2, respectively. An epitaxial facet generates three normal stress components σ_{xx}, σ_{yy} and σ_{zz}. We defined a rule to define the order of these three stress components (see Section 3.2.2). Following this order, individual analysis of the stress variation profile is then carried out.

The first stress component is σ_{zz}, the stress variations of simulated facet shapes of S1-S4 are plotted in Figure A.1a. Similar to the computed stress variations for twist facets, identical maximum amplitude is computed close to the facets and the stress amplitude decreases with the distance along x-axis. With the given surface dislocation density, the theoretical prediction of stress calculated with Eq. 3.16 is constant $\sigma_{zz}^{FDM} = 179$ MPa. Such prediction is much higher than the computed maximum amplitude about $\sigma_{zz}^{max} = 64$ MPa at $x = 0$ in Figure A.1a. The normalized stress variation curves are illustrated in Figure A.1b. The shape function of type $\xi_1(\hat{x}) = \exp(-a_{ep1}\hat{x})$ is used to fit the simulation results.

The second stress component is σ_{xx}, the stress variations of simulated facet shapes of S1-S4 are plotted in Figure A.2a. Similar to the computed stress variations for tilt facets, the stress amplitude first increases and then decreases. However, apparently the maximum stress amplitude is not influenced by the facet shape and remains a constant around $\sigma_{xx}^{max} = 12$ MPa. The theoretical prediction of stress calculated with Eq. 3.16 gives a much higher value $\sigma_{zz}^{FDM} = 135$ MPa. The normalized stress variation curves are illustrated in Figure A.2b. The shape function of type $\xi_2(\hat{x}) = \exp\left[-(\hat{x} - a_{ep2})^2/b_{ep2}\hat{x}\right]$ is used to fit the simulation results.

The third stress component is σ_{yy}, the stress variations of simulated facet shapes of S1-S4 are plotted in Figure A.3a. Similar to the computed stress variations for twist facets, identical maximum amplitude is found close to the facets and the stress amplitude decreases with the distance along x-axis. The maximum amplitude computed from DD

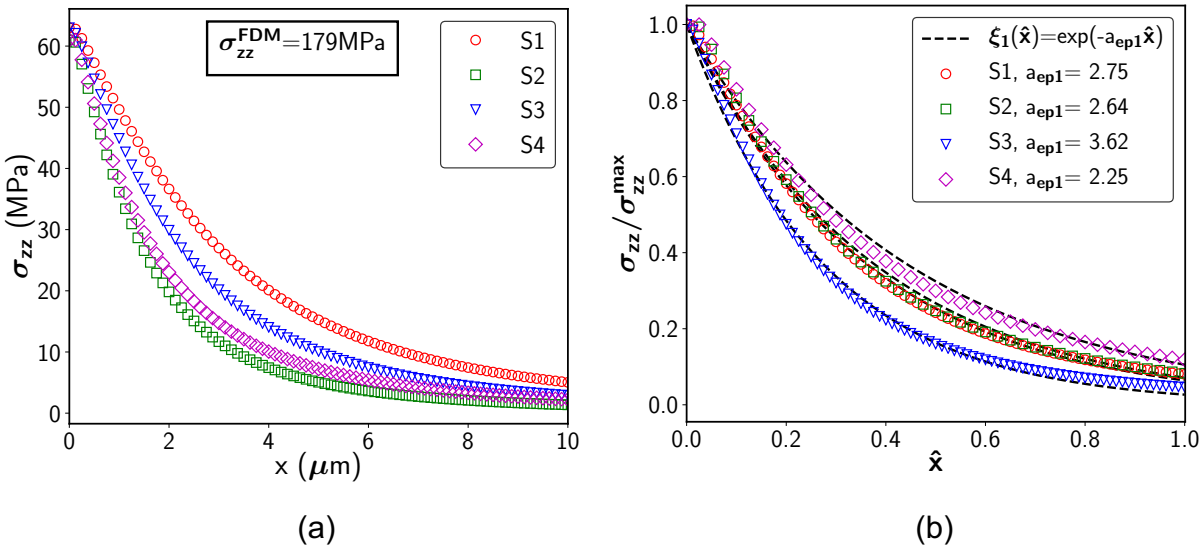

FIGURE A.1: (a) Variation of σ_{zz} with the distance from the epitaxial facet for the different simulated facet shapes (see Table 3.2). The theoretical solution of stress $\sigma_{zz}^{FDM} = 179$ MPa is calculated with Eq. 3.16. (b) Same curves as (a) but the stress is normalized by the maximum stress σ_{zz}^{max} and the distance x is normalized by the facet heights H ($\hat{x} = x/H$). Dashed lines are solutions of a fitting made with the shape function $\xi_1(\hat{x})$= exp(-$a_{ep1}\hat{x}$) where a_{ep1} is the coefficient determined by the fitting procedure.

simulation is found at $x = 0$ with the value $\sigma_{zz}^{max} = 22$ MPa. The theoretical solution of stress calculated with Eq. 3.16 is $\sigma_{yy}^{FDM} = 135$ MPa. The normalized stress variation curves are illustrated in Figure A.3b. The shape function of type $\xi_1(\hat{x}) = \exp(-a_{ep3}\hat{x})$ is used to fit the simulation results.

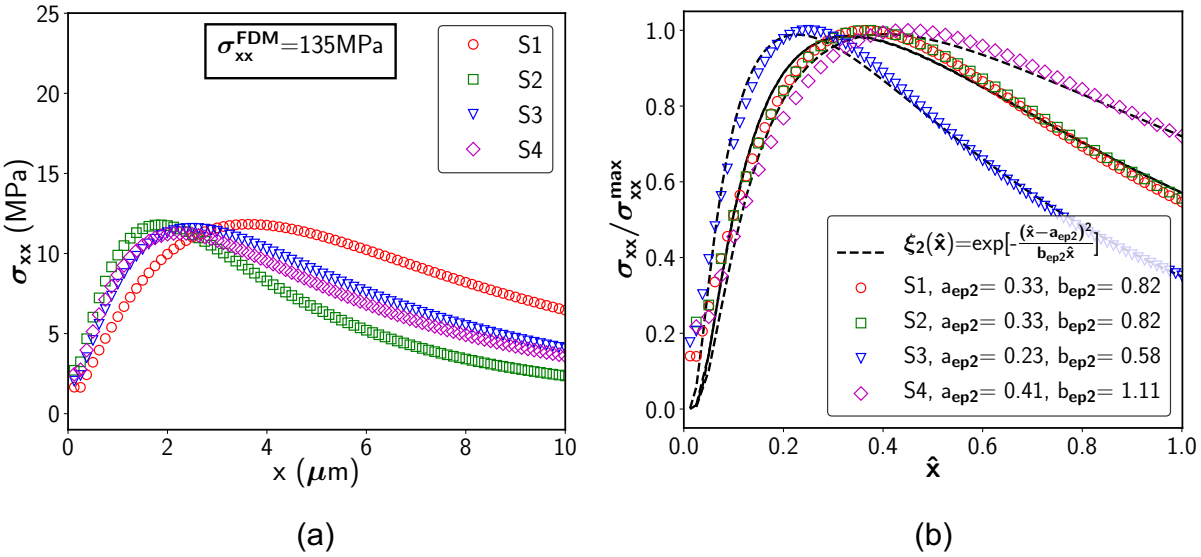

FIGURE A.2: (a) Variation of σ_{xx} with the distance from the epitaxial facet for the different simulated facet shapes (see Table 3.2). The theoretical solution of stress σ_{xx}^{FDM} = 135 MPa is calculated with Eq. 3.16. (b) Same curves as (a) but the stress is normalized by the maximum stress σ_{xx}^{max} and the distance x is normalized by the facet heights H ($\hat{x} = x/H$). Dashed lines are solutions of a fitting made with the shape function $\xi_2(\hat{x})$= $\exp\left[-(\hat{x} - a_{ep2})^2/b_{ep2}\hat{x}\right]$ where a_{ep2} and b_{ep2} are the coefficients determined by the fitting procedure.

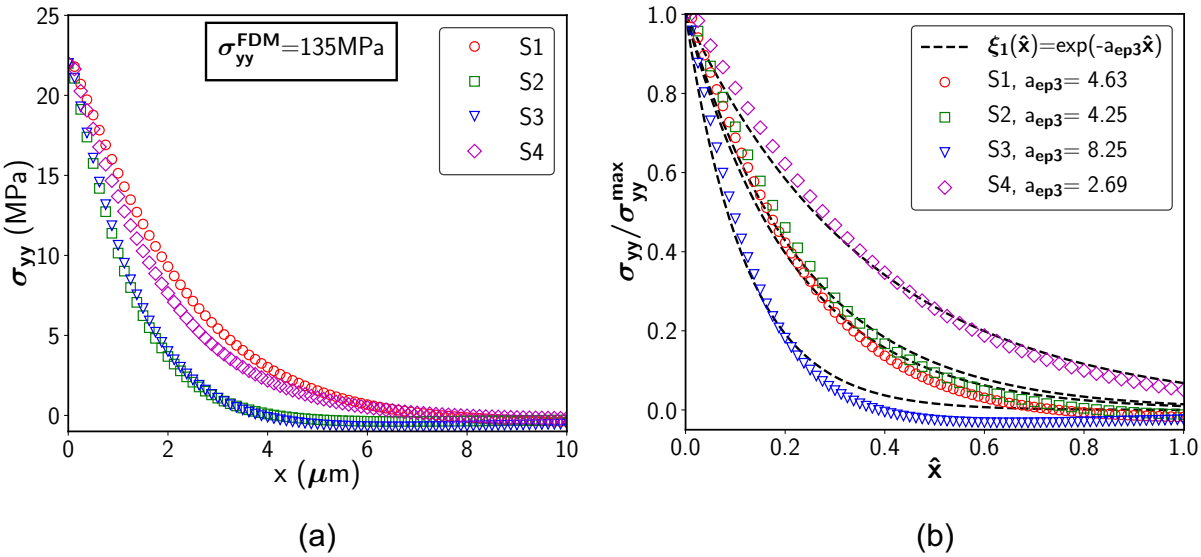

FIGURE A.3: (a) Variation of σ_{yy} with the distance from the epitaxial facet for the different simulated facet shapes (see Table 3.2). The theoretical solution of stress σ_{yy}^{FDM} = 135 MPa is calculated with Eq. 3.16. (b) Same curves as (a) but the stress is normalized by the maximum stress σ_{yy}^{max} and the distance x is normalized by the facet heights H ($\hat{x} = x/H$). Dashed lines are solutions of a fitting made with the shape function $\xi_1(\hat{x})$= exp(-$a_{ep3}\hat{x}$) where a_{ep3} is the coefficient determined by the fitting procedure.

Appendix B

Dislocations-based constitutive equations for modeling back stress

At first, we highlight the important information obtained from DD simulations. They are the basic features we consider to build up our set of constitutive equations:

- Inside grains, a significant GNDs density is accumulated in the close vicinity of GBs.
- The back stress induced by such GNDs is maximal and relatively homogeneous at the center of grains.
- The storage rate of GNDs density accumulated at the GBs can be rationalized with a simple linear function of the total grain deformation.
- An empirical model, based on regular facets of GNDs (validated with DD simulations), allows to calculate the back stress associated with any combination of dislocations decorating a GB facet.
- A linear rule of mixture can be applied to reconstruct the back stress at the center of grains by considering the contribution of each GB facet and the GND density accumulated on each side of those facets.
- The GNDs density contribution to isotropic hardening is negligible (Daveau, 2012).

The modeling approach we propose is based on the well-known Kocks-Mecking approach. Today, this dislocation density based model first developed by Kocks and Mecking (Kocks and Mecking, 2003) is a robust solution to calculate plastic strain hardening from a master equation prediction the evolution of the dislocation density with plastic strain. For coarse-grained polycrystals, the evolution of the dislocation density on each slip system, ρ^s, is calculated as the outcome of both storage and recovery process, expressed as:

$$\frac{d\rho^s}{d\gamma^s} = M(\frac{\beta}{b}\sqrt{\rho^s} - y_r\rho^s) \tag{B.1}$$

where M is the Taylor factor, β is a coefficient accounting for the dislocation mean free path within the forest dislocation network, b is the Burgers vector and y_r is a parameter accounting for the annihilation rate of dislocations related to dynamic recovery processes. In a second step, substituting the dislocation density into the Taylor equation the critical resolved shear stress can be calculated. If one needs to assess the dislocation interaction strength for a given slip system, τ_c^s, the Taylor equation is formulated into a matrix form first proposed in (Franciosi, Berveiller, and Zaoui, 1980) and later calculated with DD simulations (Devincre, Kubin, and Hoc, 2006):

$$\tau_c^s = \mu b \sqrt{\sum_p \alpha^{sp} \rho^p} \tag{B.2}$$

where τ_c^s is the CRSS to activate dislocations glide in a slip system "s". This quantity depends on the interaction with the other slip systems of density ρ^p. The strength of the interaction between slip systems is given by the interaction matrix coefficient α^{sp}. Eq. B.2 is enough to define the flow stress in a single crystal as it reflects the short-range stress resulting from forest interactions. Such interactions control the dislocation dynamics in a crystal free of GNDs. In the case of a polycrystal, one needs to account for the long-range stress related to the GNDs accumulated at GBs. Eq. B.2 must then be complemented by an additional term τ_{back}^s that is the back stress projected onto the slip system "s":

$$\tau_c^s = \mu b \sqrt{\sum_p \alpha^{sp} \rho^p} + \tau_{back}^s \tag{B.3}$$

In the following paragraphs, the procedure of the back stress calculation is divided into steps. For the sake of simplicity, grains of cubic shape are considered. At low strain, we assume GBs as impenetrable by dislocations; hence the grains are a closed cube with six facets with different indexes "f".

Step 1: Storage rate of GNDs accumulated at GBs

We showed in Chapter 4 that in the case of homogeneous deformation inside a grain, the storage rate of surface GNDs is a constant. The latter quantity present no dependence on the grain size. The storage rate of GNDs accumulation at GBs is only a function of shear strain, so the increase of surface GND density is expressed as:

$$\dot{\rho}_{GND}^{sf} = C^{sf} \dot{\gamma}^s \tag{B.4}$$

where C^{sf} is the storage rate of GNDs of slips system "s" on facet "f". It depends on the plastic strain activity of slip system and the geometry of GB facets. The value of

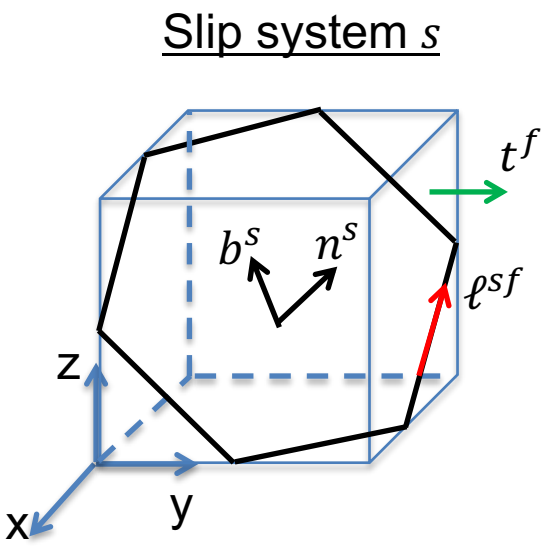

FIGURE B.1: Schematic illustration of a cubic grain with a dislocation loop deposited on GBs. Index "s" is assigned for the slip system and "f" is assigned for the GB facet.

C^{sf} can be calculated from simple geometrical models or alternatively measured directly from DD simulation. In Chapter 4, we show that both approaches give similar results.

In Eq. B.4, the plastic shear strain rate $\dot{\gamma}^s$ can be averaged in FEM simulations at the grain scale from the deformation of the mesh elements within each grain.

Step 2: Build-up of surface Nye's tensor

For a given slip system, the storage of GND density inside a grain is known from Eq. B.4. Now, this scalar value $\dot{\rho}^{sf}_{GND}$ is converted into a matrix form as to define a surface Nye's tensor $\dot{\underset{\sim}{\boldsymbol{\alpha}}}^{sf}_{GND}$:

$$\dot{\underset{\sim}{\boldsymbol{\alpha}}}^{sf}_{GND} = \dot{\rho}^{sf}_{GND}(\underline{\boldsymbol{b}}^s \bigotimes \underline{\boldsymbol{l}}^{sf}) \tag{B.5}$$

where $\underline{\boldsymbol{l}}^{sf}$ is a normalized dislocation line vector. As illustrated in Figure B.1, this parameter varies depending on the slip system s and GB facet f. For numerical efficiency, the values of $\underline{\boldsymbol{l}}^{sf}$ can be tabulated at the beginning of simulations based on the FEM mesh geometry. This simplification is made possible if the crystal rotations are neglected with the hypothesis of small deformation. The conditions to determine $\underline{\boldsymbol{l}}^{sf}$ are as follows:

$$\begin{cases} \underline{\boldsymbol{l}}^{sf} \perp \underline{\boldsymbol{n}}^s \\ \underline{\boldsymbol{l}}^{sf} \wedge \underline{\boldsymbol{b}}^s \\ \underline{\boldsymbol{l}}^{sf} \perp \underline{\boldsymbol{t}}^f \end{cases} \tag{B.6}$$

where the term $\underline{\boldsymbol{t}}^f$ is the normal vector to the GB facets, see Figure B.1.

Finally, the total surface Nye's tensor that is the one associated to all the GNDs stored at a GB facet is obtained by summing up the contributions of the slip systems:

$$\dot{\underset{\sim}{\boldsymbol{\alpha}}}^f_{GND} = \sum_s \dot{\underset{\sim}{\boldsymbol{\alpha}}}^{sf}_{GND} \tag{B.7}$$

Here, it must be noted that the calculation of Nye's tensor, for a given GB facet, needs to take into account the accumulation of GNDs on both sides of the GB facets that separate two adjacent grains. To do such operation simply, a tabulation assigning each GB facet to two grains is helpful. This way, a direct link is made between the grains deformation and each facet properties.

Step 3: Decomposition of the surface GNDs density in different characters

This procedure has been introduced in Chapter 3. The main idea is to decompose a GB facet with a surface GNDs density made of dislocations of any type into 3 simpler elementary GB facets of basic character, i.e. twist, tilt and expitaxial characters. Such operation can be made by considering a virtual crystal of simple cubic symmetry. Nine independent slip systems in simple cubic symmetry are defined in a common natural basis and each of them is related to a component of the Nye's tensor.

In what follows, we use a simple example to illustrate how to proceed with such decomposition procedure. Here, a GB facet perpendicular to z-axis having equidistantly lined-up mixed dislocations is illustrated in Figure B.2.

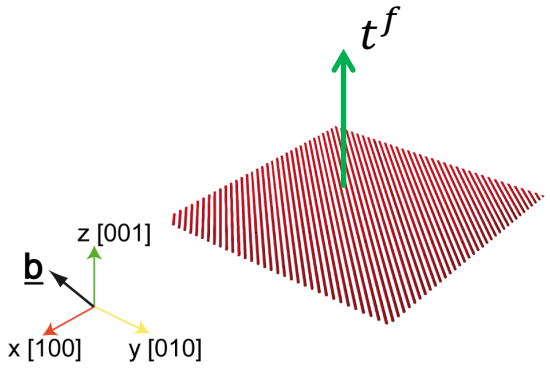

FIGURE B.2: Mixed dislocation equidistantly distributed in a GB facet with the facet normal $\underline{\boldsymbol{t}}^f$ parallel to the z-axis.

The conditions to identify the character of the Nye's components α_{ij} are the following:

$$\text{for } \alpha_{ij}: \begin{cases} (i=j): \text{Twist} \\ (i\neq j)\&(i=t_f): \text{Tilt} \\ (i\neq j)\&(i,j\perp t_f): \text{Epitaxial} \end{cases} \tag{B.8}$$

In a general case, a full Nye's tensor could have 9 non-zero components describing the GNDs distribution in space. In Chapter 2, we observed that GNDs are mainly accumulated in the very thin slices close to GBs. This observation implies that the GNDs distribution in space can be dealt as a 2D distribution of GNDs confined in a surface. If we take the example given in Figure B.2, the facet normal is parallel to z-axis $\underline{\boldsymbol{t_f}} = \underline{\boldsymbol{z}}$. We can easily convert a general full Nye's tensor to a surface Nye's tensor with the assumption of surface distribution of GNDs. Since there is no dislocation segments out of facet, all the components in $\underset{\sim}{\boldsymbol{\alpha}}$ having dislocation line direction out of facet reduce to zero, i.e. $\alpha_{ij}(j=z)=0$:

$$\begin{pmatrix} \alpha_{xx} & \alpha_{xy} & \alpha_{xz} \\ \alpha_{yx} & \alpha_{yy} & \alpha_{yz} \\ \alpha_{zx} & \alpha_{zy} & \alpha_{zz} \end{pmatrix} \xrightarrow[\alpha_{ij}(j=z)=0]{\text{Surface distribution}} \begin{pmatrix} \alpha_{xx} & \alpha_{xy} & 0 \\ \alpha_{yx} & \alpha_{yy} & 0 \\ \alpha_{zx} & \alpha_{zy} & 0 \end{pmatrix} \tag{B.9}$$

Now, 6 components remained and we need to identify their characters. By applying the rule given in Eq. B.8, we know that:

$$\begin{cases} \alpha_{xx}, \alpha_{yy}: \text{Twist} \\ \alpha_{zx}, \alpha_{zy}: \text{Tilt} \\ \alpha_{xy}, \alpha_{yx}: \text{Epitaxial} \end{cases} \tag{B.10}$$

Step 4: Calculation of the GNDs-based stress tensor

At this step, the general formula $\underset{\sim}{\boldsymbol{\alpha}} \simeq curl\underset{\sim}{\boldsymbol{U}}_e$ is used with the small deformation assumption:

$$\begin{pmatrix} \alpha_{xx} & \alpha_{xy} & \alpha_{xz} \\ \alpha_{yx} & \alpha_{yy} & \alpha_{yz} \\ \alpha_{zx} & \alpha_{zy} & \alpha_{zz} \end{pmatrix} = \begin{pmatrix} U_{xz,y} - U_{xy,z} & U_{xx,z} - U_{xz,x} & U_{xy,x} - U_{xx,y} \\ U_{yz,y} - U_{yy,z} & U_{yx,z} - U_{yz,x} & U_{yy,x} - U_{yx,y} \\ U_{zz,y} - U_{zy,z} & U_{zx,z} - U_{zz,x} & U_{zy,x} - U_{zx,y} \end{pmatrix} \tag{B.11}$$

When a surface Nye's tensor is defined with a local simple cubic basis having one axis perpendicular to the facet, maximum 6 non-zero components can be found within the tensor as given in Eq. B.9. Let us consider the GNDs facet illustrated in Figure B.2,

the general equation in Eq. B.11 can be then simplified by eliminating the components out of plane $\alpha_{ij}(j = z)$ and $U_{ij,k}(k \neq z)$ and it reduces to:

$$\begin{pmatrix} \alpha_{xx} & \alpha_{xy} & 0 \\ \alpha_{yx} & \alpha_{yy} & 0 \\ \alpha_{zx} & \alpha_{zy} & 0 \end{pmatrix} = \begin{pmatrix} -U_{xy,z} & U_{xx,z} & 0 \\ -U_{yy,z} & U_{yx,z} & 0 \\ -U_{zy,z} & U_{zx,z} & 0 \end{pmatrix} \tag{B.12}$$

Therefore, from the equality given in B.12, 6 equations are to be resolved to obtain the stress contribution associated with each component in Nye's tensor. At first, these equations can be resolved using the FDM theory based on an infinite surface singularity of dislocations (see Section 3.1).

In order to take into account of stress variations induced by the finite size of GB facets, the character of components in Nye's tensor $\underset{\sim}{\boldsymbol{\alpha}}$ needs to be identified. Such identification has been done in Step 3, then the true stress field $\underset{\sim}{\boldsymbol{\sigma}}^{\boldsymbol{f}}{}_{GND}$ generated by GB facets at the grain center can be readily calculated. We only need to multiply the theoretical FDM solution with the intensity factor F and the shape functions $\xi(\hat{x})$. The two latter are identified from DD simulations results (see Chapter 4).

Considering that the problem we solve is based on linear elasticity, the full stress tensor $\underset{\sim}{\boldsymbol{\sigma}}_{GND}$ within the grain is the sum of the stress fields generated by all the above calculated GB facets contributions $\underset{\sim}{\boldsymbol{\sigma}}^{\boldsymbol{f}}{}_{GND}$.

Step 5: Contribution of the back stress to the slip systems CRSS

Once $\underset{\sim}{\boldsymbol{\sigma}}_{GND}$ is defined at the grain center, a projection calculation is required to determine the back stress τ^s_{back} with respect to the slip system s:

$$\tau^s_{back} = \underset{\sim}{\boldsymbol{\sigma}}_{GND} \underline{\boldsymbol{b}}^s \underline{\boldsymbol{n}}^s \tag{B.13}$$

For every slip system, the back stress τ^s_{back} must be computed at each simulation time step increment. This calculation allows to take into account the increase of long-range internal stress with the plastic strain evolution. Then, τ^s_{back} is added to the short-range internal stress $\mu b\sqrt{\sum_p \alpha^{sp}\rho^p}$ to give a full description of the CRSS.

Appendix C

Back stress in a grain simulated with PBC

In this appendix, the back stress in a grain simulated with periodic boundary conditions (PBC) is investigated. At first, we compare the deformation behaviors of three simulations performed with different boundary condition: a single crystal, a grain embedded in infinite elastic matrix and a grain simulated with PBC. For the simplicity of expression, the two latter are named as embedded grain and periodic grain.

We first summarize the elements common to all the simulations. The grain size is 10 μm and the grain shape is cubic. To simulate a singe crystal, the tested shape is slightly modified from a cube to a cuboid in order to avoid the simulation artifact related to the self annihilation of dislocations. The initial dislocation microstructure is made with a random distribution of FR sources of 3 μm long belonging to one slip system. A tensile loading along the direction [135] is used to make the grains deform in single slip. The initial dislocation density is identically set as $\rho_{ini} = 0.5 \times 10^{12}$. The mechanism of CS is deactivated.

The schematic illustration of a single crystal is shown in Figure C.1a. The boundaries of the simulated crystal are transparent. The use of PBC makes the simulated crystal be surrounded by its replicas. An infinite number of replicas with transparent boundaries allows to simulate the dislocation dynamics in a singe crystal. The schematic illustration of an embedded grain is shown in Figure C.1b. Only the grain at center can be plastically deformed and its surrounding is an elastic media. The schematic illustration of a periodic grain is shown in Figure C.1c, where one grain is surrounded by its replicas. The solid black lines in C.1b and c are used to show the impenetrable interfaces of the GBs.

All the three simulations have an identical tensile loading and they are deformed to 0.2% of plastic strain. The increase of stress with the plastic strain is plotted in Figure

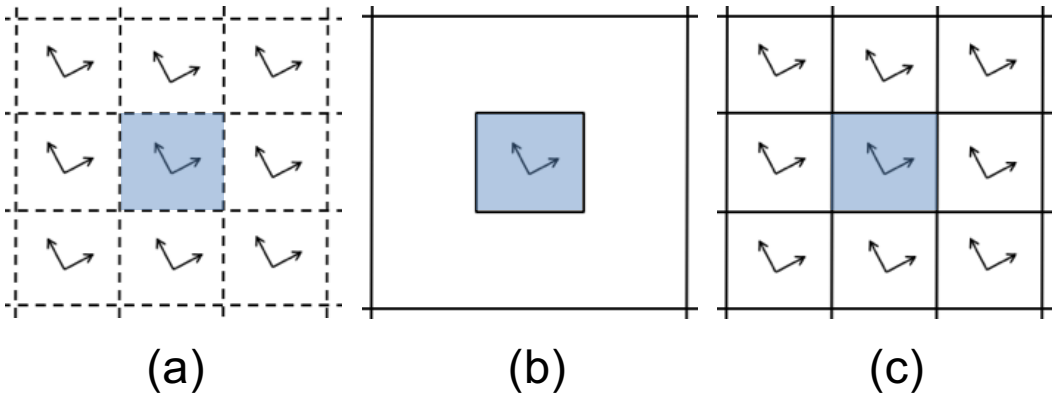

FIGURE C.1: Schematic illustrations of the simulation configuration of (a) a single crystal, (b) a embedded grain and (c) a periodic grain. Dashed lines are transparent boundaries and solid lines are impenetrable boundaries.

C.2a. The increase of dislocation density with the plastic strain is plotted in Figure C.2b. As excepted, the stress and the dislocation density amplitudes are the lowest for the single crystal. Then, for the embedded grain, the stress is significantly increased as well as the dislocation density. Such effect is induced by a large amount of GNDs accumulated in the close vicinity of GBs. The last simulation is carried out on a periodic grain, the increase of dislocation density is similar to the one of embedded grain, but the stress is dramatically reduced. This abrupt stress drop is expected since a GND density with opposite signs is accumulated on both sides of the GBs. Then, the back stress is mostly annihilated. However, we see that the stress of periodic grain is still higher than one of single crystal, which means that the annihilation of the back stress at the GBs is not perfect. The residual back stress we observe in periodic grain results into a weak but not negligible strain hardening.

In this appendix we want to explain the origin of a the back stress we observed in a periodic grains.

Inside a grain, the dislocations accumulated on the opposite sides of a grain are in opposite signs. When a grain is next to its replica, positive dislocations on a given slip system stored at a GB meet negative dislocations on the same slip system stored on the other side of this GB. In the case of homogeneous deformation, the GBs are fully filled with dislocations, see Figure C.3a and the elastic fields of positive and negative dislocations cancel each other. No back stress is then generated. However, in the simulations and in real grains, the existing FR sources in the initial dislocation microstructure cannot be perfectly distributed. More precisely, the distribution of FR sources is heterogeneous inside a grain because FR sources of a fixed length cannot exist in some regions of the grains. For instance, in our simulations, the initial FR sources cannot be

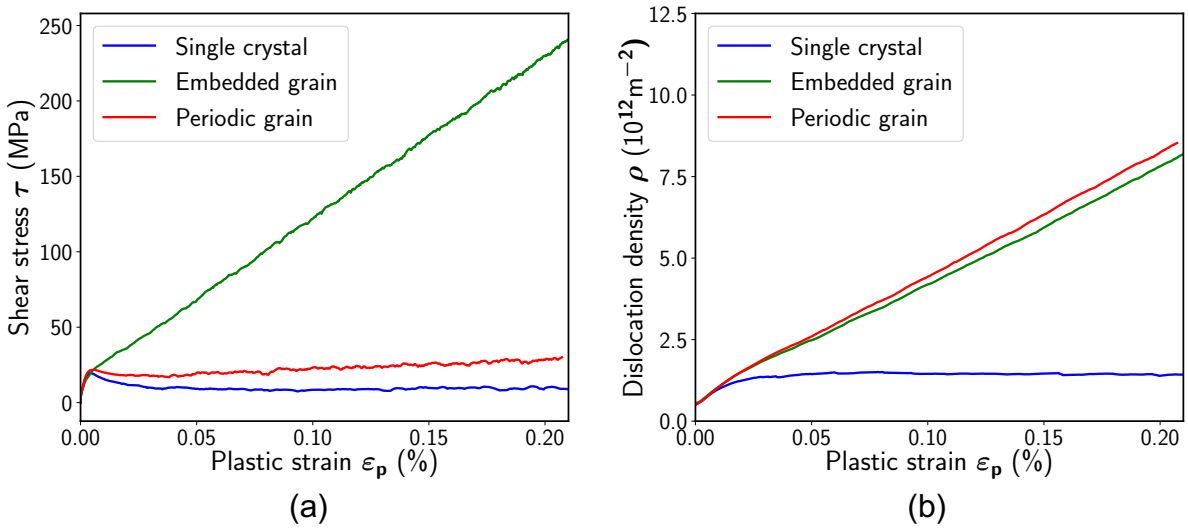

FIGURE C.2: A single crystal, an embedded grain and a periodic grain are simulated with identical initial conditions. The increase of shear stress (a) and the increase of dislocation density (b) are plotted as a function of plastic strain to 0.2%.

introduced in corners of a cubic grain. This heterogeneity of the dislocation microstructure induces the heterogeneity of the surface GNDs density at GBs. Here, it must be noted that this problem can only be partially eliminated by considering the gross-slip mechanism during the simulation of dislocation dynamics. Hence, when the dislocations arrive on both sides of a GB (see Figure C.3b), in the periodic grain the GND density is annihilated only in the central area of this GB but, the dislocation density on the top and bottom corners are polarized. Such polarized dislocations are simply GNDs that give rise to a residual back stress.

In the periodic grain, the Nye's tensor is computed in a GB region of 0.4 μm thick by taking account of both positive and negative dislocations stored on each side of the GBs. In Figure C.4, a 3D map of Nye's tensor component α_{xy} is shown. The dimensions of the GB facet are shown along x- and y-axis. The amplitude of the Nye's tensor component α_{xy} is shown along the z-axis. We see, in the central area of the map, that α_{xy} is close to zero. It means the positive and negative dislocations stored in the central area of GB surface annihilate each other and it leaves no excess of GNDs. However, we can see in the two corners of the map, the amplitude of α_{xy} is high with opposite signs. It proves that the distribution of dislocations on the GB surface in the simulated periodic grain is heterogeneous. When the two face-to-face GBs are superposed in a periodic scheme, the annihilation of dislocations of opposite signs is not perfect. Such result computed from DD simulation is in agreement with the 2D schematic illustration shown in Figure C.3b.

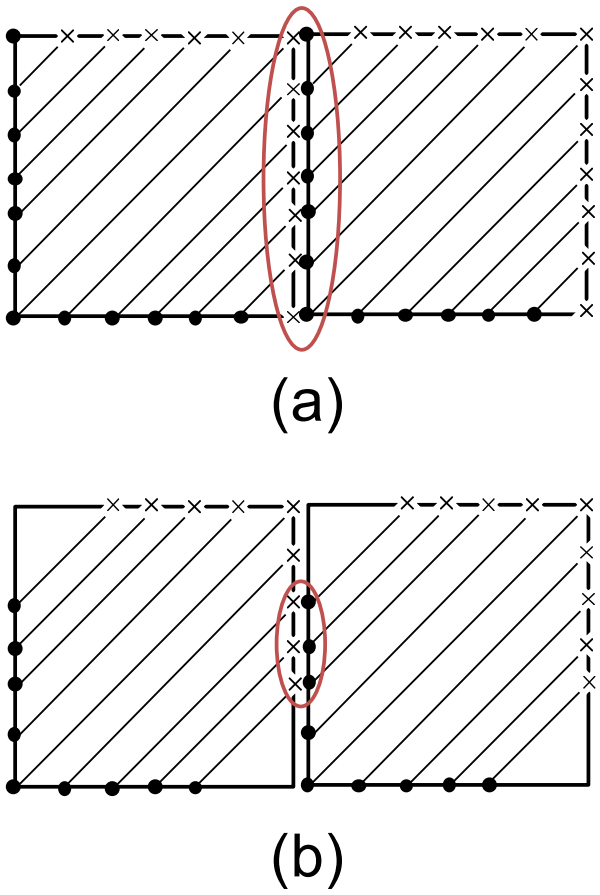

FIGURE C.3: (a) In an ideal case of perfect homogeneous deformation, dislocation lines filled the entire GB surface. The stress fields of opposite dislocations are annihilated, thus no back stress is generated. (b) In a real case, dislocation lines filled a part of GB surface because the initial dislocation microstructure is heterogeneous. The stress fields of dislocations of opposite signs are not totally annihilated, which gives rise to some residual back stress.

Due to the heterogeneous distribution of dislocations, the existence of a small population of GNDs at the GBs of the periodic grain is detected. We isolated the GB surface in Figure C.4 and calculated the associated internal stress tensor. In Figure C.5, the average distribution of internal stress components is plotted as a function of the distance along z-axis with colored symbols. The back stress τ_{back}, calculated as the projection of internal stress tensor onto the slip plane, is plotted with black dashed line. We can see that the internal stress components and the back stress are certainly not zero close to GB facet. Their amplitudes decrease with the distance far from the GB facet. The back stress shown in Figure C.4 is only associated with one GB. If we take into account the six GBs of a closed periodic cubic grain, the total amplitude of back stress will be high enough to induce some strengthening leading to the strain hardening of the periodic grain shown in Figure C.2a.

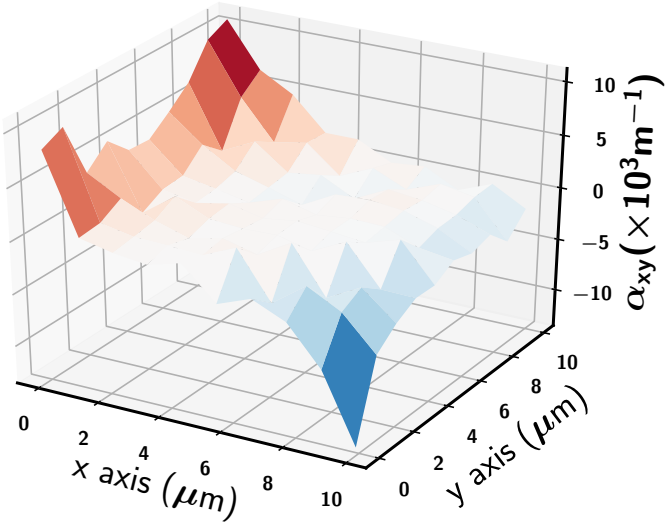

FIGURE C.4: The Nye's tensor component α_{xy} calculated in a GB region of 0.4 μm thick by including both positive and negative dislocations stored on each side of GB is illustrated in a 3D map. The dimensions of GB facet are shown along x- and y-axis. The calculated value of α_{xy} is shown along the z-axis.

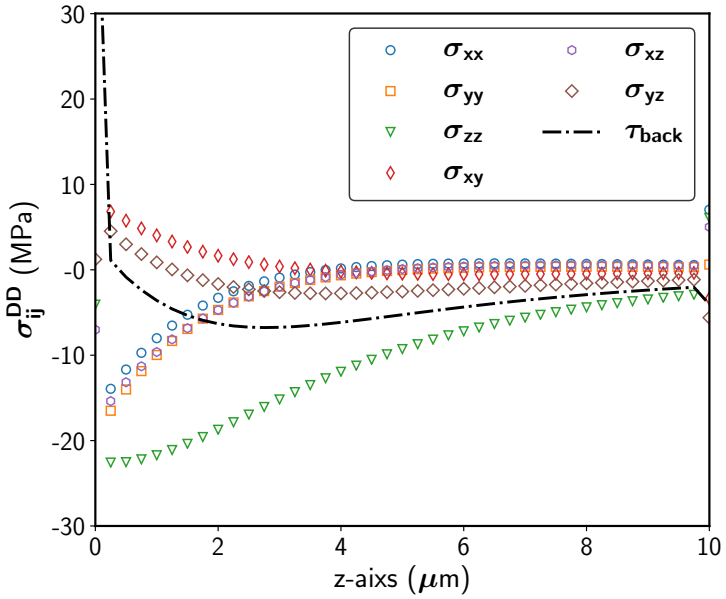

FIGURE C.5: Average distribution of internal stresses generated by a GB facet in Figure C.4 is plotted as function of distance along its normal axis, i.e. the z-axis. The internal stress components are shown in colored symbols. The back stress τ_{back} is calculated as the projection of internal stress tensor onto the tested slip plane and is shown in dashed line.

It has to be noted that it is not possible to calculate the back stress generated by the heterogeneous distributions of GNDs in the periodic grains using the model we developed. Indeed, the latter is based on an assumption of a homogeneous distribution of GNDs on the GB surface. For instance, the average surface GND density of the GB facet in Figure C.4 is zero and our model predicts no back stress, which as we have seen is not correct. Nevertheless, in the case of grain aggregate, the back stress associated with the heterogeneous distribution of GNDs is secondary compared with the back stress generated by the average distribution of surface GNDs. One possible way to account for such secondary effect is to introduce an additional back stress related to the gradient of the surface GND density. Due to lack of time, such possibility was not considered during the PhD.

Appendix D

Single source strengthening vs dislocation forest strengthening

Here we performed three DD simulations to study the effect of the initial microstructure of dislocations regarding the plastic threshold. In particular, we illustrated the competition between single source strengthening and forest strengthening in controlling the amplitude of CRSS. In Section 4.3.3, we compared the CRSS computed from DD simulations τ_{CRSS}^{DD} with the analytical solutions obtained from the Taylor equation and the Foreman equation (see Figure 4.6). We pointed out that due to the low initial dislocation density used in the simulations, the computed CRSSs were actually systematically dominated by the strength of the multiplication of FR sources. In order to provide more supporting results to this argument, three additional simulations have been performed.

Three cubic grains of size 2.5 μm embedded in an elastic matrix are deformed with a tensile loading in the [100] direction. Three initial dislocation densities are tested by increasing the number of initial FR sources. The length of FR sources is set the same for all the grain simulations as $L = 0.75$ μm. The simulation parameters are summarized in the following Table D.1. In Figure D.1, the increase of flow stress (a) and the evolution of dislocation density (b) as a function of plastic strain are shown.

Grain size $d(\mu m)$	2.5	2.5	2.5
Number of FR sources	130	243	487
Initial dislocation density $\rho_{ini}(10^{12}m^{-2})$	8	15	30

TABLE D.1: Main parameters used in the simulations of three grains of same size with increasing initial dislocation density.

One important remark is that the CRSSs at the yield points in Figure D.1a are of the same amplitude although the initial dislocation density differs. The initial dislocation density ρ_{ini} listed in Table D.1 are used to calculate τ_T with the Taylor equation and their values are marked in Figure D.1a with square symbols. One can see that τ_T increases when ρ_{ini} is increasing. τ_T predicts the yield point correctly on the simulated

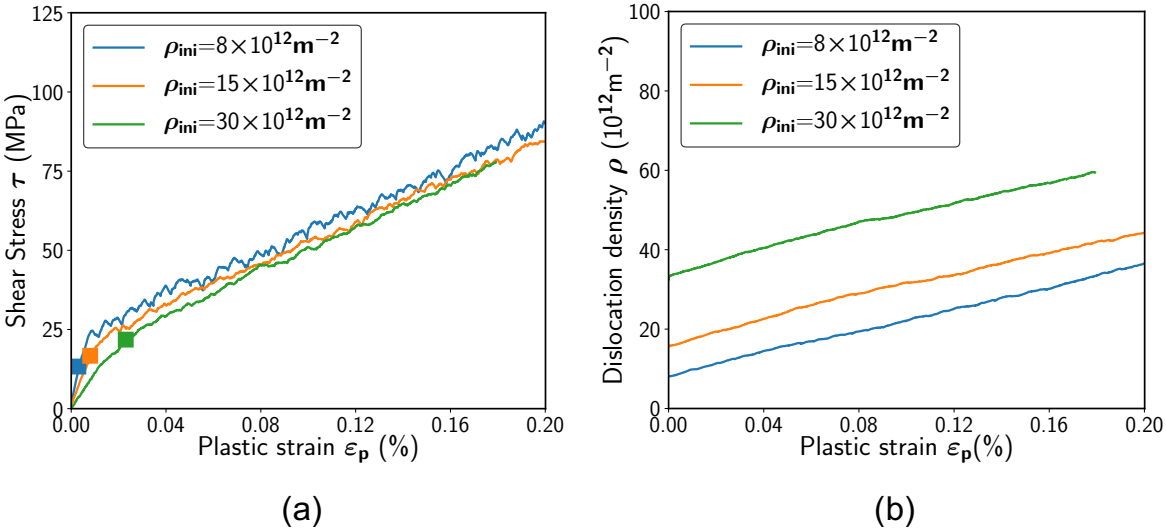

FIGURE D.1: (a) The increase of the flow stress and (b) the evolution of the dislocation density are plotted as a function of the plastic strain. Three simulations are carried with increasing initial dislocation density for a given grain size 2.5 μm. The length of the FR sources is set as $L = 0.75$ μm for all the tested grains. The tensile loading is along the [100] direction. The CRSS calculated with the Taylor equation using the initial dislocation density ρ_{ini} given in Table D.1 are marked with square symbols.

stress-strain curve only for the highest initial dislocation density $\rho_{ini} = 30\times10^{12}m^{-2}$ (the green curve). This demonstrates that the mechanism of forest strengthening becomes dominant when the ρ_{ini} is high enough, otherwise the magnitude of the CRSS is dictated by the mechanism single source strengthening. We can compare the two characteristic lengths, the first is the length of the FR source L and the second is the mean distance between dislocations approximate to $1/\sqrt{\rho_{ini}}$. Only when L becomes larger than three times the $1/\sqrt{\rho_{ini}}$, the CRSS is eventually controlled by the initial dislocation density ρ_{ini}. Such result is in agreement with one previous study (Devincre, Kubin, and Hoc, 2006).

In addition, we see in Figure D.1a that the increase of the flow stress is identical for all the simulations. This result again confirms the analysis we made in Section 4.3.2. The evolution of the back stress at low strain is only related to plastic strain rather than other simulation features, such as the initial dislocation microstructure or the grain size.

Appendix E

Rearrangement of initial dislocations microstructure

In Figure 4.6 (Section 4.3.3), a good agreement is found between the CRSS computed with DD simulations and the CRSS calculated with the Foreman equation for the larger grains. However, an increasing disparity between the theoretical and the computed CRSS is observed when the simulated grain size is reduced. We've argued that such discrepancy results from the formation of long FR sources in the initial dislocations microstructure when the smaller grains are deformed. In this appendix, we provide evidence to show how this rearrangement of the initial dislocations microstructure proceeds and influences the CRSS amplitude.

Here we analyze the evolution of the dislocations microstructure for two simulations. The first one is made with a small grain size $d = 1.25\ \mu m$ and the second one is made with a larger grain size $d = 10\ \mu m$. The parameters defining the initial dislocation microstructure used in these two simulations are given in Table 4.1. We calculate the length distribution of curved segments pinned at their ends (FR sources) inside both grains in the early stage of plastic deformation. More precisely, the dislocation microstructure is characterized when the first dislocation loop is deposited at the GBs. The two histograms of length distribution are plotted in Figure E.1 for (a) the small grain $d = 1.25\ \mu m$ and (b) the large grain $d = 10\ \mu m$. As we can see, the length distribution in the small grain is spread out, while the length distribution in the large grain is thinner. In the small grain, the distribution of segments longer than $0.5\ \mu m$ is not negligible. It indicates that a few FR sources with a length much longer than the initial length ($0.375\ \mu m$) were formed during the first steps of the simulation. As a result, the critical shear stress in this grain is decreased since dislocation multiplication can exist at lower applied stress. On the other hand, the length distribution in the large grain is mainly located in the range between 3 and 4 μm, which is close to the initial source length of 3 μm long. Such result suggests that the length distribution of FR sources in the dislocation microstructure is unchanged. Therefore, the computed CRSS for this

grain is consistent with the theoretical solution given by the Foreman equation. Such different behavior with the grain size explains the systematic deviation we observed in Figure 4.7 for the smaller grains with respect to the theoretical solution of the form $ln(d)/d$.

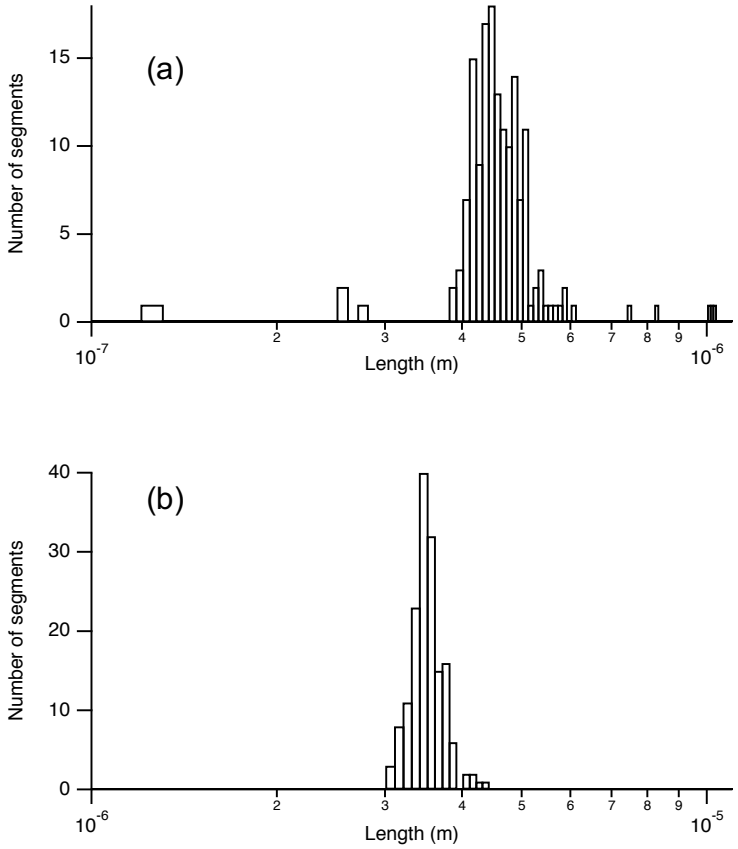

FIGURE E.1: Length distribution of curved FR sources in (a) the small grain $d = 1.25\ \mu m$ and (b) the large grain $d = 10\ \mu m$ before the first dislocation segment arrived at GB.

We tracked in the small grain $d = 1.25\ \mu m$ the formation process of long FR sources. This process is illustrated in Figure E.2 with a screenshot made of 4 images. In this simulation sequence, the 2 FR sources we observe are of pure screw character and the direction of their Burgers vector $\underline{\boldsymbol{b}}$ is noted in Figure E.2a. The Cross-Slip (CS) mechanism is activated and the dislocation line sections belonging to the collinear slip systems with the same Burgers vector are noted with different colors (green and blue, respectively). In Figure E.2b, owing to a double cross-slip process, two super jogs (the left one is marked with a pink dashed arrow) are formed along the dislocation line. Then, as pointed out with two red arrows in the image (b), the attractive force between line sections with the opposite sign leads to a collinear annihilation. In Figure E.2c, we see that the annihilation reaction leaves a tiny FR source and a much longer FR source.

Both segments contain a super jog, pointed out with two yellow arrows. At last in Figure E.2d, the formed long source expands rapidly because the line tension to bow out such long FR source is made possible at a lower stress.

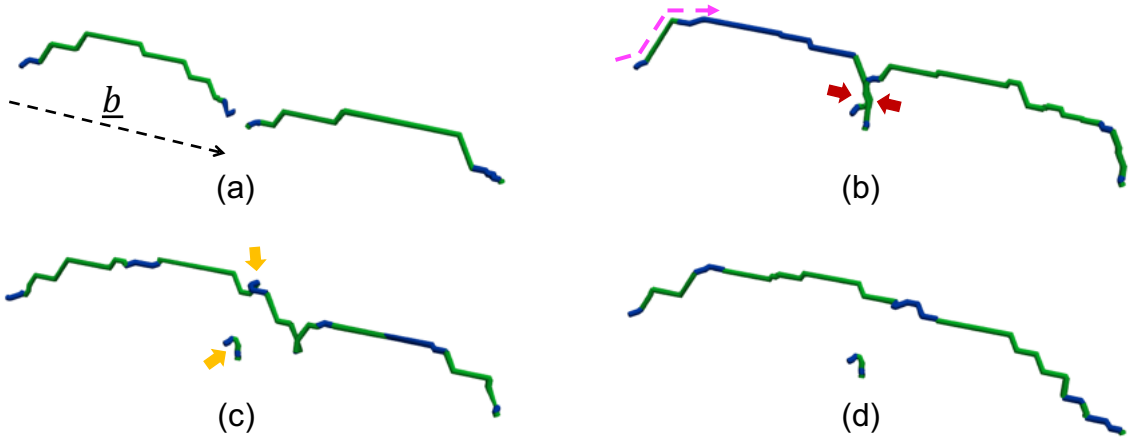

FIGURE E.2: Two short FR sources are progressively transformed into a longer FR source, displayed in (a)-(d). The dislocation segment in two colors corresponds to the 2 slip systems sharing the same Burgers vector. The direction of Burgers vector $\underline{\boldsymbol{b}}$ is indicated in (a) with a black dashed arrow. In (b), a double Cross-Slip is illustrated with a dashed rose arrow and the attractive force between the two dislocations of opposite signs is marked with red arrows. Such interaction ends with a collinear annihilation. In (c), after the annihilation of the dislocations, a longer source is formed. The two super-jogs involved in the collinear annihilation are noted with yellow arrows. In (d), the formed long source expands rapidly.

From this analysis, we see that the formation of a long FR source from two shorter FR sources is made possible from the collinear annihilation between two dislocations. From previous studies made with DD simulations, we know that such reaction is very strong and happens with many combinations of dislocation characters. In the grain simulations we made, this collinear annihilation is made possible because of the CS mechanism. Indeed, the latter is the mechanism which allows for the formation of super jogs along the dislocation lines (mainly with double cross-slip). These jogs are not mandatory, but significantly increase the number of collinear annihilation observed in the simulation. Then, it must be noted that the applied stress is higher in the small grain that makes the CS mechanism more active. As a consequence, the formation of long FR sources is more likely to take place in the small grains.

Appendix F

Résumé français

Pour les aciers de cuve et les aciers internes des réacteurs à eau pressurisée, des lois de plasticité cristalline ont déjà été élaborées. Celles-ci permettent de décrire la déformation moyenne en chargement monotone en tenant compte du durcissement de la forêt, des interactions entre les défauts d'irradiation et, d'une façon phénoménologique, l'effet Hall-Petch. Cependant, ces lois ne rendent pas compte de certains facteurs importants de la déformation plastique. Par exemple, les déformations hétérogènes induites par les joints de grains, qui induisent des contraintes internes à longue-portée est une source de durcissement supplémentaire. L'objectif principal de cette thèse est de proposer une approche simple et efficace pour modéliser les effets d'hétérogénéité de déformation permettant d'améliorer les lois cristallines existantes.

L'hétérogénéité de déformations dans les matériaux polycristallins résulte principalement de la présence de joints de grains limitant le libre parcours des dislocations. Les joints de grains, généralement considérés comme des barrières infranchissables au mouvement des dislocations, induisent un fort effet de taille modifiant la contrainte d'écoulement et le durcissement des matériaux. Cette propriété est classiquement décrite à l'aide d'une loi phénoménologique proposée par Hall et Petch. Bien que l'effet de Hall-Petch est largement impliqué dans la fabrication et le traitement des matériaux métalliques, son origine physique n'est toujours pas bien comprise. En effet il n'existe encore aucun modèle prédisant correctement le durcissement inter et intragranulaire des matériaux en fonction de paramètres microstructuraux, tels que la densité de dislocations, la forme des grains, les particules de seconde phase, la friction d'alliage, etc.

Dans cette thèse, nous allons d'utiliser les simulations de Dynamique des Dislocations (DD), identifiée maintenant comme la seule technique nous permettant de reproduire quantitativement les propriétés mécaniques à l'échelle mésoscopique. En effet, la DD permet de prédire le comportement collectif des dislocations, représentant la microstructure des aciers industriels. Cette méthode est alors essentielle pour réaliser un

changement d'échelle depuis l'échelle atomique (Calculs ab-initio, simula-tions atomiques, microscopie électronique, etc. . .) vers l'échelle continue, nécessaire à la modélisation du comportement mécanique des structures.

Dans un polycristal, les joints de grain sont les éléments primaires qui limitent le parcours des dislocations. En raison de la présence des joints de grain, la contrainte d'écoulement du matériau polycristallin augmente significativement par rapport au matériau monocristallin de même composition chimique. En outre, les résultats expérimentaux montrent que la réduction de la taille de grains augmente davantage la résistance mécanique des polycristaux. Lorsque la taille de grain est à l'échelle micrométrique, la contrainte d'écoulement est inversement proportionnelle à la racine de la taille de grain. Cette propriété du polycristal qui suit une loi phénoménologique proposée par Hall et Petch est appelée l'effet de Hall-Petch (HP).

L'effet de HP sur les propriétés mécaniques du polycristal est bien connu pour une vaste gamme des matériaux métalliques. Néanmoins, l'identification de la physique responsable de l'effet de HP est toujours le sujet d'actualité dans le milieu de la recherche. Par ailleurs, les études théoriques et expérimentales sont aujourd'hui essentiellement concentrées sur des polycristaux de grains équiaxiaux. Toutefois, les matériaux industriels sont généralement formés avec des grains ayant de forme non équiaxiale (par exemple la perlite, la martensite ou la bainite). Dans ce travail, nous avons réalisé les simulations de la Dynamique des Dislocations (DD) pour étudier l'effet HP à l'échelle des dislocations en considérant de simples agrégats polycristallins périodiques composés d'un grain ou quatre grains. De plus, l'influence de la forme du grain est explorée en simulant les grains avec différents rapports d'aspect : cube, plaquette ou aiguille.

Nos études se limitent à de petites déformations où la transmission de dislocation est difficile d'avoir lieu, les joints de grains dans nos simulations sont considérées comme les interfaces impénétrables pour les dislocations. Au total, nous avons simulé trois formes de grain avec la taille de grain comprise entre 1.25 et 10 μm. Pour chaque grain, trois simulations de traction ont été réalisées en modifiant l'orientation du grain entre [001], [111] et [135]. Remarquablement, ce type de simulation de modèle a réussi à reproduire un comportement de durcissement assez significatif. Dans nos simulations, la contrainte d'écoulement augmente quand la taille de grain diminue, ce qui est en accord avec la loi de HP. Nous avons constaté que le durcissement induit par les joints de grain était dépendant de l'orientation du grain. La valeur moyenne de la constante HP K calculée à 0.2% de déformation plastique est proche des valeurs expérimentales du cuivre. De plus, nous avons montré que l'effet HP était fortement influencé par la forme de grain. Enfin, une loi généralisée de HP est proposée, dans laquelle une taille de grain effective

est définie en tenant compte de la morphologie des grains.

L'accumulation de GNDs est localisée à proximité des GB, ce qui peut être approximé comme une singularité de surface de la concentration de dislocations. Pour calculer le champ de contrainte à longue-portée associé aux GNDs surfaciques, deux types de solutions analytiques ont été présentés. La première est une approche continue dérivée de la théorie de la Mécanique des Champs de Dislocations (MCD). La seconde est une approche discrète qui traite des sous-joints (SJ) infinis et finis de dislocations. En comparant ces solutions analytiques, nous avons constaté que la taille finie du SJ de dislocations mène toujours à une disparition de contraintes à longue distance du SJ. Les SJ des dislocations vis ne génèrent qu'un champ de distorsion élastique incompatible et peuvent être entièrement récupérées en intégrant le tenseur de Nye surfacique. Cependant, le champ de distorsion élastique compatible résultant des SJ des dislocations coin n'est pris en compte par aucun modèle de MCD.

Les deux solutions théoriques ci-dessus se limitent au cas idéal des SJ des dislocations. Afin d'aborder la variation de contraintes induites par la taille finie des SJ de dislocations, nous avons d'abord utilisé des simulations de DD pour modéliser les facettes avec différents caractères de dislocations, dimensions et densités de dislocation. Nous avons montré que la combinaison des solutions de contraintes de trois caractéristiques de base des facettes (torsion, flexion et épitaxiale) permettait de restaurer le champ de contraintes à longue-portée associé à tout type de réseau GNDs couvrant une surface de GB. Ce calcul est basé sur une approche empirique dérivée de la solution théorique du modèle MCD. En pratique, il s'agissait de déterminer deux paramètres obtenus à partir des résultats des simulations de DD. Le premier paramètre est un facteur d'intensité F nécessaire pour ajuster la différence d'amplitude des contraintes entre la solution FDM et les résultats de DD. La seconde est une fonction de forme $\xi(\hat{x})$ capturant le profil de variation de contrainte avec la distance à la facette. Avec un tel résultat, un modèle a été proposé pour calculer les contraintes internes à l'intérieur des grains comme la somme des contraintes generées par des GNDs surfaciques associées aux facettes de GBs.

Le modèle que nous avons proposé a été validé par une série de simulations de DD sur des grains et aggrégat CFC. Un tel résultat implique la possibilité de développer une nouvelle approche pour calculer le champ de contraintes à longue-portée dans la modélisation de la plasticité cristalline. Elle déduit le champ de contraintes internes à partir du calcul du tenseur de Nye dans la région GB ou plus simplement à partir d'une analyse géométrique supposant que l'activité de glissement plastique à l'intérieur des grains est homogène à petite déformation. Cette analyse sera développée dans le prochain chapitre.

Pour déterminer les mécanismes fondamentaux de l'effet de HP, nous avons réalisé des simulations de DD avec une géométrie simple, dans laquelle un grain cubique déformé plastiquement était inséré dans une matrice élastique infinie. Les contraintes internes à l'intérieur de grain ont deux origines. D'abord, les contraintes à courte-portée associées aux dislocations statistiquement stockées (SSDs) sont faible et peuvent être calculé à l'aide du modèle de la forêt. Ensuite, les contraintes à longue-portée (back stress) associées aux dislocations géométriquement nécessaires (GNDs) sont responsable de l'effet de durcissement et peuvent être calculé avec un modèle original basé sur le calcul d'une densité surfacique de GNDs. La somme de ces deux contributions a permis la reconstruction de la courbe de contrainte-déformation. De plus, nous avons montré que le taux de stockage de la densité surfacique de GNDs est une constante indépendante de la taille des grains. Par conséquent, l'augmentation du "back stress" est identique pour toutes les tailles de grains. Nos résultats révèlent que le back stress associée à l'accumulation de GNDs aux joints de grains peut être modélisé à partir d'une fonction linéaire de la déformation. Puisque le back stress n'est pas sensible à la taille de grain, son implication dans l'effet HP peut être exclue.

L'effet HP observé dans nos simulations résulte de la différence de cission résolue (CRSS) observé au tout début de la déformation plastique. Dans les faits, l'amplitude de la CRSS est contrôlé soit par la longueur de source de dislocation, soit par la densité initiale des dislocations. Dans les deux cas, la CRSS associée devrait être linéairement proportionnelle à $1/d$ ou plus précisément à $\ln(d/b)(1/d)$. Cependant, l'effet de taille reproduit par les simulations de DD est en meilleur accord avec une loi de la forme en $1/\sqrt{d}$. L'écart entre une loi en $\ln(d/b)(1/d)$ et en $1/\sqrt{d}$ s'explique par un réarrangement de la microstructure des dislocations pendant la relaxation plastique qui intervient pendant la phase de chargement élastique. Notre analyse quantitative avec des simulations de DD montre donc que l'effet HP est influencé par les propriétés de la microstructure des dislocations existant dans les grains avant déformation. Sous l'effet combiné de mécanismes locaux de durcissement et d'adoucissement telle que l'annihilation collinaire, l'effet de taille simulé en DD suit bien la relation classique dite de HP.

Enfin, l'analyse faite depuis nos simulations n'a pas permis d'expliquer l'effet HP observé dans des matériaux industriels avec une grosse taille de grain et avec une densité de dislocation relativement importante. Nous avons alors étendu notre analyse à la question de la localisation de la déformation dans les grains et à la formation d'empilements de dislocations qui en découle. Ces mécanismes sont reliés à la question de la transmission des dislocation aux joints de grains. Afin d'inclure ce denier effet dans notre modèle analyse issue des simulations de DD, une contrainte maximale d'écoulement plastique déduit du modèle classique des empilements a permis de définir une limite supérieure à

la CRSS qui élargie le domaine de validité de notre étude.

Bibliography

Acharya, Amit (2001). "A model of crystal plasticity based on the theory of continuously distributed dislocations". In: *J. Mech. Phys. Solids* 49.4, pp. 761–784. ISSN: 00225096. DOI: 10.1016/S0022-5096(00)00060-0. URL: http://linkinghub.elsevier.com/retrieve/pii/S0022509600000600.

Armstrong, R W et al. (1962). "The plastic deformation of polycrystalline aggregates". In: *Philos. Mag.* 7.73, p. 45. ISSN: null.

Armstrong, Ronald W (2014). "Engineering science aspects of the Hall–Petch relation". In: *Acta Mech.* 225.4, pp. 1013–1028. ISSN: 1619-6937. DOI: 10.1007/s00707-013-1048-2. URL: https://doi.org/10.1007/s00707-013-1048-2.

Ashby, M F (1970). "The Deformation of Plastically Non-homogeneous Materials". In: *Philos. Mag.* Pp. 399–424.

Baillin, X et al. (1987). "Dislocation transmission through $\Gamma = 9$ symmetrical tilt boundaries in silicon and germanium". In: *Philos. Mag. A* 55.2, pp. 143–164. ISSN: 0141-8610. DOI: 10.1080/01418618708209842. URL: https://doi.org/10.1080/01418618708209842.

Baldwin, W M (1958). "Yield strength of metals as a function of grain size". In: *Acta Metall.* 6.2, pp. 139–141. ISSN: 0001-6160. DOI: https://doi.org/10.1016/0001-6160(58)90136-6. URL: http://www.sciencedirect.com/science/article/pii/0001616058901366.

Bata, V and E V Pereloma (2004). *An alternative physical explanation of the Hall–Petch relation*. Vol. 52, pp. 657–665. DOI: 10.1016/j.actamat.2003.10.002.

Bean, Jonathan J et al. (2017). "Atomic structure and electronic properties of MgO grain boundaries in tunnelling magnetoresistive devices". In: *Sci. Rep.* January, pp. 1–9. DOI: 10.1038/srep45594. URL: http://dx.doi.org/10.1038/srep45594.

Benson, David, Hsueh-Hung Fu, and Marc Meyers (2001). *On the effect of grain size on yield stress: Extension into nanocrystalline domain*. Vol. 319, pp. 854–861. DOI: 10.1016/S0921-5093(00)02029-3.

Berbenni, S, V Favier, and M Berveiller (2007). "Impact of the grain size distribution on the yield stress of heterogeneous materials". In: *Int. J. Plast.* 23.1, pp. 114–142. ISSN: 0749-6419. DOI: https://doi.org/10.1016/j.ijplas.2006.03.004. URL: http://www.sciencedirect.com/science/article/pii/S074964190600043X.

Bhadeshia, H and R Honeycombe (2006). *Steels: Microstructure and Properties*. Ed. by H.K.D.H. Bhadeshia and Sir Robert Honeycombe. Third Edit. Oxford: Butterworth-Heinemann. ISBN: 978-0-7506-8084-4. DOI: https://doi.org/10.1016/B978-075068084-4/50003-0. URL: http://www.sciencedirect.com/science/article/pii/B9780750680844500030.

Borovikov, Valery, Mikhail I Mendelev, and Alexander H King (2017). "Effects of solutes on dislocation nucleation from grain boundaries". In: *Int. J. Plast.* 90, pp. 146–155. ISSN: 0749-6419. DOI: https://doi.org/10.1016/j.ijplas.2016.12.009. URL: http://www.sciencedirect.com/science/article/pii/S0749641916303539.

Bouaziz, O, S Allain, and C Scott (2008). "Effect of grain and twin boundaries on the hardening mechanisms of twinning-induced plasticity steels". In: *Scr. Mater.* 58.6, pp. 484–487. ISSN: 1359-6462. DOI: https://doi.org/10.1016/j.scriptamat.2007.10.050. URL: http://www.sciencedirect.com/science/article/pii/S1359646207007841.

Bragg, W L (1942). "A Theory of the Strength of Metals". In: *Nature* 149, p. 511. URL: https://doi.org/10.1038/149511a0http://10.0.4.14/149511a0.

Bullough, R and B A Bilby (1956). "Continuous Distributions of Dislocations: Surface Dislocations and the Crystallography of Martensitic Transformations". In: *Proc. Phys. Soc. Sect. B* 69.12, pp. 1276–1286. DOI: 10.1088/0370-1301/69/12/311. URL: https://doi.org/10.1088{\%}2F0370-1301{\%}2F69{\%}2F12{\%}2F311.

Burbery, N B et al. (2017). "Dislocation dynamics in polycrystals with atomistic-informed mechanisms of dislocation - grain boundary interactions". In: *J. Micromechanics Mol. Phys.* 02.01, p. 1750003. DOI: 10.1142/S2424913017500035. URL: https://doi.org/10.1142/S2424913017500035.

Caballero, F G et al. (2011). "Complementary use of transmission electron microscopy and atom probe tomography for the examination of plastic accommodation in nanocrystalline bainitic steels". In: *Acta Mater.* 59.15, pp. 6117–6123. ISSN: 1359-6454. DOI: https://doi.org/10.1016/j.actamat.2011.06.024. URL: http://www.sciencedirect.com/science/article/pii/S1359645411004381.

Calcagnotto, Marion et al. (2010). "Orientation gradients and geometrically necessary dislocations in ultrafine grained dual-phase steels studied by 2D and 3D EBSD". In: *Mater. Sci. Eng. A* 527.10-11, pp. 2738–2746. DOI: https://doi.org/10.1016/j.msea.2010.01.004.

Cheong, K. S., E. P. Busso, and A. Arsenlis (2005). "A study of microstructural length scale effects on the behaviour of FCC polycrystals using strain gradient concepts". In: *Int. J. Plast.* 21.9, pp. 1797–1814. ISSN: 07496419. DOI: 10.1016/j.ijplas.2004.11.001.

Cheong, Ke Shen and Esteban P. Busso (2004). "Discrete dislocation density modelling of single phase FCC polycrystal aggregates". In: *Acta Mater.* 52.19, pp. 5665–5675. ISSN: 13596454. DOI: 10.1016/j.actamat.2004.08.044.

Chia, Kuei-Hwa, Kang Jung, and Hans Conrad (2005). *Dislocation density model for the effect of grain size on the flow stress of a Ti–15.2 at.% Mo β-alloy at 4.2–650 K.* Vol. 409, pp. 32–38. DOI: 10.1016/j.msea.2005.03.117.

Christman, T (1993). "Grain boundary strengthening exponent in conventional and ultrafine microstructures". In: *Scr. Metall. Mater.* 28.12, pp. 1495–1500. ISSN: 0956-716X. DOI: https://doi.org/10.1016/0956-716X(93)90581-C. URL: http://www.sciencedirect.com/science/article/pii/0956716X9390581C.

Conrad, H (1963). "Effect of grain size on the lower yield and flow stress of iron and steel". In: *Acta Met.* 11.1, pp. 75–77. ISSN: 00016160. DOI: 10.1016/0001-6160(63)90134-2.

Conrad, H and G Schoeck (1960). "Cottrell locking and the flow stress in iron". In: *Acta Met.* 8.11, p. 791. ISSN: null.

Conrad, Hans (2004). "Grain-size dependence of the flow stress of Cu from millimeters to nanometers". In: *Metall. Mater. Trans. A* 35.9, pp. 2681–2695. ISSN: 1543-1940. DOI: 10.1007/s11661-004-0214-5. URL: https://doi.org/10.1007/s11661-004-0214-5.

Cordero, Z C, B E Knight, and C A Schuh (2016). "Six decades of the Hall–Petch effect – a survey of grain-size strengthening studies on pure metals". In: *Int. Mater. Rev.* 61.8, pp. 495–512. ISSN: 17432804. DOI: 10.1080/09506608.2016.1191808.

Cottrell, A.H. (1953). "Theory of dislocations". In: *Prog. Met. Phys.* 4, pp. 205–264. ISSN: 0502-8205. DOI: 10.1016/0502-8205(53)90018-5. URL: https://www.sciencedirect.com/science/article/pii/0502820553900185?via{\%}3Dihub.

Daveau, G. (2012). "Interaction dislocations – joints de grains en déformation plastique monotone : étude expérimentale et modélisations numériques". PhD thesis. École Centrale Paris.

De Baglion, Laurent (2011). "Comportement et endommagement en fatigue oligocyclique d'un acier inoxydable austénitique 304L en fonction de l'environnement (vide , air , eau primaire REP) à 300 °C". PhD thesis. Ecole Nationale Supérieure de Mécanique et d'Aérotechique - Poitiers.

Delannay, Laurent and Matthew R. Barnett (2012). "Modelling the combined effect of grain size and grain shape on plastic anisotropy of metals". In: *Int. J. Plast.* 32-33, pp. 70–84. ISSN: 07496419. DOI: 10.1016/j.ijplas.2011.12.002. URL: http://dx.doi.org/10.1016/j.ijplas.2011.12.002.

Déprés, Christophe (2005). "Modélisation physique des stades précurseurs de l'endommagement en fatigue de l'acier inoxydable austénitique 316L". PhD thesis. Institut National Polytechnique de Grenoble.

Devincre, B, T Hoc, and L.P. Kubin (2008). "Dislocation mean free paths and strain hardening of crystals." In: *Science (80-.).* 320.5884, pp. 1745–8. ISSN: 1095-9203. DOI: 10.1126/science.1156101. arXiv: arXiv:1011.1669v3. URL: http://www.ncbi.nlm.nih.gov/pubmed/18583605.

Devincre, B., L. Kubin, and T. Hoc (2006). "Physical analyses of crystal plasticity by DD simulations". In: *Scr. Mater.* 54.5, pp. 741–746. ISSN: 13596462. DOI: 10.1016/j.scriptamat.2005.10.066.

Devincre, B et al. (2011). "Modeling crystal plasticity with dislocation dynamcis simulations : the «MICROMEGAS» code". In: ed. by A. Ponchet S. Forest, pp. 81–100.

Dewald, M P and W A Curtin (2007). "Multiscale modelling of dislocation/grain-boundary interactions: I. Edge dislocations impinging on Σ11 (1 1 3) tilt boundary in Al". In: *Model. Simul. Mater. Sci. Eng.* 15.1, S193. ISSN: 0965-0393. URL: http://stacks.iop.org/0965-0393/15/i=1/a=S16.

Diawara, B (2011). "Caractérisation quantitative de la microstructure de l'acier 16MND5 des cuves de réacteurs nucléaires à eau pressurisée". PhD thesis. Université Grenoble.

Dunstan, D. J. and A. J. Bushby (2014). "Grain size dependence of the strength of metals: The Hall-Petch effect does not scale as the inverse square root of grain size". In: *Int. J. Plast.* 53, pp. 56–65. ISSN: 07496419. DOI: 10.1016/j.ijplas.2013.07.004. URL: http://linkinghub.elsevier.com/retrieve/pii/S074964191300140Xhttp://www.sciencedirect.com/science/article/pii/S074964191300140X.

El-Awady, Jaafar A (2015). "Unravelling the physics of size-dependent dislocation-mediated plasticity". In: *Nat. Commun.* 6.May 2014, pp. 1–9. ISSN: 20411723. DOI: 10.1038/ncomms6926. URL: http://dx.doi.org/10.1038/ncomms6926.

English, C and J Hyde (2012). "4.05 - Radiation Damage of Reactor Pressure Vessel Steels". In: *Compr. Nucl. Mater.* Ed. by Rudy J M Konings. Oxford: Elsevier, pp. 151–180. ISBN: 978-0-08-056033-5. DOI: https://doi.org/10.1016/B978-0-08-056033-5.00087-2. URL: http://www.sciencedirect.com/science/article/pii/B9780080560335000872http://dx.doi.org/10.1016/B978-0-08-056033-5.00087-2.

Fan, Haidong et al. (2015). "Orientation influence on grain size effects in ultrafine-grained magnesium". In: *Scr. Mater.* 97, pp. 25–28. ISSN: 13596462. DOI: 10.1016/j.scriptamat.2014.10.031. URL: http://dx.doi.org/10.1016/j.scriptamat.2014.10.031.

Feaugas, X. and H. Haddou (2003). "Grain-size effects on tensile behavior of nickel and AISI 316L stainless steel". In: *Metall. Mater. Trans. A* 34.10, pp. 2329–2340. ISSN: 1543-1940. DOI: 10.1007/s11661-003-0296-5. URL: http://dx.doi.org/10.1007/s11661-003-0296-5.

Feltham, P and J D Meakin (1957). "On the mechanism of work hardening in face-centred cubic metals, with special reference to polycrystalline copper". In: *Philos. Mag. A J. Theor. Exp. Appl. Phys.* 2.13, pp. 105–112. ISSN: 0031-8086. DOI: 10.1080/14786435708231728. URL: https://doi.org/10.1080/14786435708231728.

Foreman, A J E (1967). "The bowing of a dislocation segment". In: *Philos. Mag. A J. Theor. Exp. Appl. Phys.* 15.137, pp. 1011–1021. DOI: 10.1080/14786436708221645. URL: https://doi.org/10.1080/14786436708221645.

Franciosi, P, M Berveiller, and A Zaoui (1980). "Latent hardening in copper and aluminium single crystals". In: *Acta Metall.* 28.3, pp. 273–283. ISSN: 0001-6160. DOI: https://doi.org/10.1016/0001-6160(80)90162-5. URL: http://www.sciencedirect.com/science/article/pii/0001616080901625.

Frank, F C and W T Read (1950). "Multiplication Processes for Slow Moving Dislocations". In: *Phys. Rev.* 79.4, pp. 722–723. DOI: 10.1103/PhysRev.79.722. URL: https://link.aps.org/doi/10.1103/PhysRev.79.722.

Fressengeas, C, V Taupin, and L Capolungo (2011). "An elasto-plastic theory of dislocation and disclination fields". In: *Int. J. Solids Struct.* 48.25-26, pp. 3499–3509. ISSN: 0020-7683. DOI: 10.1016/j.ijsolstr.2011.09.002. URL: http://dx.doi.org/10.1016/j.ijsolstr.2011.09.002.

Fressengeas, C. et al. (2012). "Tangential continuity of elastic/plastic curvature and strain at interfaces". In: *Int. J. Solids Struct.* 49.18, pp. 2660–2667. ISSN: 00207683. DOI: 10.1016/j.ijsolstr.2012.05.020. URL: http://dx.doi.org/10.1016/j.ijsolstr.2012.05.020.

Fressengeas, Claude (2017). *Mechanics of Dislocation Fields*. Ed. by Wiley-ISTE. ISBN: 9781848213753. DOI: 10.1002/9781118578285.

Garner, F A et al. (1981). "The microstructural origins of yield strength changes in aisi 316 during fission or fusion irradiation". In: *J. Nucl. Mater.* 104, pp. 803–807. ISSN: 0022-3115. DOI: https://doi.org/10.1016/0022-3115(82)90698-5. URL: http://www.sciencedirect.com/science/article/pii/0022311582906985.

Haddou, Hakim (2003). "Influence de la taille de grain et de l'énergie de défaut d'empilement sur l'état de contraintes internes développé au cours de la déformation plastique en traction simple et en fatigue oligocyclique (alliages C.F.C.) Présentée". PhD thesis. Université de technologie de compiègne.

Hall, E.O. (1951). "The Deformation and Ageing of Mild Steel: III Discussion of Results". In: *Proc. Phys. Soc., Sect. B* 64.9, p. 747. ISSN: null.

Hamid, Mehdi et al. (2017). "Modeling and Characterization of Grain Boundaries and Slip Transmission in Dislocation Density-Based Crystal Plasticity". In: *Crystals* 7, p. 152. DOI: 10.3390/cryst7060152.

Hansen, B L, C A Bronkhorst, and M Ortiz (2010). "Dislocation subgrain structures and modeling the plastic hardening of metallic single crystals". In: *Model. Simul. Mater.*

Sci. Eng. 18.5, p. 55001. ISSN: 0965-0393. URL: http://stacks.iop.org/0965-0393/18/i=5/a=055001.

Hansen, N and B Ralph (1982). "The strain and grain size dependence of the flow stress of copper". In: *Acta Metall.* 30.2, pp. 411–417. ISSN: 0001-6160. DOI: https://doi.org/10.1016/0001-6160(82)90221-8. URL: http://www.sciencedirect.com/science/article/pii/0001616082902218.

Hansen, Niels (2004). "Hall-petch relation and boundary strengthening". In: *Scr. Mater.* 51.8 SPEC. ISS. Pp. 801–806. ISSN: 13596462. DOI: 10.1016/j.scriptamat.2004.06.002.

Haouala, Sarra, Javier Segurado, and Javier LLorca (2018). "An analysis of the influence of grain size on the strength of FCC polycrystals by means of computational homogenization". In: *Acta Mater.* 148, pp. 72–85. ISSN: 13596454. DOI: 10.1016/j.actamat.2018.01.024. URL: https://doi.org/10.1016/j.actamat.2018.01.024.

He, S. H. et al. (2017). "On the correlation among dislocation density, lath thickness and yield stress of bainite". In: *Acta Mater.* 135, pp. 382–389. ISSN: 13596454. DOI: 10.1016/j.actamat.2017.06.050.

He, S H et al. (2018). "Acta Materialia Evolution of dislocation density in bainitic steel : Modeling and experiments". In: *Acta Mater.* 149, pp. 46–56. DOI: 10.1016/j.actamat.2018.02.023.

He, W., W. Ma, and W. Pantleon (2008). "Microstructure of individual grains in cold-rolled aluminium from orientation inhomogeneities resolved by electron backscattering diffraction". In: *Mater. Sci. Eng. A* 494.1-2, pp. 21–27. ISSN: 09215093. DOI: 10.1016/j.msea.2007.10.092.

Hingwe, A K and K N Subramanian (1975). "Deformation of duplex crystals and two-phase bicrystals of alpha-beta brass". In: *J. Mater. Sci.* 10.2, pp. 183–188. ISSN: 1573-4803. DOI: 10.1007/BF00540340. URL: https://doi.org/10.1007/BF00540340.

Hirth, J P (1972). "The influence of grain boundaries on mechanical properties". In: *Metall. Trans.* 3.12, pp. 3047–3067. ISSN: 1543-1916. DOI: 10.1007/BF02661312. URL: https://doi.org/10.1007/BF02661312.

Hirth, J P and J Lothe (1982). *Theory of Dislocations*. Krieger Publishing Company. ISBN: 9780894646171. URL: https://books.google.fr/books?id=LFZGAAAAYAAJ.

Hu, Xianzhi et al. (2017). "Bauschinger Effect and Back Stress in Gradient Cu-Ge Alloy". In: *Metall. Mater. Trans. A* 48.9, pp. 3943–3950. ISSN: 1543-1940. DOI: 10.1007/s11661-017-4176-9. URL: https://doi.org/10.1007/s11661-017-4176-9.

Hughes, G D et al. (1986). "Hall-petch strengthening for the microhardness of twelve nanometer grain diameter electrodeposited nickel". In: *Scr. Metall.* 20.1, pp. 93–97. ISSN: 0036-9748. DOI: https://doi.org/10.1016/0036-9748(86)90219-X. URL: http://www.sciencedirect.com/science/article/pii/003697488690219X.

Jiang, Maoyuan, Benoit Devincre, and Ghiath Monnet (2019). "Effects of the grain size and shape on the flow stress: A dislocation dynamics study". In: *Int. J. Plast.* 113, pp. 111–124. ISSN: 0749-6419. DOI: https://doi.org/10.1016/j.ijplas.2018.09.008. URL: http://www.sciencedirect.com/science/article/pii/S0749641918303425.

Kacher, J P, G S Liu, and I M Robertson (2011). "Visualization of grain boundary/dislocation interactions using tomographic reconstructions". In: *Scr. Mater.* 64.7, pp. 677–680. ISSN: 1359-6462. DOI: https://doi.org/10.1016/j.scriptamat.2010.12.020. URL: http://www.sciencedirect.com/science/article/pii/S135964621000850X.

Kacher, Josh et al. (2014). "Dislocation interactions with grain boundaries". In: *Curr. Opin. Solid State Mater. Sci.* 18.4, pp. 227–243. ISSN: 1359-0286. DOI: https://doi.org/10.1016/j.cossms.2014.05.004. URL: http://www.sciencedirect.com/science/article/pii/S1359028614000217.

Kocks, U. F. (1970). "The relation between polycrystal deformation and single-crystal deformation". In: *Met. Mater. Trans.* 1.5, p. 1121. ISSN: null.

Kocks, U F and H Mecking (2003). "Physics and phenomenology of strain hardening: the FCC case". In: *Prog. Mater. Sci.* 48.3, pp. 171–273. ISSN: 0079-6425. DOI: https://doi.org/10.1016/S0079-6425(02)00003-8. URL: http://www.sciencedirect.com/science/article/pii/S0079642502000038.

Kocks, U. F., C. N. Tomé, and H. R. Wenk (2000). *Texture and Anisotropy: Preferred Orientations in Polycrystals and Their Effect on Materials Properties*. Cambridge University Press.

Kröner, Ekkehart (1963). "On the physical reality of torque stresses in continuum mechanics". In: *Int. J. Eng. Sci.* 1.2, pp. 261–278. ISSN: 00207225. DOI: 10.1016/0020-7225(63)90037-5. URL: http://www.sciencedirect.com/science/article/pii/0020722563900375.

Kubin, L., B. Devincre, and T. Hoc (2008). "Modeling dislocation storage rates and mean free paths in face-centered cubic crystals". In: *Acta Mater.* 56.20, pp. 6040–6049. ISSN: 13596454. DOI: 10.1016/j.actamat.2008.08.012. URL: http://dx.doi.org/10.1016/j.actamat.2008.08.012.

Kumar, K S, H Van Swygenhoven, and S Suresh (2003). "Mechanical behavior of nanocrystalline metals and alloys". In: 51, pp. 5743–5774. DOI: 10.1016/j.actamat.2003.08.032.

Lasalmonie, a and Jl Strudel (1986). "Influence of grain size on the mechanical behaviour of some high strength materials". In: *J. Mater. Sci.* 21, pp. 1837–1852. ISSN: 0022-2461. DOI: 10.1007/BF00547918. URL: http://link.springer.com/article/10.1007/BF00547918.

Lee, T C, I M Robertson, and H K Birnbaum (1990). "TEM in situ deformation study of the interaction of lattice dislocations with grain boundaries in metals". In: *Philos. Mag. A* 62.1, pp. 131–153. ISSN: 0141-8610. DOI: 10.1080/01418619008244340. URL: https://doi.org/10.1080/01418619008244340.

Lefebvre, S, B Devincre, and T Hoc (2007). "Yield stress strengthening in ultrafine-grained metals : A two-dimensional simulation of dislocation dynamics". In: *J. Mech. Phys. Solids* 55, pp. 788–802. DOI: 10.1016/j.jmps.2006.10.002.

Lemaitre, Jean and Jean-Louis Chaboche (1994). *Mechanics of Solid Materials*. Cambridge University Press.

Li, J C M (1963). "Petch relation and grain boundary sources". In: *Trans. Am. Inst. Met. Eng.* Pp. 227–239.

Li, J. C.M. (1960). "Some elastic properties of an edge dislocation wall". In: *Acta Metall.* 8.8, pp. 563–574.

Li, James C.M. and Charles D. Needham (1960). "Some elastic properties of a screw dislocation wall". In: *J. Appl. Phys.* 31.8, pp. 1318–1330. ISSN: 00218979. DOI: 10.1063/1.1735836.

Li, N et al. (2015). "Quantification of dislocation nucleation stress in TiN through high-resolution in situ indentation experiments and first principles calculations". In: *Sci. Rep.* May, pp. 1–8. DOI: 10.1038/srep15813.

Li, Y, A J Bushby, and D J Dunstan (2016). "The Hall–Petch effect as a manifestation of the general size effect". In: *Proc. R. Soc. A Math. Phys. Eng. Sci.* 472.2190. URL: http://rspa.royalsocietypublishing.org/content/472/2190/20150890.abstract.

Li, Y., A.J. Bushby, and D.J. Dunstan (2018). "Factors determining the magnitude of grain-size strengthening in polycrystalline metals". In: *Materialia*. ISSN: 25891529. DOI: 10.1016/j.mtla.2018.08.017. URL: https://linkinghub.elsevier.com/retrieve/pii/S2589152918300772.

Libert, Maximilien (2007). "Etudes expérimentale et numérique de l ' effet des mécanismes de plasticité sur la rupture fragile par clivage dans les aciers faiblement alliés". PhD thesis. École Centrale Paris.

Madec, R, B Devincre, and L P Kubin (2002). "From dislocation junctions to forest hardening." In: *Phys. Rev. Lett.* 89.25, p. 255508. ISSN: 0031-9007. DOI: 10.1103/PhysRevLett.89.255508.

Mathieu, Jean-philippe (2006). "Analyse et modélisation micromécanique du comportement et de la rupture fragile de l'acier 16MND5 : prise en compte des hétérogénéités microstructurales". PhD thesis. Arts et Métiers ParisTech.

Medina Almazan, L (2008). "Études expérimentale et numérique de l'effet du mercure sur le comportement mécanique des aciers 316L et T91". PhD thesis. École Centrale Paris.

Meyers, M A and E Ashworth (1982). "A model for the effect of grain size on the yield stress of metals". In: *Philos. Mag. A* 46.5, pp. 737–759. ISSN: 0141-8610. DOI: 10.1080/01418618208236928. URL: https://doi.org/10.1080/01418618208236928.

Meyers, M. A., A. Mishra, and D. J. Benson (2006). "Mechanical properties of nanocrystalline materials". In: *Prog. Mater. Sci.* 51.4, pp. 427–556. ISSN: 00796425. DOI: 10.1016/j.pmatsci.2005.08.003. arXiv: ProgressinMaterialsScience51(2006)427âĂŞ556.

Meyers, Marc A, Umberto R Andrade, and Atul H Chokshi (1995). "The effect of grain size on the high-strain, high-strain-rate behavior of copper". In: *Metall. Mater. Trans. A* 26.11, pp. 2881–2893. ISSN: 1543-1940. DOI: 10.1007/BF02669646. URL: https://doi.org/10.1007/BF02669646.

Mohles, Volker (2001). "Simulations of dislocation glide in overaged precipitation-hardened crystals". In: *Philos. Mag. A* 81.4, pp. 971–990. ISSN: 0141-8610. DOI: 10.1080/01418610108214330. URL: https://doi.org/10.1080/01418610108214330.

Monnet, G, S Naamane, and B Devincre (2011). "Orowan strengthening at low temperatures in bcc materials studied by dislocation dynamics simulations". In: *Acta Mater.* 59.2, pp. 451–461. ISSN: 1359-6454. DOI: https://doi.org/10.1016/j.actamat.2010.09.039. URL: http://www.sciencedirect.com/science/article/pii/S1359645410006166.

Monnet, Ghiath (2015a). "Acta Materialia Multiscale modeling of precipitation hardening : Application to the Fe – Cr alloys". In: *Acta Mater.* 95, pp. 302–311. ISSN: 1359-6454. DOI: 10.1016/j.actamat.2015.05.043. URL: http://dx.doi.org/10.1016/j.actamat.2015.05.043.

— (2015b). "New insights into radiation hardening in face-centered cubic alloys". In: *Scr. Mater.* 100, pp. 24–27. ISSN: 1359-6462. DOI: 10.1016/j.scriptamat.2014.12.003. URL: http://dx.doi.org/10.1016/j.scriptamat.2014.12.003.

— (2018). "Multiscale modeling of irradiation hardening : Application to important nuclear materials". In: *J. Nucl. Mater.* 508, pp. 609–627. ISSN: 0022-3115. DOI: 10.1016/j.jnucmat.2018.06.020. URL: https://doi.org/10.1016/j.jnucmat.2018.06.020.

Monnet, Ghiath, Ludovic Vincent, and Benoit Devincre (2013). "Dislocation-dynamics based crystal plasticity law for the low- and high-temperature deformation regimes of bcc crystal". In: *Acta Mater.* 61.16, pp. 6178–6190. ISSN: 1359-6454. DOI: 10.1016/j.actamat.2013.07.002. URL: http://dx.doi.org/10.1016/j.actamat.2013.07.002.

Morris, S B Biner and J R (2002). "A two-dimensional discrete dislocation simulation of the effect of grain size on strengthening behaviour". In: *Model. Simul. Mater. Sci. Eng.* 10.6, p. 617. ISSN: 0965-0393. URL: http://stacks.iop.org/0965-0393/10/i=6/a=303.

Mura, Toshio (1987). "General theory of eigenstrains". In: *Micromechanics of defects in solids*. Dordrecht: Springer Netherlands. ISBN: 978-94-009-3489-4. DOI: 10.1007/978-94-009-3489-4_1. URL: https://doi.org/10.1007/978-94-009-3489-4{_}1.

Naamane, S, G Monnet, and B Devincre (2010). "Low temperature deformation in iron studied with dislocation dynamics simulations". In: *Int. J. Plast.* 26.1, pp. 84–92. ISSN: 0749-6419. DOI: https://doi.org/10.1016/j.ijplas.2009.05.003. URL: http://www.sciencedirect.com/science/article/pii/S074964190900076X.

Naamane, Sanae (2008). "Etude de la déformation plastique de la ferrite à basse température : simulations de dynamique des dislocations". PhD thesis. Université Paris 6.

Navarro, A and E R de los Rios (1988). "An alternative model of the blocking of dislocations at grain boundaries". In: *Philos. Mag. A* 57.1, pp. 37–42. ISSN: 0141-8610. DOI: 10.1080/01418618808204497. URL: https://doi.org/10.1080/01418618808204497.

Nye, J F (1953). "Some geometrical relations in dislocated crystals". In: *Acta Metall.* 1.2, pp. 153–162. ISSN: 0001-6160. DOI: https://doi.org/10.1016/0001-6160(53)90054-6. URL: http://www.sciencedirect.com/science/article/pii/0001616053900546.

Odette, G R and G E Lucas (1998). "Recent progress in understanding reactor pressure vessel steel embrittlement". In: *Radiat. Eff. Defects Solids* 144.1-4, pp. 189–231. DOI: 10.1080/10420159808229676. URL: https://doi.org/10.1080/10420159808229676.

Ohashi, Tetsuya, Masato Kawamukai, and Hussein Zbib (2007). "A multiscale approach for modeling scale-dependent yield stress in polycrystalline metals". In: *Int. J. Plast.* 23.5, pp. 897–914. ISSN: 0749-6419. DOI: https://doi.org/10.1016/j.ijplas.2006.10.002. URL: http://www.sciencedirect.com/science/article/pii/S074964190600129X.

Ohashi, Tetsuya et al. (2009). "X-ray microdiffraction and strain gradient crystal plasticity studies of geometrically necessary dislocations near a Ni bicrystal grain boundary". In: *Int. J. Plast.* 25.5, pp. 920–941. ISSN: 07496419. DOI: 10.1016/j.ijplas.2008.04.009. URL: http://dx.doi.org/10.1016/j.ijplas.2008.04.009.

Ovid'ko, I A, A G Sheinerman, and R Z Valiev (2014). "ScienceDirect Dislocation emission from deformation-distorted grain boundaries in ultrafine-grained materials". In: *Scr. Mater.* 76, pp. 45–48. DOI: 10.1016/j.scriptamat.2013.12.012.

Parthasarathy, Triplicane A. et al. (2007). "Contribution to size effect of yield strength from the stochastics of dislocation source lengths in finite samples". In: *Scr. Mater.* 56.4, pp. 313–316. ISSN: 13596462. DOI: 10.1016/j.scriptamat.2006.09.016.

Pécheur, Anne Le (2008). "Fatigue thermique d'un acier inoxydable austénitique : influence de l ' état de surface par une approche multi-échelles". PhD thesis. École Centrale Paris.

Pechkovskii, É P et al. (1989). *Plastic deformation of polycrystals. Report II. Limit of elasticity and strain hardening of molybdenum, niobium, and iron.* Vol. 21, pp. 338–344. DOI: 10.1007/BF01529185.

Petch, N J (1953). "The Cleavage Strength of Polycrystals". In: *J. Iron Steel Inst.* 174.1, p. 25. ISSN: null.

Pipard, J et al. (2009). "A new mean field micromechanical approach to capture grain size effects". In: *Comput. Mater. Sci.* 45.3, pp. 604–610. ISSN: 0927-0256. DOI: 10.1016/j.commatsci.2008.06.012. URL: http://dx.doi.org/10.1016/j.commatsci.2008.06.012.

Poulsen, H F et al. (2003). "Lattice rotations of individual bulk grains: Part I: 3D X-ray characterization". In: *Acta Mater.* 51.13, pp. 3821–3830. ISSN: 1359-6454. DOI: https://doi.org/10.1016/S1359-6454(03)00206-4. URL: http://www.sciencedirect.com/science/article/pii/S1359645403002064.

Quek, Siu Sin et al. (2014). "Polycrystal deformation in a discrete dislocation dynamics framework". In: *Acta Mater.* 75, pp. 92–105. ISSN: 13596454. DOI: 10.1016/j.actamat.2014.04.063. URL: http://dx.doi.org/10.1016/j.actamat.2014.04.063.

Queyreau, Sylvain (2008). "Etude des mécanismes d'écrouissage sous irradiation de la ferrite par simulations de dynamique de dislocations". PhD thesis. Université Paris 6.

Queyreau, Sylvain, Ghiath Monnet, and Benoit Devincre (2009). "Slip systems interactions in α-iron determined by dislocation dynamics simulations". In: *Int. J. Plast.* 25.2, pp. 361–377. ISSN: 07496419. DOI: 10.1016/j.ijplas.2007.12.009.

— (2010). "Orowan strengthening and forest hardening superposition examined by dislocation dynamics simulations". In: *Acta Mater.* 58.17, pp. 5586–5595. ISSN: 13596454. DOI: 10.1016/j.actamat.2010.06.028. URL: http://dx.doi.org/10.1016/j.actamat.2010.06.028.

Raabe, Dierk et al. (2003). "Grain-scale micromechanics of polycrystal surfaces during plastic straining". In: *Acta Mater.* 51.6, pp. 1539–1560. ISSN: 13596454. DOI: 10.1016/S1359-6454(02)00557-8.

Rafael Velayarce, Jorge et al. (2018). "Influence of single and multiple slip conditions and temperature on the size effect in micro bending". In: *Acta Mater.* 154, pp. 325–333. ISSN: 13596454. DOI: 10.1016/j.actamat.2018.05.054. URL: http://linkinghub.elsevier.com/retrieve/pii/S135964541830421X.

Roters, F et al. (2010). "Overview of constitutive laws, kinematics, homogenization and multiscale methods in crystal plasticity finite-element modeling: Theory, experiments, applications". In: *Acta Mater.* 58.4, pp. 1152–1211. ISSN: 1359-6454. DOI: https://doi.org/10.1016/j.actamat.2009.10.058. URL: http://www.sciencedirect.com/science/article/pii/S1359645409007617.

Saada, G (1960). "On hardening due to the recombination of dislocations". In: *Acta Met.* 8.12, pp. 841–847. ISSN: 0001-6160. DOI: https://doi.org/10.1016/0001-6160(60)90150-4. URL: http://www.sciencedirect.com/science/article/pii/0001616060901504.

Saada, G. and E. Bouchaud (1993). "Dislocation walls". In: *Acta Met. Mater.* 41.7, pp. 2173–2178.

Sachtleber, M., Z. Zhao, and D. Raabe (2002). "Experimental investigation of plastic grain interaction". In: *Mater. Sci. Eng. A* 336.1-2, pp. 81–87. ISSN: 09215093. DOI: 10.1016/S0921-5093(01)01974-8.

Sansal, Christophe de, Benoit Devincre, and Ladislas Kubin (2009). *Grain Size Strengthening in Microcrystalline Copper: A Three-Dimensional Dislocation Dynamics Simulation*. Vol. 423, pp. 25–32. DOI: 10.4028/www.scientific.net/KEM.423.25.

Schall, Peter et al. (2006). "Visualizing dislocation nucleation by indenting colloidal crystals". In: *Nature* 440.7082, pp. 319–323. ISSN: 14764687. DOI: 10.1038/nature04557.

Schwartz, Julien (2011). "Approche non locale en plasticité cristalline : application à l'étude du comportement mécanique de l'acier AISI 316LN en fatigue oligocyclique". PhD thesis. École Centrale Paris.

Sekfali, Seddik (2004). "Influence de la microstructure sur le comportement local dans les aciers 16MND5". PhD thesis. École Centrale Paris.

Shan Le Wang and L. E. Murr (1980). "Effect of Prestrain and Stacking-Fault Energy on the Application of the Hall-Petch Relation in Fcc Metals and Alloys." In: *Metallography* 13.3, pp. 203–224. ISSN: 00260800. DOI: 10.1016/0026-0800(80)90001-4.

Shen, Z., R. H. Wagoner, and W. A T Clark (1986). "Dislocation pile-up and grain boundary interactions in 304 stainless stee". In: *Scr. Metall.* 20.c, pp. 921–926. ISSN: 00369748. DOI: 10.1016/0036-9748(86)90467-9. arXiv: arXiv:1011.1669v3. URL: http://linkinghub.elsevier.com/retrieve/pii/0036974886904679.

Shen, Z, R H Wagoner, and W A T Clark (1988). "Dislocation and grain boundary interactions in metals". In: *Acta Met.* 36.12, pp. 3231–3242. ISSN: 0001-6160. DOI: https://doi.org/10.1016/0001-6160(88)90058-2. URL: http://www.sciencedirect.com/science/article/pii/0001616088900582.

Shi, Qiwei (2018). "Experimental and numerical studies on the micromechanical crystal plasticity behavior of an RPV steel". PhD thesis. Université Paris-Saclay.

Sinclair, C. W., W. J. Poole, and Y. Bréchet (2006). "A model for the grain size dependent work hardening of copper". In: *Scr. Mater.* 55.8, pp. 739–742. ISSN: 13596462. DOI: 10.1016/j.scriptamat.2006.05.018.

Smith, E. and P. J. Worthington (1964). "The effect of orientation on the grain size dependence of the yield strength of metals". In: *Philos. Mag.* 9.98, pp. 211–216. ISSN: 00318086. DOI: 10.1080/14786436408229186.

Spearot, Douglas E and Michael D Sangid (2014). "Insights on slip transmission at grain boundaries from atomistic simulations". In: *Curr. Opin. Solid State Mater. Sci.* 18.4, pp. 188–195. ISSN: 1359-0286. DOI: https://doi.org/10.1016/j.cossms.2014.04.001. URL: http://www.sciencedirect.com/science/article/pii/S1359028614000175.

Stricker, M et al. (2016). "On slip transmission and grain boundary yielding". In: *Meccanica* 51.2, pp. 271–278. ISSN: 1572-9648. DOI: 10.1007/s11012-015-0192-2. URL: https://doi.org/10.1007/s11012-015-0192-2.

Sutton, A. P. and R. W. Balluffi (1995). *Interfaces in Crystalline Materials*. Oxford University Press, pp. 116–120. ISBN: 978-0199211067.

Tasan, C C et al. (2015). "An Overview of Dual-Phase Steels: Advances in Microstructure-Oriented Processing and Micromechanically Guided Design". In: *Annu. Rev. Mater. Res.* 45.1, pp. 391–431. DOI: 10.1146/annurev-matsci-070214-021103. URL: https://doi.org/10.1146/annurev-matsci-070214-021103.

Thompson, A W and W A Backofen (1971). "Production and mechanical behavior of very fine-grained copper". In: *Met. Trans.* 2, pp. 2004–2005.

Thompson, Anthony W, Michael I Baskes, and William F Flanagan (1973). "The dependence of polycrystal work hardening on grain size". In: *Acta Metall.* 21.7, pp. 1017–1028. ISSN: 0001-6160. DOI: https://doi.org/10.1016/0001-6160(73)90158-2. URL: http://www.sciencedirect.com/science/article/pii/0001616073901582.

Tsuchida, N. et al. (2008). "Effect of ferrite grain size on tensile deformation behavior of a ferrite-cementite low carbon steel". In: *Mater. Sci. Eng. A* 488.1-2, pp. 446–452. ISSN: 09215093. DOI: 10.1016/j.msea.2007.11.047.

Van Houtte, P (1982). "On the equivalence of the relaxed Taylor theory and the Bishop-Hill theory for partially constrained plastic deformation of crystals". In: *Mater. Sci. Eng.* 55.1, pp. 69–77. ISSN: 0025-5416. DOI: https://doi.org/10.1016/0025-5416(82)90085-4. URL: http://www.sciencedirect.com/science/article/pii/0025541682900854.

Wang, J, I J Beyerlein, and C N Tomé (2014). "Reactions of lattice dislocations with grain boundaries in Mg: Implications on the micro scale from atomic-scale calculations". In: *Int. J. Plast.* 56, pp. 156–172. ISSN: 0749-6419. DOI: https://doi.org/10.1016/j.ijplas.2013.11.009. URL: http://www.sciencedirect.com/science/article/pii/S0749641913002143.

Wang, L. et al. (2011). "Experimental characterization and crystal plasticity modeling of heterogeneous deformation in polycrystalline α-Ti". In: *Metall. Mater. Trans. A Phys. Metall. Mater. Sci.* 42.3, pp. 626–635. ISSN: 10735623. DOI: 10.1007/s11661-010-0249-8.

Winther, G et al. (2004). "Lattice rotations of individual bulk grains Part II: correlation with initial orientation and model comparison". In: *Acta Mater.* 52.10, pp. 2863–2872. ISSN: 1359-6454. DOI: https://doi.org/10.1016/j.actamat.2004.02.045. URL: http://www.sciencedirect.com/science/article/pii/S1359645404001223.

Xiang, Y and J J Vlassak (2005). "Bauschinger effect in thin metal films". In: *Scr. Mater.* 53, pp. 177–182. DOI: 10.1016/j.scriptamat.2005.03.048.

Yanushkevich, Z et al. (2017). "Acta Materialia Hall-Petch relationship for austenitic stainless steels processed by large strain warm rolling". In: *Acta Mater.* 136, pp. 39–48. ISSN: 1359-6454. DOI: 10.1016/j.actamat.2017.06.060. URL: http://dx.doi.org/10.1016/j.actamat.2017.06.060.

Yellakara, Ranga Nikhil and Zhiqiang Wang (2014). "A three-dimensional dislocation dynamics study of the effects of grain size and shape on strengthening behavior of fcc Cu". In: *Comput. Mater. Sci.* 87, pp. 253–259. ISSN: 09270256. DOI: 10.1016/j.commatsci.2014.02.037. URL: http://dx.doi.org/10.1016/j.commatsci.2014.02.037.

Yoshinaga, Naoki et al. (2008). "Deep Drawability of Electro-deposited Pure Iron Having an Extremely Sharp ‹111›//ND Texture". In: *ISIJ Int.* 48.5, pp. 667–670. DOI: 10.2355/isijinternational.48.667.

Zhang, Liang, Cheng Lu, and Kiet Tieu (2016). "A review on atomistic simulation of grain boundary behaviors in face-centered cubic metals". In: *Comput. Mater. Sci.* 118, pp. 180–191. ISSN: 09270256. DOI: 10.1016/j.commatsci.2016.03.021. URL: http://dx.doi.org/10.1016/j.commatsci.2016.03.021.

Zhang, Xu et al. (2014). "Internal length scale and grain boundary yield strength in gradient models of polycrystal plasticity: How do they relate to the dislocation microstructure?" In: *J. Mater. Res.* 29.18, pp. 2116–2128. ISSN: 20445326. DOI: 10.1557/jmr.2014.234.

Zhou, Caizhi, Irene J. Beyerlein, and Richard Lesar (2011). "Plastic deformation mechanisms of fcc single crystals at small scales". In: *Acta Mater.* 59.20, pp. 7673–7682. ISSN: 13596454. DOI: 10.1016/j.actamat.2011.08.032. URL: http://dx.doi.org/10.1016/j.actamat.2011.08.032.

Zhou, Caizhi and Richard Lesar (2012). "Dislocation dynamics simulations of plasticity in polycrystalline thin films". In: *Int. J. Plast.* 30-31, pp. 185–201. ISSN: 07496419. DOI: 10.1016/j.ijplas.2011.10.001. URL: http://dx.doi.org/10.1016/j.ijplas.2011.10.001.

Zinkle, S J, P J Maziasz, and R E Stoller (1993). "Dose dependence of the microstructural evolution in neutron-irradiated austenitic stainless steel". In: *J. Nucl. Mater.* 206.2, pp. 266–286. ISSN: 0022-3115. DOI: https://doi.org/10.1016/0022-3115(93)90128-L. URL: http://www.sciencedirect.com/science/article/pii/002231159390128L.

université PARIS-SACLAY
ÉCOLE DOCTORALE
Sciences mécaniques et énergétiques, matériaux et géosciences (SMEMAG)

Titre : Exploration des effets de la taille et de la forme des grains sur la plasticité cristalline par simulations de dynamique des dislocations

Mots clés : Effet de taille, Plasticité cristalline, Dynamique des dislocations, Contraintes internes

Résumé : Des simulations de dynamique de dislocation (DD) sont utilisées pour l'étude de l'effet Hall-Petch (HP) et des contraintes internes à long-portée induites par les hétérogénéités de déformation dans les matériaux polycristallins.

L'effet HP est reproduit avec succès grâce à des simulations de DD réalisées sur de simples agrégats polycristallins périodiques composés de 1 ou de 4 grains. De plus, l'influence de la forme des grains a été explorée en simulant des grains avec différents rapports d'aspect. Une loi généralisée de HP est proposée pour quantifier l'influence de la morphologie du grain en définissant une taille de grain effective. La valeur moyenne de la constante HP K calculée avec différentes orientations cristallines à faible déformation est proche des valeurs expérimentales.

Les dislocations stockées pendant la déformation sont principalement localisées à proximité des joints de grain et peuvent être traitées comme une distribution surfacique de dislocations. Nous avons utilisé des simulations DD pour calculer les contraintes associées aux parois de dislocations de différentes hauteurs, longueurs densités et caractères. Dans tous les cas, la contrainte est proportionnelle à la densité surfacique de dislocations géométriquement nécessaires (GNDs) et sa variation est capturée par un ensemble d'équations empiriques simples. Une prévision de contraintes à long-portée dans les grains est réalisée en sommant les contributions des GNDs accumulées de part et d'autre des joints de grains.

L'augmentation de la contrainte interne liée au stockage de GNDs est linéaire avec la déformation plastique et est indépendante de la taille des grains. L'effet de taille observé dans les simulations de DD est attribué au seuil de déformation plastique, contrôlé par deux mécanismes concurrents : la contrainte critique de multiplication des sources et la contrainte critique de franchissement de la forêt. En raison de la localisation de la déformation dans les matériaux à gros grains, le modèle d'empilement des dislocations doit être utilisé pour prédire la contrainte critique dans ce cas. En superposant cette propriété aux analyses que nous avons fait à partir de simulations de DD dans le cas d'une déformation homogène, l'effet HP est justifié pour une large gamme de tailles de grains.

Title : Investigation of grain size and shape effects on crystal plasticity by dislocation dynamics simulations

Keywords : Size effect, Crystal plasticity, Dislocation dynamics, Internal stress

Abstract : Dislocation Dynamics (DD) simulations are used to investigate the Hall-Petch (HP) effect and back stresses induced by grain boundaries (GB) in polycrystalline materials.

The HP effect is successfully reproduced with DD simulations in simple periodic polycrystalline aggregates composed of 1 or 4 grains. In addition, the influence of grain shape was explored by simulating grains with different aspect ratios. A generalized HP law is proposed to quantify the influence of the grain morphology by defining an effective grain size. The average value of the HP constant K calculated with different crystal orientations at low strain is close to the experimental values.

The dislocations stored during deformation are mainly located at GB and can be dealt with as a surface distribution of Geometrically Necessary Dislocations (GNDs). We used DD simulations to compute the back stresses induced by finite dislocation walls of different height, width, density and character. In all cases, back stresses are found proportional to the surface density and their spatial variations can be captured using a set of simple empirical equations. The back stress calculation inside grains is achieved by adding the contributions of GNDs accumulated at each GB facet.

These back stresses are found to increase linearly with plastic strain and are independent of the grain size. The observed size effect in DD simulations is attributed to the threshold of plastic deformation, controlled by two competing mechanisms : the activation of dislocation sources and forest strengthening. Due to strain localization in coarse-grained materials, the pile-up model is used to predict the critical stress. By superposing such property to the analysis we made from DD simulations in the case of homogeneous deformation, the HP effect is justified for a wide range of grain sizes.

Université Paris-Saclay
Espace Technologique / Immeuble Discovery
Route de l'Orme aux Merisiers RD 128 / 91190 Saint-Aubin, France